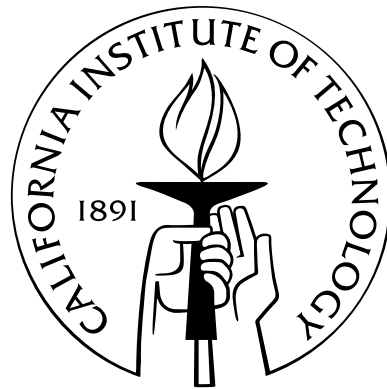


CRYSTALLINE WHISPERING GALLERY MODE RESONATORS FOR QUANTUM AND NONLINEAR OPTICS

Thesis by
Ivan S. Grudinin

In Partial Fulfillment of the Requirements
for the Degree of
Doctor of Philosophy



California Institute of Technology
Pasadena, California

2008
(Defended April 22, 2008)

Acknowledgements

Upon my arrival at Caltech in July 2003 I started work as a research assistant in the LIGO, Thermal Noise Interferometer group led by Prof. Ken Libbrecht, who has been a very supportive advisor all my graduate school years. Some of the first Americans I met were Eric Black and Akira Villar. I am grateful to them for helping me to adapt to a new life in Pasadena and for being very welcoming and friendly individuals. I am also grateful to Eric for teaching me better experimental research style. Vladimir Ilchenko inspired my transition to JPL. The main theme of my work has been shaped under his influence. Andrey Matsko not only has always been friendly, but also provided great deal of scientific mentoring and useful advice. As an outstanding theorist he provided constructive feedback and guidance to my experimental research. I was also happy to learn some article-writing skills from him. Anatoliy Savchenkov, on the other hand, being an outstanding and highly creative experimentalist, taught me many techniques and useful tricks in the laboratory. Many results of my work would not have been possible without his encouragement. Lute Maleki, who has been a supervisor for the Quantum Science and Technology Group at JPL and my advisor there, is a unique person. Not only has he managed scientific and financial issues with great success, but also provided fair critique and judgement to personal issues in the group. His ability of finding ways of making the experimental projects feasible has been the ultimate driver of my work. He has been a wonderful person to talk to and learn from. I have also enjoyed collaboration with Enrico Rubiola. The accuracy of his notebooks and electronic circuits has been a good example for me. Bill Diener has been notably friendly and helpful in actually making things work on a larger scale. Much of my cryogenic work has greatly benefited from the advice and support of Rabi Wang. Allyson Beatrice and Diana Parsegian have been helpful and friendly. Makan Mohageg has been a nice person to work with. Talking to him has been a great relief from the long working days in the lab. Thanh Lee has also been a very friendly person. Nan Yu, who became the new group supervisor, has shared a great deal of scientific knowledge and expertise in laser stabilization and related experimental questions. Dave Aveline and James Kellogg, as well as James Kohel and Robert Thompson, have been friendly and helpful in terms of hardware that could be borrowed. I would also like to mention the support I got on many occasions from such great people as Dmitry Strelakov, Meirong Tu, Daphna Enzer, Lawrence Lim, Sang Chung, Jon Dick, John Prestage, Ertan Salik and Nicole Czakon.

On the personal side I was also lucky to have friendly roommates Justin Bois and Shaunak Sen. Rasul Karabalin notably stands out as a bright and positive person. My other friends Dmitry Pavlov, Konstantin Taganov, Dmitry Kogan, Todor Tsankov, Vadim Borokhov, Mikhail Kislitsyn, Peter Mikhalev, and many others from Caltech Russian Club have made the years of study at Caltech much brighter. Tatyana Derevinska has been my inspiration through the years, especially during the long months of studying for my written Physics candidacy exams.

I also thank the Optical Society of America, Elsevier, the American Physical Society, and the American Institute of Physics for permission to reuse material of the papers published in their journals.

Special thanks to Professors Ken Libbrecht, Kerry Vahala, Lute Maleki, Yanbei Chen and Mark Wise for serving on my candidacy and defense committees.

Abstract

This work describes a series of projects and technology developments aimed at the realization of a solid-state photonic-ionic trap for quantum optics experiments. The projects however, are not constrained to this goal and explore the fields of nonlinear optics and fabrication techniques.

Fabri-Perot resonators have transformed the optical technology and can be found in many devices that utilize laser radiation. Whispering gallery mode resonators (WGMR) are relatively new elements and have such advantages as compactness, highest optical quality factors, and relative ease of fabrication. Small optical mode volume and long storage times allow record low thresholds of various nonlinear processes. Raman and Brillouin lasing, second and third harmonic generation, parametric oscillations and four wave mixing have all been enhanced in WGM resonators. Compared to glass microspheres, crystalline WGM resonators have higher nonlinear coefficients, may not be sensitive to water vapor, and have generally higher purity leading to record optical quality (Q) factors. Zero phonon lines of ions in crystals enable applications in cavity QED with single ions.

A novel application of diamond turning to fabrication of axially symmetric crystalline optical resonators is described. This technique enabled crystalline WGM microresonators, multiple resonators coupled via the evanescent field, and a single mode resonator. Crystalline resonators having a record high optical Q of 10^{11} were demonstrated. Fundamental limits of the Q factor were investigated and $Q = 10^{15}$ was predicted at cryogenic temperatures. Record low threshold and high efficiency of stimulated Raman and Brillouin scattering led to the first observations of these effects in crystalline cavities. Brillouin and Raman lasers based on WGM resonators are expected to have very narrow linewidth. A cryogenic setup was developed that allowed observation of WG modes at low temperatures. Crystalline cavity was used as a reference for narrowing a linewidth of a commercial diode laser with a Pound-Drever-Hall technique for the first time. A device based on a fused silica WGMR was used to generate beams with large angular momenta. In addition, a Fabri-Perot cavity was used to sense thermal expansion of mirrors to derive thermal expansion and temperature conductivity of thin optical coatings.

Contents

Acknowledgements	iii
Abstract	v
Timeline of research	1
0.1 Summary	6
1 Introduction	8
1.1 History of whispering gallery mode resonators	8
1.2 Analytical description of WG modes in dielectric resonators	9
1.2.1 Modes of a dielectric sphere	10
1.2.2 Mode volume	12
1.2.3 Modes of a spheroid	13
2 Fabrication of crystalline cavities	14
2.1 Application of diamond turning	14
2.1.1 Air-bearing spindle	15
2.1.2 Diamond cutter	16
2.1.3 Cutter positioning	17
2.1.4 Speeds and feeds	17
2.2 Polishing and cleaning techniques	18
3 New resonant structures	19
3.1 Single-mode cavity	19
3.2 Coupled resonators	25
3.3 Crystalline microcavities, Q factor, and tunability	26
3.3.1 Tuning crystalline microresonators by mechanical deformation	29
3.3.2 Precision spectroscopy of single ions	30
3.4 Resonators with reduced spectrum	33

4	Optical quality factors of crystalline cavities	34
4.1	Q factors of CaF ₂ cavities in linear regime	35
4.1.1	Introduction	35
4.1.2	Fabrication of the WGM resonators	36
4.1.3	Measurement of a Q factor	36
4.1.4	Q factor and pump power	37
4.1.5	Losses in crystalline cavities	38
4.1.5.1	Surface scattering	39
4.1.5.2	Material absorption and scattering	42
4.1.6	Maximum Q factor and its limitations	44
4.1.7	Nonlinear processes in crystalline WGM resonators and optical Q factor . . .	44
4.1.8	Impurities and possibilities for higher Q factors	48
4.1.9	Possible applications and conclusion	49
4.2	Fundamental limits and cryogenic Q factor of crystalline resonators	50
4.2.1	Three types of scattering	51
4.2.2	Properties of fluorite WGM resonators	52
4.2.3	Experimental observation of nonlinear attenuation	55
4.2.4	Conclusion	56
5	Photon–phonon interactions in crystalline resonators	57
5.1	Stimulated Raman scattering.	58
5.1.1	Introduction	58
5.1.2	Fabrication of the resonators	59
5.1.3	Low-threshold and cascaded generation of Raman Stokes	60
5.1.4	High-efficiency and single-mode Raman lasing	63
5.1.5	Conclusion	68
5.2	Stimulated Brillouin scattering	68
5.2.1	Introduction	69
5.2.2	Experimental observation of Brillouin and Raman lasing	70
5.2.3	Interpretation of experimental results	73
5.2.4	Brillouin scattering in fluorite	74
5.2.5	Conclusion	76
6	Laser linewidth narrowing with a WGM cavity as a frequency reference	78
7	Cryogenic apparatus	85

8 Applications of optical resonators	87
8.1 Bessel beam generation	87
8.1.1 Introduction	87
8.1.2 Experimental generation of truncated Bessel beams	88
8.1.3 Conclusion	91
8.2 Enhanced photothermal displacement spectroscopy	92
Bibliography	98
Vita	110

Timeline of research

I started my work at Caltech in July of 2003 by joining Professor Ken Libbrecht and his TNI group of LIGO. After learning some basic experimental techniques I started to work on the measurement of thermal conductivity and expansion coefficients in thin films with an interferometric method. My work was to expand and enhance the thin-film interferometer built by senior student Shanti Rao. In place of a light chopper I installed an electro-optical modulator, which led to dramatic increase of operational frequency range and sensitivity of the setup. I also brought software and hardware together to automate these measurements. I used mirrors with thin dielectric coatings which I additionally coated with a thin gold layer to perform the measurements. Upon completion of this project and a brief trip to a LIGO Livingston site as a scientific monitor in 2003, I joined the Quantum Science and Technology group at JPL, led by Lute Maleki.

Initially, the work included learning the various optical techniques used in the lab, such as fabrication of disk resonators and optical couplers, fiber splicing and polishing. The grand project goal of my work was set as the fabrication of crystalline microresonators with high Q factor and their subsequent utilization in cryogenic spectroscopy experiments with single ions. For that reason I also conducted a large literature survey on single-molecule spectroscopy techniques, rare-earth ion properties and zero phonon lines, cavity QED, crystalline blank suppliers, and polishing techniques. At that time the cryogenic setup started to take some shape on paper in numerous discussions with V.S. Ilchenko. This planning however, was still too far from any real implementation. Rudimentary attempts of making microcavities with crystals involved usage of dental handpieces, burs, and other miniature motors. Electro- and magneto-rheological polishing techniques were also adopted for early trials. After several trial-and-error months a simple cavity was fabricated. It was a MgF_2 resonator with a quality factor of only one million (Fig. 1). It was clear that a novel fabrication technique would be required. I started to develop a diamond turning apparatus in 2004. In initial attempts the computer hard drive brushless motors were used as spindles on which the crystalline workpiece was installed. Manual positioning of a cutter, sometimes represented by a grain of diamond or a piece of sapphire, was achieved with a 3-axis positioner from Thorlabs. It later became clear that brushless motors from hard drives, while being very stable, do not provide the necessary rigidity. A custom air bearing was made in the lab's machine shop for the 2nd attempt. This air-bearing spindle

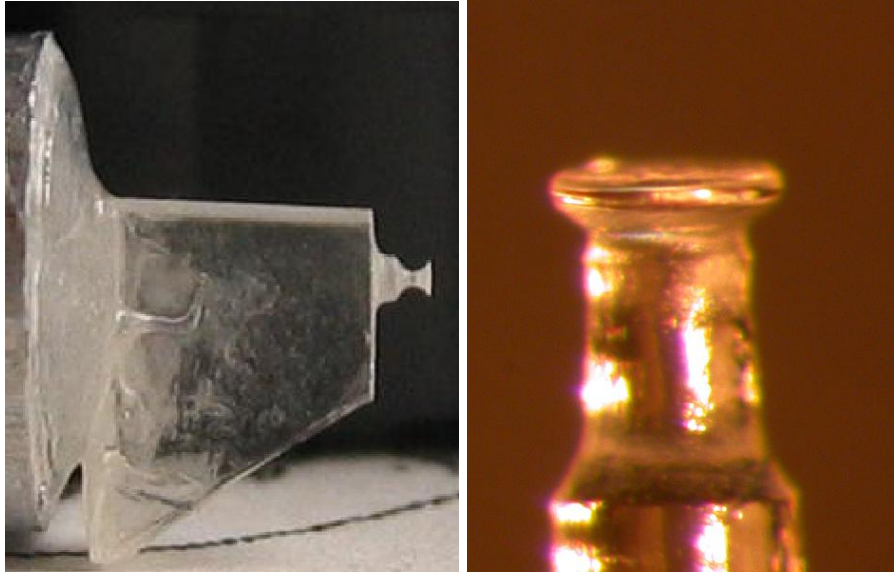


Figure 1: First and second attempts to make a resonator $450\ \mu\text{m}$ in diameter

was more robust, rigid, and could operate at speeds of up to 20000 rpm. Stepper motors controlled by a computer program were now positioning the diamond cutter and the microresonators were finally fabricated. Polishing of the resonator improved the quality factor. The polishing technique finally converged to a manual polishing with diamond abrasives and some tricky cleaning procedures. Soon afterwards a single-mode cavity was fabricated, along with several other multimode cavities on the same cylinder, representing coupled chains of resonators. Mechanical squeezing tunability of a magnesium fluoride microcavity was tested with success. In early 2005 it was also clear that the biggest challenge to any cryogenic operation of WGMRs would be coupling of light to the modes. Initial designs were developed that involved cunning applications of levers and PZT elements, such as shown on Fig. 2. The biggest challenge was the small available diameter of the cryogenic insert. It was difficult, if not impossible, to package all necessary functionality into such a small tube, as seen in Fig. 2, lower part.

In September of 2005 I also fabricated the first Bessel beam generating devices after a design suggested by A. Savchenkov and A. Matsko. At the same time there were some attempts at obtaining lasing with some residual Yb^{3+} impurities in the excimer grade fluorite bought from Corning. This was not successful, due to extremely low concentration of Ytterbium. The Q factor at that point was only 1.5 billion for 1.4 mm CaF_2 cavity and a search for the optimal polishing technique continued. This was all a bit frustrating as A. Savchenkov had already achieved 20 billion Q factor and the techniques seemed to be state of the art in a hard-to-repeat way. By November 10th the Q of 25 billion was achieved. Such a quality factor required a new laser for it to be measured, so a Lightwave Nd:YAG was installed instead of a “New Focus velocity” laser. By December 15, 2005 a Q factor of

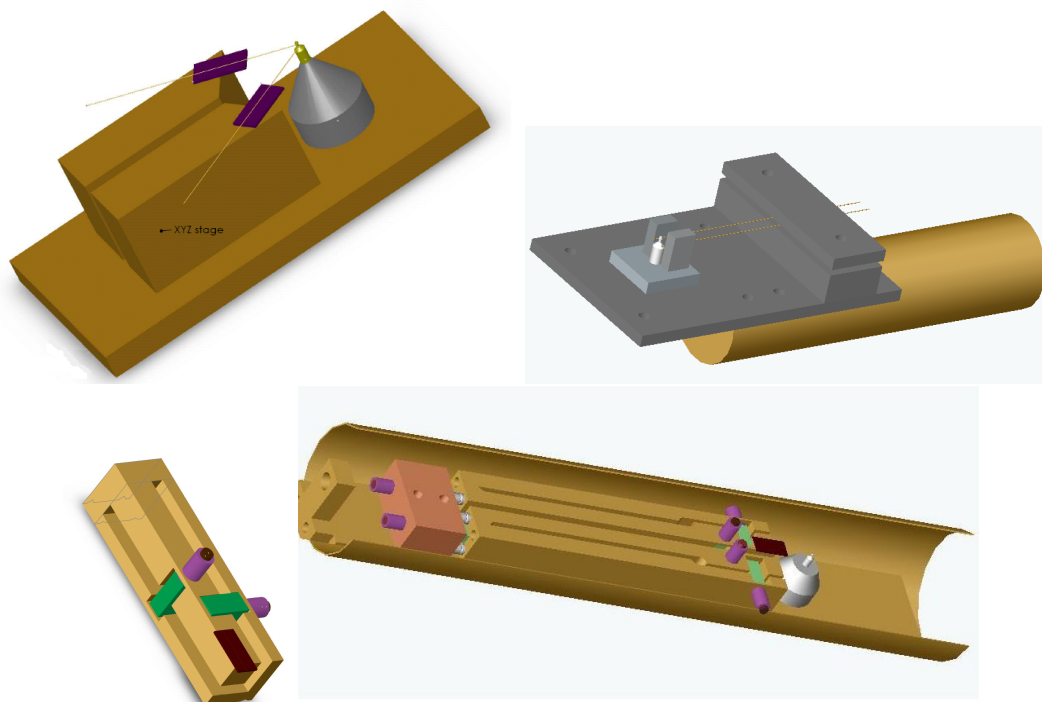


Figure 2: Evolution of designs for cryogenic operation of WGM resonators. Cantilevers are controlled by piezo elements and can be adjusted with a set-screw. Final design is described in Chap. 7.

63 billion was achieved and it was decided that further improvements would come only in a cryogenic environment. Later, however, A. Savchenkov showed that additional improvement by a factor of 5 could be achieved by repeatedly annealing and polishing the resonator at $\simeq 600^\circ C$.

At the same time three possible solutions to a cryogenic setup were discussed. One approach would involve gluing all the couplers, holders and a resonator together so that thermal expansion would be engineered and coupling would be maintained after cooling. Another approach involved purchasing the cryogenic nanopositioners which would do the job of coupling — in a compact setup. The problems included 4-inch-diameter limitation for the complete cryogenic insert and the absence of windows in a cryostat that I was given. This cryo was built 18 years ago by another student for measurements on He_3 samples at millikelvin temperatures. Subsequently I spent multiple months fixing leaks in this cryo, which led to almost complete rebuilding of the insert. The 2 positioner options we had were German Attocube's XYZ scanner with 30 micrometer translation at 4 K, and the three stick-slip stages with a millimeter scale translation. The former solution was \$10,000 and provided some chance of success while the latter was \$22,000 and was sure to do the trick. On a meeting with Lute Maleki and V. Ilchenko it was decided to take the risk and save the money. After about 3 months the XYZ scanner was delivered. The other solution of monolithic gluing was explored in the mean time.

In April of 2006 I implemented a simplified Pound-Drever-Hall technique to lock the laser to a WGM cavity, which allowed me to observe new phenomena in a CW mode. This included Raman lasing which I observed earlier in the CaF_2 cavities, despite the skeptical aptitude of other researchers. Raman threshold of the 1st and 2nd Stokes components was measured and proved to be the record low threshold for any Raman laser. Multiple cascaded lasing Stokes components were also observed. In June of 2006 I was also involved in a project aimed at accurate measurement of the parametric oscillation threshold in fluorite cavities. Enrico Rubiola was responsible for it, while A. Savchenkov was also involved; my role was to help Enrico with resonator technology. I made a cavity for him and helped him with locking a laser to it at 1550 nm. At the same time I was measuring Raman emission at around 1100 nm in my own setup. While the sought after parametric oscillation regime provides two symmetric sidebands in the optical spectrum, which are separated by cavity FSR around the pump mode, the sidebands Enrico and Anatoliy observed had unequal power. Moreover, they observed regimes with only a single sideband present as well as multiple asymmetric sideband regimes. Their sidebands were separated by a cavity FSR. I also observed a single sideband regime in my Raman lasing measurements at the same time with (arguably) the same disk they used, which was believed to be some sort of unconventional parametric oscillation. A year later when I started to process the data from my Raman measurements I found, to my great surprise, that the offset of the Stokes component, or a single sideband, in my case, was consistently not equal to the cavity FSR. Careful analysis and some estimations showed that a doubly resonant stimulated Brillouin scattering was being observed for the first time in crystalline cavities. In the end of June of 2006 a highly efficient Raman lasing was also observed, as well as lasing in microcavity, and a single mode cavity. Later the analysis was carried out to determine the limit of Q factor for crystalline cavities. Raman gain of fluorite was derived, which gave some hints as to why Raman lasing is rarely observed in the 1550 nm band, while parametric oscillations are hard to see in the 1064 nm band.

In November 2006 I invented a new way of making disk resonators with a small radius of curvature without diamond turning (see Sec. 3.4). On December 6, it was clear the cryogenic setup with an Attocube scanner was not working, as thermal drifts much larger than the useful positioning range were discovered. It was also learned that another group at Caltech, had obtained the cryogenic setup I hoped for by pursuing exactly the same approach that we couldn't afford. Despite frustration, we decided to move on and pursue a monolithic gluing approach. Careful analysis of thermal contraction properties of various available materials finally showed that it was simply not possible to build a setup in this way. Required mechanical precision of assembly was beyond our reach. In addition, the stiffness of the resulting assembly would not be high enough for coupling to be stable. On December 10 I started to play with a prototype of a stick-slip-based positioning mechanism and tried to reverse-engineer the Attocube positioners from the information available on the web. By the end of February I had a working and stable prototype which was analogous to the Attocube's

positioners and provided millimeter range positioning in 3 dimensions at low temperatures. In March I also developed a cryogenically compatible modification of a commercial web camera, so the two toughest problems of the cryostat, namely coupling and imaging, were resolved to some degree. The WG modes were observed at liquid nitrogen temperature in March 2007. At the time I was working on a cryo, I also designed a new experiment — spectroscopy of impurities with high Q WG modes. If I could measure Q factor at several wavelengths around the expected absorption line of residual Yb doping, I could derive some very low absorption coefficients. This would require a stable tunable laser, which could be used to measure Q factor at several wavelengths. If the Q factor were limited by impurities, which was widely believed, the variations in Q would provide information about spectral dependence of extremely weak absorption.

At the same time, in March of 2007 Lute decided to retire and leave the group, which he did in a matter of several months. After that, all the experimental work was even more difficult to carry on, due to funding limitations that followed. A Nd:YAG laser was finally returned to its owners and I was left with a New Focus Velocity laser, which has a wide linewidth of 300 kHz, making it impossible to measure high Q factor without additional stabilization. On May 3rd I finally found out how to clean the disks to an absolutely clean surface, which was very inspiring. I conducted the first experiment in spectroscopy, trying to obtain cavity Q factors in the range of 960–990 nm with a New Focus laser, but it turned out that the stability of the laser was not adequate and that a stabilized laser is the only practical solution. On the cryogenic front, a cold leak was found in the cryo, a leak that only opens at low temperature. Such a leak was not possible to locate with a helium leak detector. In May I started to work on laser stabilization and also planned to attend a conference in Munchen, Germany, at the end of June, returning in July. I designed a simplistic holder for a reference cavity that allowed for mechanical tuning and temperature control. While waiting for my return visa in Moscow I found the Brillouin scattering in the data I took a year ago. Unfortunately, bureaucracy at JPL and the Department of State prevented me from attending the conference and I got stuck in Moscow until August of 2007. Upon my return I discovered that there was virtually zero funding available for my research in the lab at JPL and I was expected to graduate soon. Nevertheless, there were hopes for a better situation and I continued to stabilize a laser. The hopes for a tunable laser had to be abandoned as well, as the tunable Velocity New Focus laser revealed pronounced phase and amplitude noises at frequencies up to 10 MHz, probably because of its age, which made it impossible to lock. So I adopted a New Focus Vortex laser, which was only marginally tunable. By December 2007 I had stabilized this laser to 10 KHz of linewidth. While I managed to make a servo electronics and some transimpedance photodetectors, the absence of funding finally took its toll and by December all work had to be halted. Subsequently my JPL badge was being renewed for about 2 more months. My last month at JPL was March, 2008, during which I participated in some simple experiments and helped others with WGM technology. I also observed parametric frequency

combs which are generated when a fluorite WGM resonator is pumped by 20–30 mW of radiation at 1550 nm.

0.1 Summary

The work presented in this dissertation may be characterized as a sequence of related projects. The relation between these projects is in their utility for realization of a major goal set forth at the beginning of my graduate work, without specific timeline or likelihood of achieving such goal. This major abstract goal may be defined as an experimental ability to optically detect and interrogate single ions embedded into a crystalline resonator. Thus a crystalline resonator would operate as a photonic and ionic trap at the same time. The goal requires several prerequisite technologies, some of which had to be created in the present work. Some projects appeared naturally from the creation of a new technology and produced interesting results. Chapters of this dissertation represent these projects and often contain portions of corresponding published papers.

The introductory chapter of this dissertation contains a short review of WGM resonator technology, historical outline, and related mathematical descriptions. Chapter 2 contains basic information on the fabrication techniques that were developed in the course of this work. The single-mode project [1] described in Sec. 3.1 was proposed and theoretically analyzed by A. Savchenkov and A. Matsko based on analogy with planar and regular single-mode waveguides and ring resonators. D. Strekalov developed the initial version of diamond turning control software in Labview. The author has debugged and improved the software, developed the fabrication technique and setup, fabricated the single-mode resonator and performed all measurements. Attempts to fabricate the single-mode resonators led to the results of Sec. 3.2, where coupled resonators are presented. Work presented in Sec. 3.3 was done mostly by the author. Most of the material presented in that section was previously published in the journal *Optics Communications* [2]. Structures in Sec. 3.4 resulted from playing with polishing regimes. The work presented in Sec. 4.1 was done mostly by the author with some participation and advising on the part of V.S. Ilchenko and L. Maleki. The results were published in *Physical Review A* [3]. Section 4.2 resulted from analytical work done together with A. Matsko and was published in *Optics Express* [4]. Lute Maleki and Andrey Matsko participated in theoretical analysis and editing of Sec. 5.1 and 5.2. Results presented there were published in *Optics Letters*, *Journal of Optical Society of America B* and *Physical Review Letters* [5, 6, 7]. Work presented in Sec. 6 and 7 was done by the author, as well as most of the experimental part of [8] (Sec. 8.1). The author's major contribution to the work in Sec. 8.2 was extending the frequency range by upgrading the experimental setup, automating the procedure, and carrying out all of the measurements.

Parts of this dissertation were presented at 6 conferences, and were distinguished by a best student presentation prize at the IQEC/CLEO-PR 2005 conference in Tokyo. New results were

marked by 3 NASA awards [9, 10], and were reported in industrial journals [11] and 9 peer-reviewed publications [1, 2, 8, 3, 5, 4, 7, 6, 12].

Conferences:

1. “Crystalline Cavities for Quantum and Nonlinear Optics”, CLEO-QELS, San Jose, CA. May 4–9, 2008. Poster session.
2. “Crystalline whispering gallery mode cavities for quantum optics”, Workshop on the Storage and Manipulation of Quantum Information in Optically-Addressed Solids, Bozeman, Montana, January 25–27, 2008.
3. “Crystalline cavities for quantum and nonlinear optics”, IQEC Europe, 2007, München, Germany. (Not attended)
4. “Towards cavity QED with crystalline microcavities”, CLEO 2006 Long Beach, California. Oral presentation.
5. “Crystalline microresonators: status and applications”, Photonics West 2006, San Jose, California. Oral presentation.
6. “Ultra high Q crystalline microcavities”, IQEC/CLEO-PR 2005 Tokyo, Japan July 12, 2005. Oral presentation.

Chapter 1

Introduction

1.1 History of whispering gallery mode resonators

Optical whispering gallery modes are named after the whispering gallery at St. Paul's Cathedral in London. Acoustical modes supported by this gallery were analyzed by Rayleigh in 1910 [13]. In 1939 Richtmyer [14] described electromagnetic modes of a dielectric sphere analytically and predicted high Q factors of these modes. Optical quality factors on the order of 10^6 were predicted but deemed potentially unattainable given a relatively poor quality of optical materials at that time. A subsequent more elaborate theoretical treatise may be found in a book written by Stratton [15].

Whispering gallery modes were implemented by numerous microwave and acoustic technologies. WG modes of the ionosphere of Earth were also analyzed. A significant body of research emerged from observation of WGMs in liquid microdroplets [16, 17], which inspired solid-state WG microresonators. One of the first experimental evidence of the optical WGMs known to the author was the observation of lasing in $\text{CaF}_2:\text{Sm}^{++}$ polished spheres in 1961 [18]. Another milestone, which launched optical WGM resonators into modern science and technology, was achieved in 1987 when the first optical fused silica resonators were demonstrated [19]. One of the important contributions of this work was the demonstration of a WGM resonator and a coupling technique as a vehicle, which could be deterministically used in optical experiments. Another technological advance came in 2003 with the fabrication of fused silica microtoroids using a combination of lithography and laser heating [20]. Similar techniques also enabled silicon microtoroids in 2004 [21, 22]. The WGM resonances, also known as morphology-dependent resonances, have proven to be useful in many photonics and optics applications. Miniaturization of these resonators makes new applications possible in precision physics experiments [23, 24].

Although whispering gallery modes were discovered almost a century ago, significant advances in their actual utilization in optics appeared only during the last couple of decades, following the invention of efficient resonator-light coupling methods. Development of the coupling techniques beyond a prism coupler has been equally important for this field. Angle-polished [25] and tapered

[26] fiber couplers have evolved into conventional laboratory coupling elements. Prism remains a coupler of choice where fibers with suitable refractive indices are unavailable. This is the case for lithium niobate WGMRs, which require a diamond prism coupler.

Historically, the WGM resonators have been fabricated with a variety of materials including, sapphire, fused silica, calcium fluoride, lithium niobate and other optical glasses and crystals. Even such exotic medium as solid hydrogen [27] was used. It was found in the 1980s that crystals such as sapphire offer extremely low loss for microwave WGMs, especially at low temperatures [28]. One of the first optical crystalline WGM resonators known to the author was fabricated in 2002 with a lithium niobate and used as an efficient microwave receiver [29]. Subsequently a Q factor in excess of 10^{10} was demonstrated in CaF_2 resonators [30]. The optically transparent crystals are particularly interesting for fabrication of the resonators because they naturally have many specific nonlinear-optical [31] and spectroscopic features, such as zero phonon lines, which are not so pronounced in amorphous materials. Another advantage of crystalline materials for the fabrication of the resonators is that the quality of the surface can be immune to humidity, as in the case of CaF_2 and MgF_2 . Quality (Q) factor of the fused silica microspheres and microdisks degrades when exposed to atmospheric water vapor [32]. The high Q factor of the resonators and their small size (small volume of the WGMs) is of great importance for a number of applications.

Contributions of the present work to the resonator technology and physics are described in the following chapters. A good account of the theory and applications of WGM resonators may be found in [33] and the work referenced there.

1.2 Analytical description of WG modes in dielectric resonators

Similarly to acoustic modes of a whispering gallery, optical WGM modes are formed when total internal reflection of light beams occur inside the dielectric resonator — be that an ideal sphere, a spheroid, or a thin disk. In optical WG modes this reflection takes place under an angle of incidence close to $\pi/2$, so that the beam is trapped inside the resonator and forms a closed trajectory. From the electromagnetic field point of view, most of the energy in a WG mode is located close to the surface. The structure of this field, as well as eigenfrequencies of the resonator and radiative losses may be analytically found in the case of an ideal sphere or a cylinder. For a non-ideal sphere this analytical solution may be used only approximately. Generally, in a non-spherical resonator represented by an arbitrary body of rotation the exact solutions for the WGM field is not known. Numerical methods have decreasing precision with increase of the resonator in terms of an optical wavelength. Some approximate methods still give good results.

1.2.1 Modes of a dielectric sphere

Analytical expressions for WG modes of an ideal sphere may be derived [14, 15] using, for example, a scalar Debye potential approach. It can be shown that in an isotropic dielectric, the field vectors \vec{E} , \vec{B} , \vec{D} , \vec{H} , vector potential \vec{A} and a Hertz vector \vec{P} satisfy the following equation:

$$\Delta \vec{C} - \frac{\varepsilon}{c^2} \frac{\partial^2 \vec{C}}{\partial t^2} = 0, \quad (1.1)$$

where \vec{C} — any of the field vectors, $\varepsilon = n^2$ — permittivity of a dielectric. By choosing a time dependence as $e^{i\omega t}$, this equation transforms into the vector Helmholtz equation:

$$\Delta \vec{C} + k_n^2 \vec{C} = 0, \quad (1.2)$$

where $k_n = n\omega/c = kn = 2\pi n/\lambda$ — wave number in the medium. This equation can always be represented by the equivalent system of three scalar equations. However, in non-cartesian systems of coordinates it is almost always impossible to resolve the resulting system with respect to any particular component. It is possible to build a solution in a spherical system of coordinates by involving the Debye potential, which satisfies the following scalar equation:

$$\Delta \Psi + k_n^2 \Psi = 0. \quad (1.3)$$

The three independent solutions of this Helmholtz equation are vector functions:

$$\vec{L} = \nabla \Psi, \quad \vec{M} = \nabla \times (\vec{r} \Psi), \quad \vec{N} = \frac{1}{k_n} \nabla \times (\vec{M}), \quad (1.4)$$

where \vec{r} — radius-vector and ∇ represents a Laplace operator. These vectors are mutually orthogonal and form a basis. The vector \vec{L} describes the potential part of the field and equals zero in the absence of free charges. The vectors \vec{N} and \vec{M} are solenoidal. The conventional notations for the types of modes are:

H-type (transverse-electric TE-modes), $\vec{E} \sim \vec{M}, E_r = 0,$

E-type (transverse-magnetic TM-modes), $\vec{E} \sim \vec{N}, H_r = 0.$

The variables can be separated and the solution for the scalar equation is represented by

$$\Psi = AY_{lm}(\theta, \phi)z_l(k_n r), \quad (1.5)$$

where A is a constant and $Y_{lm}(\theta, \phi)$ — spherical function, usually normalized to unity:

$$\int_0^\pi \int_0^{2\pi} Y_{lm}(\theta, \phi) Y_{l'm'}^*(\theta, \phi) d\phi d\theta = \delta_{ll'} \delta_{mm'}$$

$$Y_{lm}(\theta, \phi) = \sqrt{\frac{(l-m)! (2l+1)}{(l+m)! (4\pi)}} e^{\pm im\phi} P_m^l(\cos\theta).$$

Here $P_m^l(\cos\theta)$ are the associated Legendre polynomials, $z_l(k_n r)$ — radial spherical functions. In expression (1.5), when the area inside the sphere is described, z_l represents Bessel functions $j_l(k_n r)$ (finite at $r = 0$). When the space outside the sphere is described, z_l corresponds to the Hankel functions $h_l^{(1)}(k_n r)$, which are limited at infinity. The l index is called radial index or mode's order. It corresponds to the number of wavelengths along the resonator surface $l \simeq 2\pi nR/\lambda$. There are $l - m + 1$ maximums in θ direction, where m is the azimuthal index of the mode. The factors $e^{im\phi}$ and $e^{-im\phi}$ account for the two counter-propagating waves.

By applying a spherical Laplace operator

$$\begin{aligned} \nabla \times \mathbf{F} = & \frac{1}{r \sin\theta} \left(\frac{\partial(\sin\theta F_\phi)}{\partial\theta} - \frac{\partial F_\theta}{\partial\phi} \right) \mathbf{e}_r + \frac{1}{r} \left(\frac{\mathbf{1}}{\sin\theta} \frac{\partial \mathbf{F}_r}{\partial\phi} - \frac{\partial(\mathbf{r} \mathbf{F}_\phi)}{\partial \mathbf{r}} \right) \mathbf{e}_\theta \\ & + \frac{1}{r} \left(\frac{\partial(r F_\theta)}{\partial r} - \frac{\partial F_r}{\partial\theta} \right) \mathbf{e}_\phi \end{aligned}$$

to the solution of the scalar equation we obtain electric and magnetic field components in a Gaussian system of units for the time dependence of $e^{i\omega t}$ for TE -mode :

$$\begin{aligned} \hat{\mathbf{e}}^{TE} &= C^{TE} \left[\frac{m}{\sin\theta} Y_{lm}(\theta, \phi) z_l(kr) \mathbf{e}_\theta + i \frac{\partial Y_{lm}(\theta, \phi)}{\partial\theta} z_l(kr) \mathbf{e}_\phi \right], \\ \hat{\mathbf{b}}^{TE} &= C^{TE} \frac{1}{k_0 c} \left[l(l+1) Y_{lm}(\theta, \phi) \frac{z_l(kr)}{r} \mathbf{e}_r + \frac{\partial Y_{lm}(\theta, \phi)}{\partial\theta} \frac{\partial(r z_l(kr))}{r \partial r} \mathbf{e}_\theta + \right. \\ &\quad \left. + \frac{im}{\sin\theta} Y_{lm}(\theta, \phi) \frac{\partial(r z_l(kr))}{r \partial r} \mathbf{e}_\phi \right] \end{aligned} \quad (1.6)$$

and TM -mode:

$$\begin{aligned} \hat{\mathbf{e}}^{TM} &= C^{TM} \frac{1}{n^2 k_0} \left[l(l+1) Y_{lm}(\theta, \phi) \frac{z_l(kr)}{r} \mathbf{e}_r + \frac{\partial Y_{lm}(\theta, \phi)}{\partial\theta} \frac{\partial(r z_l(kr))}{r \partial r} \mathbf{e}_\theta \right. \\ &\quad \left. + \frac{im}{\sin\theta} Y_{lm}(\theta, \phi) \frac{\partial(r z_l(kr))}{r \partial r} \mathbf{e}_\phi \right] \\ \hat{\mathbf{b}}^{TM} &= -C^{TM} \frac{1}{c} \left[\frac{m}{\sin\theta} Y_{lm}(\theta, \phi) z_l(kr) \mathbf{e}_\theta + i \frac{\partial Y_{lm}(\theta, \phi)}{\partial\theta} z_l(kr) \mathbf{e}_\phi \right], \end{aligned} \quad (1.7)$$

where $z_l(kr)$ denote spherical Bessel functions $j_l(nk_0 r)$ inside the sphere and spherical Hankel functions $h_l^{(2)}(k_0 r)$ outside the sphere.

From the equality of tangential components of the field on the boundary ($r = R$):

$$E_\theta^i = E_\theta^e, \quad E_\phi^i = E_\phi^e, \quad (1.8)$$

$$B_\theta^i = B_\theta^e, \quad B_\phi^i = B_\phi^e, \quad (1.9)$$

we obtain the relations

$$C_e^{TE} = C_i^{TE} j_l(nk_0R)/h_l^{(2)}(k_0R), \quad (1.10)$$

$$C_e^{TM} = n^2 C_i^{TM} j_l(nk_0R)/h_l^{(2)}(k_0R) \quad (1.11)$$

which connect field amplitudes outside and inside the resonator. The boundary conditions also give a characteristic equation

$$\frac{p\partial[xj_l(x)]/\partial x}{j_l(x)} = \frac{\partial[xh_l^{(2)}(x)]/\partial x}{h_l^{(2)}(x)}. \quad (1.12)$$

Here $p = (1/n)^2$ for TM oscillations, and $p = 1$ for TE modes; $x = k_0R$ — is the so-called dimensional parameter of the sphere. This equation has many solutions which define the eigen numbers k_{lq} of oscillations of the dielectric resonator. Imaginary parts of solutions give radiative quality factor $Q_{\text{rad.}} = \frac{\text{Re}(x)}{2\text{Im}(x)}$. In an ideal sphere, all eigen numbers correspond to the same frequency, they are degenerate. If the geometry of the resonator is different from a sphere, frequencies of different k_{lq} are not the same. Thus the WGM is characterized with one more index — q . This index roughly corresponds to the number of wavelengths between total internal reflections of the beam.

1.2.2 Mode volume

The effective volume occupied by the electromagnetic field of a whispering gallery mode may be defined as follows:

$$V_{eff} \approx \frac{(\int \mathbf{E}^2 d^3\mathbf{r})^2}{\int \mathbf{E}^2 \mathbf{E}^2 d^3\mathbf{r}}, \quad (1.13)$$

where $\mathbf{E}(r, \theta, \phi)$ describes the mode's electric field distribution. For this definition of volume it is possible to obtain the estimate for E_{lm1}, H_{lm1} modes [34, 19]:

$$V_{eff} \approx 3.4\pi^{3/2} \left(\frac{\lambda}{2\pi n}\right)^3 l^{11/6} \sqrt{2(l-m)+1}, \quad \left(l = \frac{2\pi an}{\lambda}\right). \quad (1.14)$$

Here l is the radial index of the WGM, a is the radius of the resonator and m is the angular index of the mode. For the fused silica resonators, He–Ne laser wavelength of $\lambda = 633$ nm and the modes with the most compact θ –angle distribution of energy (modes E_{ll1}, H_{ll1}) one may estimate:

$$V_{eff} \approx 3 \times 10^{-11} \text{ cm}^3 \quad (l = 100, D \approx 14 \mu\text{m}),$$

$$V_{eff} \approx 2 \times 10^{-9} \text{ cm}^3 \quad (l = 1000, D \approx 140 \mu\text{m}).$$

1.2.3 Modes of a spheroid

Virtually any practically available WGM resonator may be approximated with a spheroid, so a recently obtained solution for WG modes in an arbitrary spheroid [35] appears to be especially useful in practice. Quasi-classical approach may be used to compute WG mode frequencies and radiative quality factors of a spheroidal resonator with equatorial axis “a” and polar axis “b”:

$$nka = l - \alpha_q \left(\frac{l}{2}\right)^{1/3} + \frac{2p(a-b) + a}{2b} - \frac{\chi n}{\sqrt{n^2 - 1}} + \frac{3\alpha_q^2}{20} \left(\frac{l}{2}\right)^{-1/3} - \frac{\alpha_q}{12} \left(\frac{2p(a^3 - b^3) + a^3}{b^3} + \frac{2n\chi(2\chi^2 - 3n^2)}{(n^2 - 1)^{3/2}}\right) \left(\frac{l}{2}\right)^{-2/3} + O(l^{-1}), \quad (1.15)$$

where $k = \frac{\lambda}{2\pi}$ is the wavenumber, $l \gg 1$, $p = l - |m| = 0, 1, 2, \dots$ and $q = 1, 2, 3, \dots$ are integer mode indices. α_q are negative zeros of order q of the Airy function, n — refractive index of the optical material. For quasi-TE modes $\chi = 1$ and for quasi-TM modes $\chi = 1/n^2$.

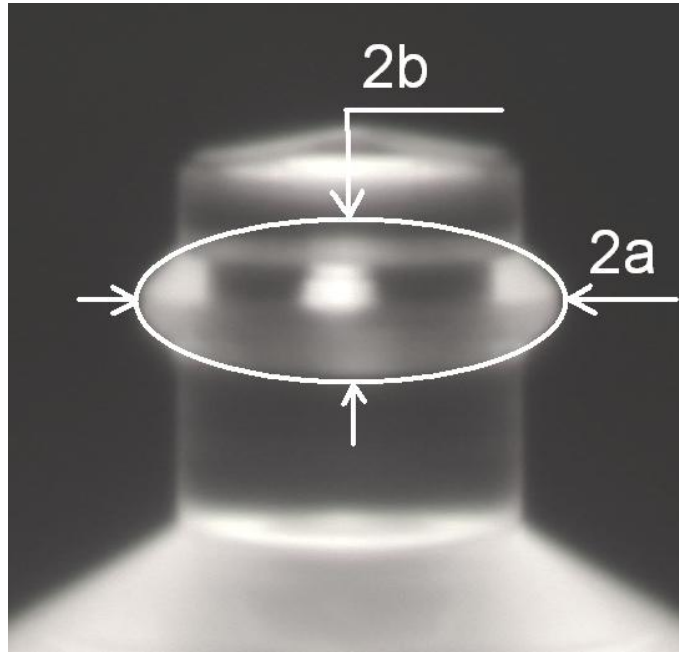


Figure 1.1: Crystalline WGM resonator and the approximating spheroid in cross section

Chapter 2

Fabrication of crystalline cavities

Unlike fused silica resonators, crystalline cavities may not be formed by a heat-assisted reflow process. No lithography techniques are known to work for the majority of optical crystals in terms of generating polished surfaces. A mechanical fabrication technique is required. Such technique was developed at JPL and significantly improved as described in this thesis. It allowed fabrication of crystalline resonators with arbitrary geometry of surface, including microresonators.

The present work was motivated by a project in which single dopant ions would be strongly coupled to the mode of a resonator. The strong coupling required fabrication of micro-resonators, for which the technique available in the lab at that time was not suitable. Straightforward extension of fabrication capabilities could be provided by application of a single point diamond turning process (SPDT). The field of SPDT and polishing is akin to jewelry, as it looks more like a set of engineering tricks rather than an implementation of predictions of a scientific theory. One of the reasons may be that the processes involved are too complicated and involve chemistry, tribology, solid mechanics, and thermodynamics. These tricks are based on empirical research and are usually hidden behind corporate walls. Consequently, the literature on the topic is anywhere from scattered to non-existent. Some papers still offer valuable pieces of information [36, 37, 38, 39, 40, 41, 42].

2.1 Application of diamond turning

After a significant trial-and-error stage, a prototype computer-controlled SPDT apparatus was developed. This allowed me to fabricate crystalline axially symmetric optical elements with any desirable surface structure and good surface roughness. The key elements include a heavy mounting plate, a precision air-bearing spindle, a dc motor, a custom-made diamond cutter, a motorized cutter positioning stage, PC, and software.

The starting point of resonator fabrication is a crystalline cylinder which is obtained from a crystal blank with a special coring drill and a diamond suspension used as an abrasive.

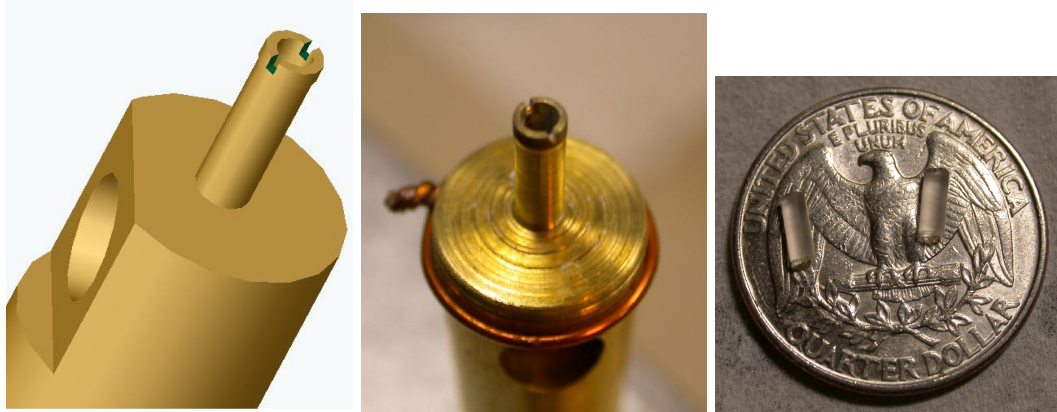


Figure 2.1: Fabrication of crystalline cylinder with a coring drill

2.1.1 Air-bearing spindle

Initially, the experiments on SPDT were carried out on simple DC motors and later on DC brushless motors of commercial hard disk drives (HDD). These motors, especially those with fluid dynamic bearing technology, have very stable rotational repeatability and stability at high speeds, mandated by precision HDD technology. Unfortunately for my application, these motors did not provide high stiffness of the spindle, required in SPDT. Soft spindle leads to rotational instabilities under mechanical load and a diamond tool damage. It was realized that air-bearing technology is conventionally used in SPDT and, after an initial successful prototype, a working model of a compact air bearing measuring 1/2 inch in diameter was assembled in the laboratory. While the spindle has several resonances, it allows smooth operation at speeds of up to 15000 rpm. Air bearing is generally a

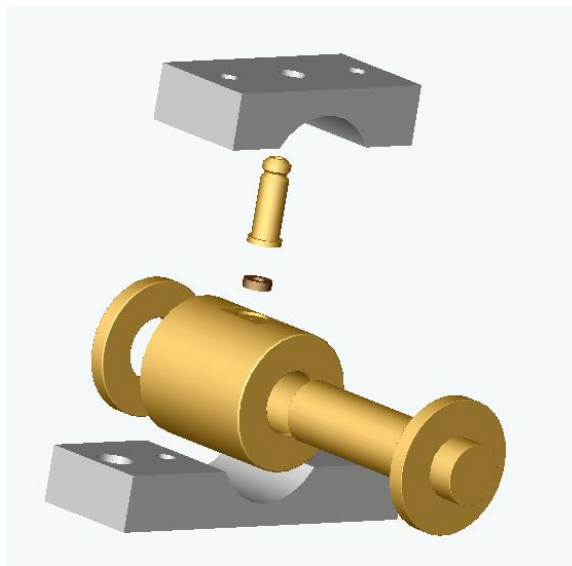


Figure 2.2: Model of the air-bearing spindle

shaft with a polished surface, which is enclosed in a holder. The inner surface of a holder follows the geometry of the shaft and is also polished. Pressurized dry air is supplied to a small gap between the shaft and the enclosure, serving as an almost perfect lubricant. The biggest challenge in fabricating the air bearing is smallness of the air gap, typically around 20–50 micrometers. Such a bearing has a near zero friction and a high stiffness, comparable and even exceeding that of conventional ball bearings of similar size. In addition, such bearings have very good repeatability of rotation.

A brushless 5-watt motor from Maxon was coupled to the spindle on one end via a magnetic clutch. Powerful and compact neodymium magnets provided torque transfer while isolating motor vibrations. A tight-fitting cap with fixation screws was attached to the other end of the spindle and the crystalline workpiece could be glued to that cap.

2.1.2 Diamond cutter

Diamond turning of crystals may be carried out in two modes: ductile and brittle. The brittle mode machining results in a surface pitted with numerous cracks and fractures and hence is not practical for optical fabrication. In a ductile machining mode the surface undergoes phase transition and the material is removed evenly resulting in an optically smooth surface. Achieving this regime generally requires implementing certain machining parameters such as workpiece rotation speed, depth of cut, feed speed, diamond tool rake and relief angle, and are specific for various crystals. The tools used in this work were designed in Solidworks and custom made by Chardontool for the optimal machining of calcium fluoride CaF_2 . They had a -20 degree rake angle and 2 degree relief angle of the cutting edge. The shape was designed so as to allow fabrication of micrometer scale features and cavities with diameter down to $40\ \mu\text{m}$. Alternatively, good cutting results were obtained with usage of commercial optical diamond prisms instead of a cutter.

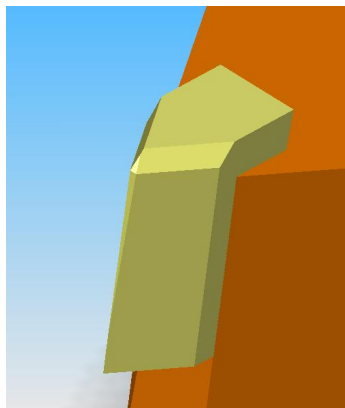


Figure 2.3: Model of a cutter for fluorite machining

2.1.3 Cutter positioning

Positioning of a diamond cutting tool was carried out with help of two Thorlabs positioning stages, two stepper motors “Z625B” and a vertical positioning stage. The cutter was mounted onto the X-Y stages via magnetic kinematic base plate. Stepper motors were controlled by a PC with a Labview-based software, which had options for manual control of the position and automatic motion along a programmed trajectory. Calculated resolution of the motors is 40 nm and measured backlash is around $3\ \mu\text{m}$. This backlash was compensated programmatically. Programmed trajectories used to fabricate microstructures took cutter geometry into account.

2.1.4 Speeds and feeds

Even though the machining setup was designed to be rather stiff, it was not stiff enough by commercial standards. Minute vibrations in a spindle and positioning mechanics led to accelerated degradation of a cutting edge, as shown on Fig. 2.4. In some cases only a couple miles of optically

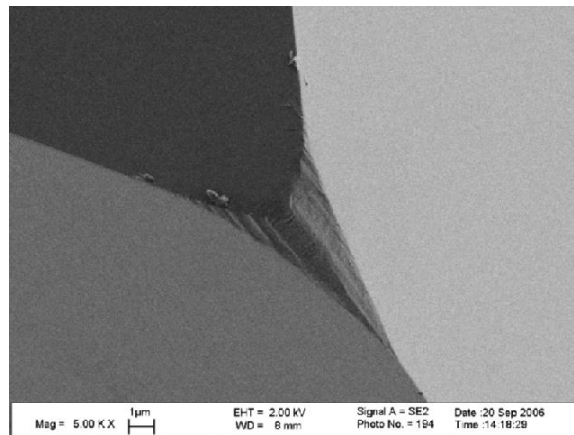


Figure 2.4: Diamond tool wear

ideal surface, on which no fractures could be seen at $\times 400$ magnification, could be obtained. Ideally, cutter position should be controlled with nanometer precision to reduce accidental jumps and vibration. Cutting speed should be chosen such that would provide the longest tool life. Cutting edge wear is a major problem of SPDT. For fluorite machining rotation speeds of 90–3000 rpm, feeds of $0.25\text{--}5\ \mu\text{m}$ per revolution, and depth of cut of $0.25\text{--}2\ \mu\text{m}$ were found useful. Further optimization is possible. The described SPDT apparatus allowed me to fabricate structures with features as small as $3\ \mu\text{m}$, and the Q factor of resonators right after the turning step was as high as 10^7 , corresponding to a good surface roughness.

2.2 Polishing and cleaning techniques

Surface roughness and cleanliness are critical for ultrahigh optical Q factors. Surface roughness of better than 0.2 nm rms was achieved with a hand-polishing method. Much better results may be possible with application of other advanced techniques such as magneto- or electro-rheological polishing.

A diamond suspension from Alliedhightech were used for resonator polishing. Pure isopropanol and water were used for cleaning. Acetone may be used in some cases, but is not generally required. Low lint paper napkins were used as polishing and cleaning cloth.

Specific polishing sequence depends on the goal of the process. If polishing of SPDT-fabricated structures is required, initial diamond grit of $0.25 \mu\text{m}$ may be used. If the starting point is a plain crystalline cylinder, the initial stage of polishing can be accomplished with diamond grits of up to $20 \mu\text{m}$ at high speed. This initial polishing can also be used to define resonator shape. Thus SPDT may not be required when relatively simple large resonators are needed. In fact, it is possible to formulate a resonator with radius of curvature as small as $5 \mu\text{m}$ or even less (as shown in Sec. 3.4) without SPDT. On the other hand, single-mode or micro resonators are likely to require SPDT or other advanced fabrication techniques.

Thin stripes of polishing cloth are cut and twisted to form threads, which are then soaked with a diamond suspension. Before the suspension grit size can be reduced, a cleaning step is required. This is usually accomplished by polishing with alcohol instead of diamond suspension, followed by a wiping step. Generally, the grit size sequence is as follows: 20, 3, 1, 0.25, 0.1, $0.05 \mu\text{m}$. A Q factor exceeding 10^{10} is usually achieved after a $0.25 \mu\text{m}$ polishing step.

Chapter 3

New resonant structures

Each whispering gallery mode in an arbitrary resonator is identified by three indices, which define distribution of optical field nodes over the volume of the resonator. Frequencies corresponding to each combination of these indices are generally different, which leads to a rather complicated spectrum. Geometry of a resonator imposes boundary conditions which define the spectrum and may exclude certain combinations of indices. Thus modifying the resonator surface and diameter is a way to control its spectrum. Development of a diamond turning apparatus has enabled this control over surface geometry and allowed the author to fabricate several new types of resonators. This chapter includes material presented in an *Optics Letters* paper [1] and an *Optics Communications* paper [2]. Materials reproduced with permissions from OSA and Elsevier.

3.1 Single-mode cavity

There are two general ways to engineer optical modes. The most common approach is to use optical waveguides to confine and guide light. The waveguide is based on the refractive-index contrast between its material and the surroundings to support light confinement and guiding. In the other approach, a photonic bandgap crystal [43] provides confinement and guiding of photons by use of the morphology of the structure. One achieves this by placing defects in otherwise periodic arrays of a dielectric material.

The utility of WGM-based devices and the efficiency of nonlinear optical interactions of WGMs depend on accurate engineering of the cavity mode structure. Achieving the required level of control over the mode spectrum has eluded scientists working on WGM resonators. Thus WGM resonators have as yet neither entered the mainstream of photonic device engineering nor been embraced by the optical physics. Practically all WGM resonators have more-or-less complicated modal structures, in other words they have more than one mode per free spectral range. This is an obstacle for many practical applications. The nature of the dense spectrum can be easily understood. The special functions that describe WGM in a perfect dielectric sphere are degenerate. In other words,

many modes have the same eigenfrequency. This degeneracy is lifted when the geometry of the resonator is changed to anything different from a perfect sphere. Generally speaking, the special functions should also be different and in most cases it is impossible to resolve the electromagnetic field into any possible kind of special functions. Only approximate analytical and numerical methods may be helpful [35]. The modes that have identical eigenfrequency in a spherical resonator would have different eigenfrequencies in a non-spherical one. This creates a rich optical spectrum in real resonators, which are always non-spherical. However, the same degeneracy lifting can be useful. In this section a new approach to designing the geometry of the resonator and controlling the structure of its optical spectrum is demonstrated. It relies on generating an effective refractive-index contrast produced by shaping the geometry of a whispering gallery mode (WGM) resonator. With this technique, single and multiply-coupled WGM resonators can be designed for a wide variety of applications.

It is reasonable to note that these new resonators are no longer pure WGMRs, but rather a hybrid incorporating the features of an optical planar waveguide, or a ridge waveguide [44, 45, 46], and a conventional WGM resonator. Single-mode WGM resonator is topologically different from these waveguides and the WGM feature is critical in achieving ultra high optical Q factor. The analysis of this cavity is based on the similarity with a single-mode gradient waveguide [47]. The resonators profile serves as a confinement structure, in analogy to the refractive index gradient in the single-mode optical fiber.

A single-mode homogeneous dielectric waveguide is realized when the frequency of the propagating light is close to the cutoff frequency of the channel. This means that the thickness of the waveguide approaches half the wavelength of light in the host material of the waveguide. It is impractical to fabricate a single-mode optical fiber by decreasing the fibers diameter. Instead, single-mode operation is ensured by the specially selected radial profile of the refractive index of the fiber material. The core of the fiber has a larger index of refraction than the surrounding cladding material. The difference of the indices is small, so only one mode propagates inside the core, while the others decay into the cladding (Fig. 3.1 (a)). For instance, the condition for the single mode operation of a planar waveguide is [48]

$$d_{co} < \frac{\lambda}{2\sqrt{\Delta\epsilon}}, \quad (3.1)$$

where d_{co} is thickness of the core, λ is wavelength of light in vacuum, and $\Delta\epsilon$ is the difference between the susceptibilities of the core and the cladding material, respectively. As a result, the core may have a reasonably large diameter. Note that the core of a single-mode fiber becomes a multimode waveguide when the cladding is removed.

Let us consider the WGM resonator as a multi-mode gradient waveguide [49] (Fig. 3.1 (b)). The resonator becomes an ideal single-mode-family resonator only if the waveguide is thin enough.

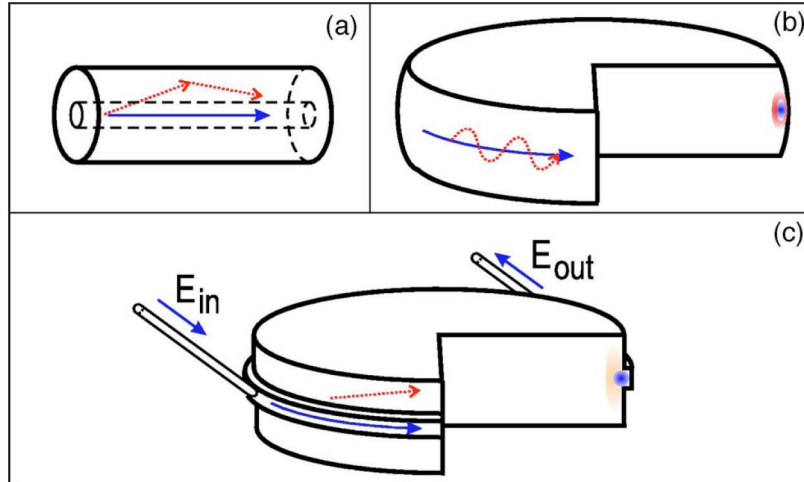


Figure 3.1: (a) Structure and mode localization in the optical fiber. Only one propagating mode, shown by the solid arrow, survives in the core of the fiber, while others (dotted arrows) penetrate into the cladding and dissipate. (b) Mode localization in the WGM resonator. The resonator corresponds to a multimode gradient fiber for which the index of refraction is set by the resonator shape, not by the change of the refractive index of the resonator host material, which is constant. Both the fundamental and the auxiliary modes survive. (c) Mode localization in a low-contrast WGM resonator. Only a single-mode family survives. The other modes penetrate into the cylinder rod and dissipate. The coupling to the single-mode family is achieved with, e.g., an angle-polished fiber coupler.

Following this trivial approach the WGM resonator should be designed as an approximately half-wavelength-thick torus to support a single-mode family. Recent experiments confirmed this conclusion and nearly single-mode resonators have been demonstrated [20].

There is another, nontrivial, approach to the problem based on the analogy with single-mode optical fiber. It is shown here that a WGM resonator made of any transparent material with any size can be transformed into a single-mode resonator if the appropriate geometrically defined core and cladding are developed (Fig. 3.1(c)).

To show that WGM modes can be described by use of a waveguide formalism, we start with the usual wave equation

$$\nabla \times (\nabla \times \mathbf{E}) - k^2 \epsilon(\mathbf{r}) \mathbf{E} = 0, \quad (3.2)$$

where $k = \omega/c$ is the wave number, $\epsilon(\mathbf{r})$ is the coordinate dependent dielectric susceptibility, \mathbf{E} is the electric field of the mode, and \mathbf{r} is the radius vector.

Higher-order WGMs (i.e., those with the wavelength much smaller than the resonator size) of both TE and TM kinds are localized in the vicinity of the equator of the resonator. Here cylindrical coordinates can be conveniently used. Applying the technique of separation of variables, and assuming that the resonators radius changes as $R = R_0 + L(z)$ ($R_0 \gg |L(z)|$) in the vicinity of

the equator, we transform Eq. 3.2, for TE mode family, to

$$\frac{\partial^2 E}{\partial r^2} + \frac{\partial^2 E}{\partial z^2} + \left[k^2 \epsilon \left(1 + 2 \frac{L(z)}{R_0} \right) - \frac{\nu^2}{r^2} \right] E = 0, \quad (3.3)$$

where ν is the angular momentum number of the mode (we assume that $\nu \gg 1$), $E(r, z)$ is the scalar field amplitude, and ϵ is the susceptibility of resonator material. Equation 3.3 is similar to the gradient waveguide equation. It is easy to see that, for instance, modes of a spherical WGM resonator coincide with modes of a gradient waveguide with parabolic distribution of the refractive index in the z direction. Hence it is the geometry of the surface that should be modified to produce an ideal single-mode WGM resonator. A core for the WGM waveguide can be obtained by proper design of the resonator's surface in the vicinity of the equator. The rest of the resonator body acts as the cladding (Fig. 3.1(c)).

Consider a resonator consisting of a cylindrical drum and a small, ring-like protrusion, $L(z) = L_0$ for $d \geq z \geq 0$, on its surface. The drum's effective susceptibility does not depend on the z coordinate and is equal to ϵ . The effective susceptibility of the ring, $\epsilon(1 + 2L_0/R_0)$ (see Eq. 3.3), is slightly larger. Therefore, the ring is the core that confines the light in the z direction, while the drum is the cladding. The condition for single-mode operation of the resonator by use of inequality (3.1) is:

$$1 > \frac{d}{\lambda} \sqrt{\frac{2L_0\epsilon}{R_0}} > \frac{1}{2}. \quad (3.4)$$

Condition (3.4) stays valid for a resonator with an arbitrary large radius. Both the width and the height of the ring can be much larger than the wavelength of light. The ratio L_0/R_0 acts the same way as the ratio $\Delta\epsilon/\epsilon$ in an optical fiber. The author of this dissertation has fabricated

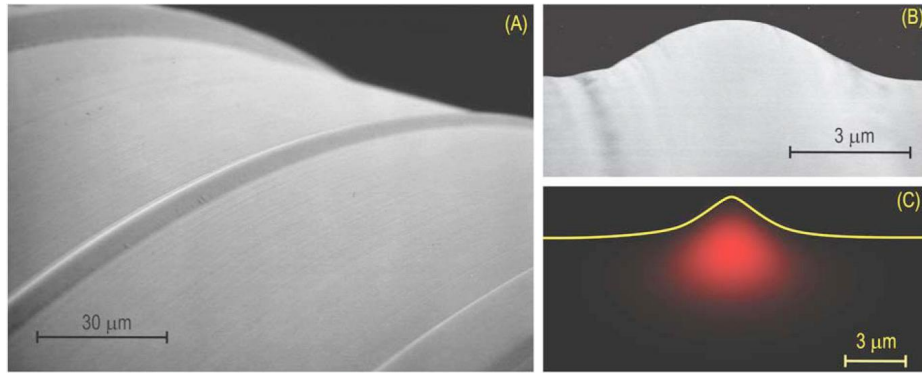


Figure 3.2: (A) Scanning electron microscope images of the resonator whose spectrum is shown in Fig. 3.4 and 3.5. The resonator has a nearly Gaussian shape, with $2.5 \mu\text{m}$ height and $5 \mu\text{m}$ full-width at half-maximum. (B) Image of the profile of the resonator shown in (A). (C) Intensity map of the field in the resonator shown in (A) simulated by numerical solution of Eq. 3.3.

a 5 mm diameter monocrystalline fluorite rod. The spectrum of such a rod is extremely dense,

having enormous number of modes in each FSR. A small ring with dimensions on the order of several micrometers was then fabricated on the surface of the cylinder by removing some additional material (Fig. 3.2). The resonator spectrum changed drastically. The resonator has a single TE

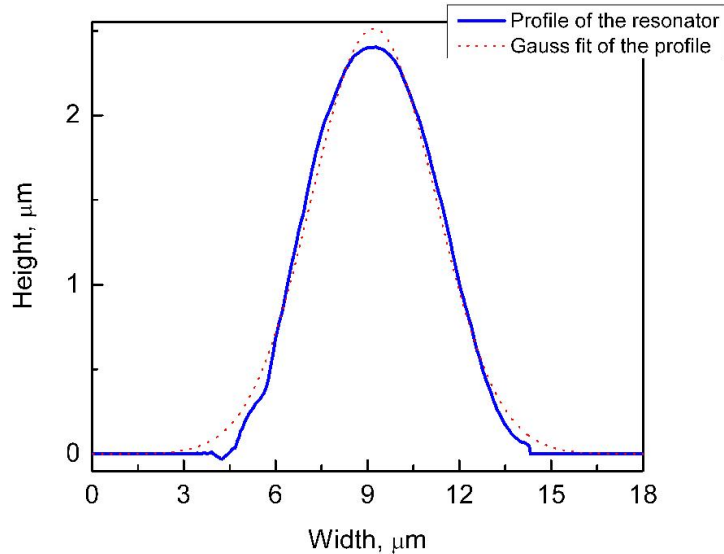


Figure 3.3: Geometrical profile of the resonator and a Gaussian fit

and a single TM mode family shifted by a few gigahertz relative to each other. A single TM mode family was selected by the polarization of incoming light. Loaded Q factors of both families of modes shown in Fig. 3.4 are equal to 8×10^6 . The particular resonator's Q-factor was limited by residual surface roughness. The profile of the resonator is nearly Gaussian, as shown in Fig. 3.3. The spectra shown on Fig. 3.4 and Fig. 3.5 were obtained with two angle-polished fiber couplers [25], one for the input and one for the output. The fiber couplers were made with a standard single-mode fiber with cladding diameter of about $150 \mu\text{m}$ and core of about $5 \mu\text{m}$. The photodetector signal represents transmission of the resonator. Logarithmic detector measurements have shown that besides the two mode families there were no other modes down to -30 dB level. It should be noted that, given the geometrical parameters of the resonator and the couplers, the single mode regime of this resonator is not a function of coupling but an intrinsic property. Here we present the spectrum of a multimode resonator made by the same technique on the same cylinder (Fig. 3.4(b)) to demonstrate that the coupling does not affect the observed mode structure. Moreover, the logarithmic measurements were performed in a loaded configuration, when the couplers are in contact with the resonator. Numerical simulation of resonator parameters were carried out as well, which clearly demonstrated that only the fundamental modes survive.

This kind of resonator could, in principle, be fabricated with lithium niobate, the refractive index

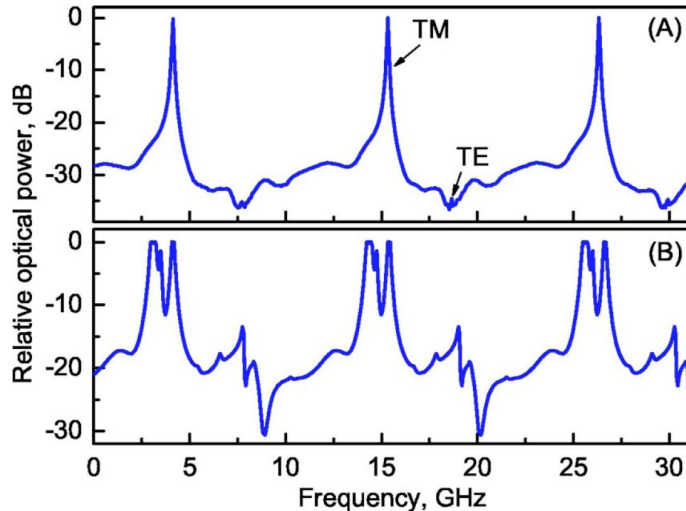


Figure 3.4: (A) Spectrum of a nearly ideal single-mode resonator obtained by use of a 980 nm laser, as well as the angle-polished fiber couplers (Fig. 3.1(c)). The mode number is approximately $\nu = 2 \times 10^4$. The low-Q modes on the spectrum background are the modes of the cylinder. (b) Spectrum of the multimode resonator made on the same cylinder ($2.5 \mu\text{m}$ height and $15 \mu\text{m}$ width) and detected with the same coupling technique. The resonator is partially visible in the lower right corner of Fig. 3.2(a).

of which can be controlled by applying an electric field. Such a resonator could be used for unique optical measurements and filtering applications.

The type of the dielectric medium used for the single-mode resonators is not important in achieving the single-mode regime as long as it is solid and transparent. Generally, as the behavior of the system is defined only by the systems geometry, it is not even important for what kinds of wave the structure is a resonator. Microwave, acoustical, or mechanical chains of resonators of this type have the same features and basis of design as their optical counterparts.

With the approach described here, one can make a single-mode optical WGM resonator of any size. A resonator the size of an orange requires a ring with a dimension of tens of micrometers for single-mode propagation of $1 \mu\text{m}$ wavelength light. This is counterintuitive because the size of the single-mode channel is much larger than the wavelength. This type of experiment may be interesting in fundamental research investigations. For practical applications, small resonators are of more interest.

In conclusion, the high density of modes in spherical and cylindrical WGM resonators has limited their usefulness in optical science and technology. Light sent into these cavities occupies a large multiplicity of overlapping and possibly interacting modes, thus complicating device performance and limiting the accuracy of physical measurements. A single-mode family resonator that avoids this pitfall by design is demonstrated. By engineering the photonic density of states to minimize interaction between the modes and force all input energy into one eigenstate, science is provided with

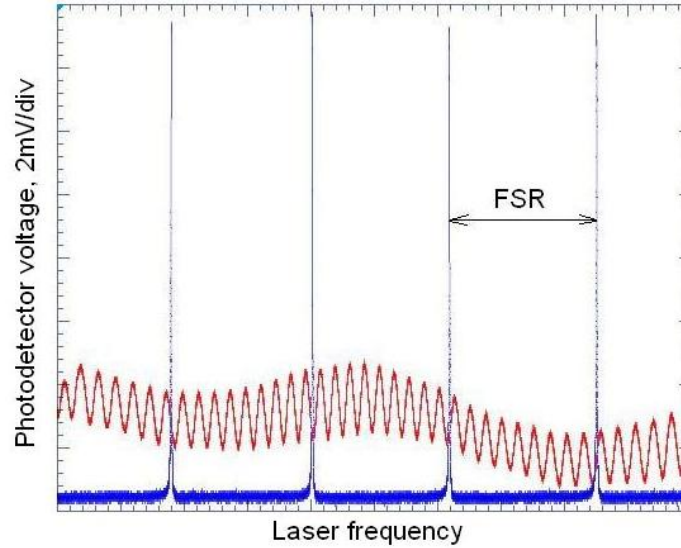


Figure 3.5: Linear spectrum that contains transmission of the resonator represented by modes with spacing of around 11 GHz and that of the reference 1.2 GHz Fabri-Perot etalon

a new tool with which to study the threshold dynamics of nonlinear and quantum optical processes and for sensing chemical concentrations and fluid flow. It also creates a new class of photonic circuit elements that could expand the capabilities of communications technology.

3.2 Coupled resonators

A single-mode cavity was fabricated on a fluorite cylinder along with two other cavities shown on Fig. 3.6, which had larger dimensions and supported more than one mode per FSR. These cavities were fabricated at separations of around $70\ \mu\text{m}$ and $140\ \mu\text{m}$ from the single-mode cavity, which was deemed far enough for these cavities to be independent, given the wavelength of light used to excite resonances is $1\ \mu\text{m}$. Coupling to the resonators was achieved by means of an angle-polished fiber coupler [25]. Modes were excited in a multimode cavity by scanning laser frequency over several tens of gigahertz, which corresponded to about two cavity FSR. Some of the energy was resonantly transferred to a single-mode cavity as it happened to have modes at the same frequency as some of the modes in a multimode cavity. This resonant energy transfer is mediated by an evanescent field of the modes which spreads out to a comparatively large distance inside the crystalline cylinder. Coupling over such a large distance is spectacular and may be explained by a high quality factor of participating modes. This effect may be used for delay lines, where multiple resonators are fabricated in a way similar to Fig. 3.6, as was theoretically proposed recently [50]. Realization of the delay lines seems feasible if the precision of the fabrication process is adequate.

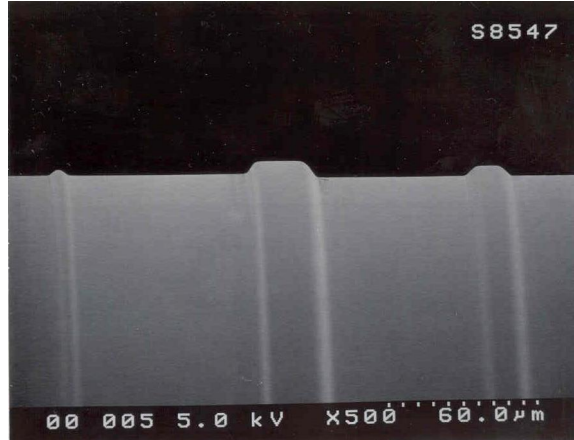


Figure 3.6: Three resonators: single-mode (on the left) and two multimode cavities. Cylinder diameter is 5 μm .

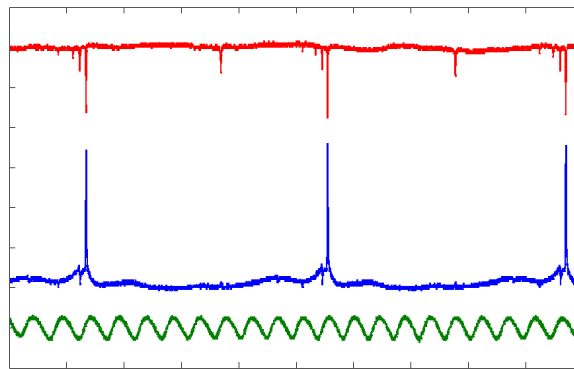


Figure 3.7: Resonant coupling of two resonators separated by $70 \mu\text{m}$ via an evanescent field inside the cylinder. Upper spectrum represents the reflected signal from a middle resonator on Fig. 3.6. Middle curve is the output of the single-mode resonator. Lower spectrum is a transmission of a reference 1.2 GHz Fabry-Perot etalon.

3.3 Crystalline microcavities, Q factor, and tunability

Starting with a cylinder 1.5 mm in diameter it was possible to fabricate cylinders as small as $40 \mu\text{m}$ and then formulate a waveguide on the surface. The diameter of the resonators can be as small as a few tens of microns and their geometrical features, such as surface curvature or profile, can be precisely engineered. Resonators were polished after the diamond-turning step to improve optical Q factor. CaF_2 resonators as small as $100 \mu\text{m}$ in diameter having quality factor $Q = 4 \times 10^8$ were fabricated from magnesium and calcium fluoride. Some of these cavities are shown in Fig. 3.8.

The fabrication process includes two steps. The first step is the diamond-turning process, which employs computer control of a precision lathe. The structures obtained at this step are engineered to about 40 nm precision and have optical Q factors of up to 10^7 . If higher Q factors are needed, additional optical polishing has to be performed. This polishing step naturally modifies the structure that was initially obtained by the diamond-turning process.

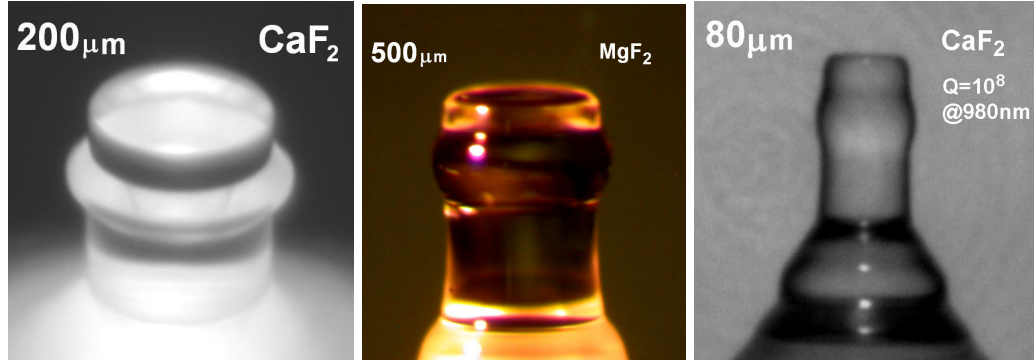


Figure 3.8: Crystalline microresonators

Special diamond-turning regimes should be employed to avoid brittle machining and to achieve a required smoothness of the surface. Such parameters as speed of rotation of the workpiece, feed and cutting angle, diamond cutter geometry and sharpness, as well as lubricant, are very important in achieving ductile regime of machining [51]. Special attention should be paid to vibration isolation of the turning process. In our diamond-turning setup we use a homemade air bearing to provide the required stiffness and repeatability of workpiece rotations. A commercial brushless motor and a simple magnetic clutch are used to rotate the bearing. Polishing with polycrystalline diamond abrasives is performed in several steps with decreasing diamond grit sizes followed by the cleaning process. It was found that small particles are extremely difficult to remove from the surface of the material. The cleaning process is the most critical in achieving ultrahigh Q factor. Cleaning was performed in a clean-room environment with use of organic solvents.

The optical Q factor of the resonators after polishing is limited by contributions from four main sources: scattering by the dust particles accumulated on the resonator surface, absorption in the resonator material, radiation leakage, and surface scattering. We assume that the optical power circulating inside the resonator is below the threshold of nonlinear effects, such as Raman lasing or thermo-optical instability [52].

Scattering by the dust particles would be the main restriction on the quality factor if a clean-room environment is not provided. Once inside the clean room environment or vacuum, the Q factor can be preserved on a very high level for a long time. Aside from dust accumulation, optical polishing leaves some amount of nanoparticles embedded into the resonator surface.

It is known that water is detrimental for the Q factor of fused silica devices due to formation of irregularly adsorbed layers [53]. Fortunately, such crystals as CaF₂ and MgF₂ have chemical properties that reduce accumulation of water on the surface. Diffusion of water into crystalline lattice is inhibited, while a monomolecular layer of water is always present on the surface.

The intrinsic absorption of the resonator material is the second important effect restricting the value of the measured Q factor. The absorption is a function of the crystal-growing process and is

defined by the optical properties of a crystal at a given wavelength. This parameter is particularly small in crystalline materials, since they can be produced with high purity. Recent developments in UV lithography have stimulated the production of extremely pure CaF_2 monocrystals. However, even in those purest crystals the reference-sheet absorption rarely falls below 10 ppm/cm, which corresponds to quality factors on the order of 10^{10} . Unfortunately, not much data are available for the optical absorption coefficients, since there is no technique capable of measuring this coefficient with high precision when absorption becomes very weak. Interestingly, the WGM resonators may be used to measure internal absorption with good precision if the Q factor is known to be limited only by internal absorption. For example, the absorption coefficient reported by the crystal producer is $\alpha = 2 \times 10^{-5} \text{ cm}^{-1}$. According to the expression for the internal absorption limited Q factor $Q = 2\pi n/(\alpha k)$, this corresponds to $Q = 4.2 \times 10^9$ at wavelength of $\lambda = 1064 \text{ nm}$. Here, n is the refractive index of material. On the other hand, with this piece of crystal the author has measured $Q = 5.3 \times 10^{10}$, which gives a more accurate upper limit estimate of absorption coefficient $\alpha = 1.6 \times 10^{-6} \text{ cm}^{-1}$.

The radiation leakage is significant only for the resonators with extremely small diameters not exceeding several micrometers, which is not the case in our study.

Finally, the surface roughness is made small by our polishing technique, as confirmed by measurements with an atomic force microscope (AFM). In its contribution to surface scattering factor, the surface roughness is accompanied by the subsurface material damage. This damage is represented by the microfractures and embedded particles and is usually confined within a shallow surface layer of the material. The thickness of this layer is determined by the polishing and grinding process. AFM studies have shown the small amount of diamond particles embedded into the resonator surface. This could be useful in quantum optics, since a quantum dot containing diamonds or other nanoparticles can be embedded this way to create a coupled system without noticeable degradation of Q factor.

The author has fabricated a calcium fluoride resonator with $100 \mu\text{m}$ diameter and optical Q factor of 4×10^8 , as derived from resonant curves shown on Fig. 3.9. The surface roughness does not restrict the value of the quality factor. The measurements performed with AFM showed that the surface roughness of small resonators is about the same as for the large disks with Q factor of 10^9 and is practically negligible. Let us estimate the maximum Q factor that could be achieved in the resonators with measured surface roughness. We will use the previously derived [54] expression:

$$Q \simeq \frac{3\lambda^3 a}{8n\pi^2 B^2 \sigma^2} \quad (3.5)$$

where λ is the wavelength, a is the radius of the resonator, n is the refraction index of the resonator material, B is the correlation length (length of exponential decrease of the autocorrelation function

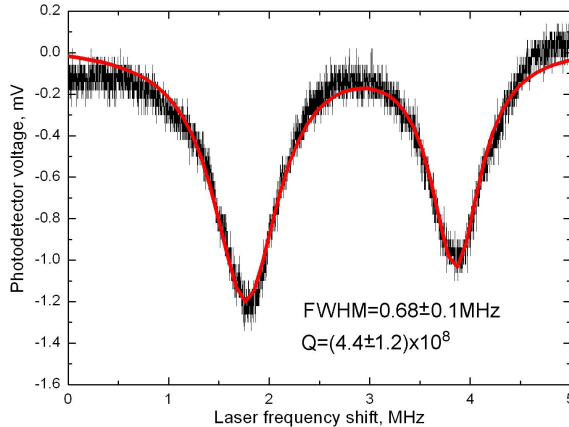


Figure 3.9: Resonant curve with Lorentzian fit for CaF_2 resonator $100\ \mu\text{m}$ in diameter. Rayleigh-scattering-induced splitting is present.

for surface height), and σ is the roughness (standard deviation of surface height). Let us assume that $\lambda=1\ \mu\text{m}$, $a = 50\ \mu\text{m}$, $n = 1.43$, $B = 2\ \text{nm}$, and $\sigma = 0.33\ \text{nm}$. For this set of parameters, we obtain $Q = 4 \times 10^{12}$. The estimated value of the Rayleigh-scattering-limited Q factor scales proportionally to the radius and is still much higher than any Q factor observed in WGM resonators. The resonator was fabricated with vacuum UV grade CaF_2 and its Q factor was limited by residual contamination of the surface with polishing agents. It was found that when an excimer grade CaF_2 is used, it is possible to achieve a Q factor higher than in any other open resonator and any other WGM resonator. The 5.5-mm-diameter CaF_2 WGM resonator was fabricated with Q factor of $(5.31 \pm 0.04) \times 10^{10}$ measured with a Nd:YAG laser at wavelength of 1064 nm. Even higher Q factors were achieved in our laboratory. In microresonators, the role of Rayleigh and surface scattering becomes more important, so the Q factor is lower for smaller cavities [54].

3.3.1 Tuning crystalline microresonators by mechanical deformation

Ability to tune frequencies of WG modes of crystalline microresonators is beneficial for quantum optics and other experiments. Tuning of fused silica resonators by mechanical deformation has been previously demonstrated [55]. Tuning by an electric field via Kerr effect may also be used. The author and V.S. Ilchenko have carried out an experiment on tuning the WG modes by mechanical pressure. The $500\ \mu\text{m}$ resonator made with MgF_2 was installed onto a piezo element and clamped under slight pressure as shown on Fig. 3.10. By adjusting the piezo voltage we were able to reversibly shift the WGM frequencies with a sensitivity of around 1 GHz/V (see Fig. 3.11). To couple light in and out of the resonator, the angle-polished fiber couplers were used [25]. Tuning by as much as 100 GHz was possible but finally led to damage of the resonator. Similar experiments with a 5 mm CaF_2 resonator in a different setup showed tunability of around 10 MHz/V. These results show that if tunability of a crystalline microresonator is required, it can be achieved by accurate mechanical

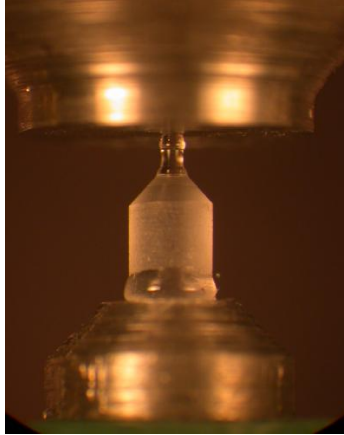


Figure 3.10: MgF_2 resonator is deformed along its axis with a piezo element. Resonator diameter is $500\ \mu\text{m}$.

deformation of the crystal.

3.3.2 Precision spectroscopy of single ions

Ultrahigh Q crystalline microresonators with small mode volumes are suitable for applications in quantum cavity electrodynamics and quantum optics. For instance, the resonators could be used to demonstrate the strong coupling between a WGM and an atom, or to modify the spontaneous emission of an atom interacting with the WGM. Various quantum optics experiments become possible with the new microresonators as the combination of high Q and small mode volume make it easier to utilize optical nonlinearities of the crystalline material. It may be possible to arrange for an interaction of single ions in a crystalline lattice and the optical WG mode leading to such intriguing applications as a single ion clock without a magneto-optical trap. In this section we consider spectroscopy of a single ion in a doped crystalline microresonator as a possible application.

The dopants in crystalline WGMR are influenced by the host material of the resonator and by the WGM field structure. The absorption profile of each individual doping ion is broadened homogeneously through interaction with lattice phonons and shifted through the influence of the crystalline lattice. This inhomogeneous shift of transition frequency is caused by the slight differences in electronic configurations at the various lattice sites, which create different electric fields for each individual doping ion. The observed inhomogeneous broadening of atomic transition profile in a crystalline host is caused by these shifts. The spectrum of the doping in a crystal is formed as a combination of many overlapping but relatively shifted spectra of single ions. Inhomogeneous broadening varies over a wide frequency range for different host materials. In most crystals the absorption lines of atomic impurities get narrower with decreasing temperature. At liquid helium temperatures the phonon-originated homogeneous broadening fades, leaving the inhomogeneously

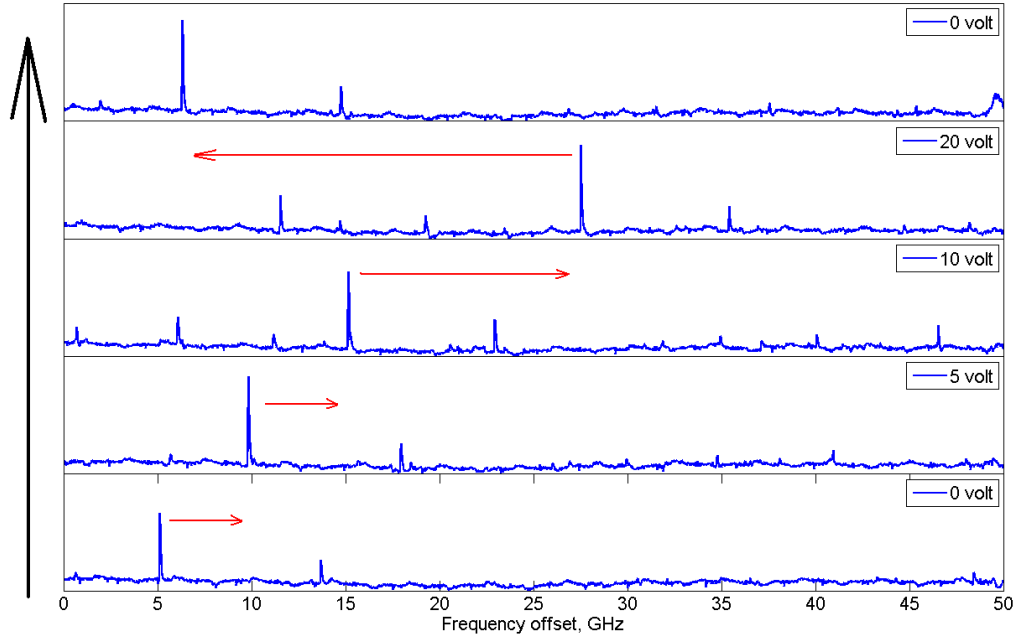


Figure 3.11: Resonator spectrum during mechanical deformation. Lower spectrum corresponds to zero voltage applied to the piezo element. Voltage was increased to 20 V gradually and then reduced back to zero. Some permanent deformation took place as the mode on the upper graph is displaced as compared to the lower graph.

broadened impurity absorption line with greatly increased intensity. These so-called zero phonon lines make it possible to optically detect single impurity molecules or ions in such crystals [19] using the single molecule spectroscopy techniques. The application of the WGM crystalline resonators may be fruitful for this kind of single ion spectroscopy. Rare earth ions are convenient for observation of the effect because they have many zero phonon line transitions, and relatively strong associated dipole moments for selected transitions. For example, a Sm^+ ion in CaF_2 has a dipole moment of 0.63 D for $\lambda=709$ nm transition [56], which is comparable to organic molecules of pentacene in p-terphenyl matrix, 0.7 D at $\lambda=592$ nm [57]. Debye is a non-system unit of electric dipole moment. It is equal to the electric dipole moment created by the two charges of 10^{-10} Franklin (or esu) separated by 10^{-10} m ($1D = 10^{-18}$ Fr cm = 3.3356410^{-30} C m).

The WGM can be used to observe the absorption profile of a single ion if a small enough resonator is doped with rare earth ions in low concentration. At low temperatures the absorption profile of the dopant ions transforms into a “forest” of absorption profiles, corresponding to the individual ions. If the modes of the resonator are scanned over the absorption profiles of the ions, one may expect to observe the interaction of individual photons in a WGM and an ion, resulting in quantum effects such as Rabi splitting [58]. The frequency of a WGM can be shifted by use of nonlinear properties of the resonator material (e.g., electro-optical effect in lithium niobate) or by a change of the resonators geometry (see, e.g., Sec. 3.3.1).

Alternatively, a first step towards this experiment, which requires a very low light level and photon counting, may be the spectroscopy of a very low dopant concentration with large resonators. The Q factor of a 5 mm resonator is limited by dopant absorption. By measuring the Q factor over the span of wavelengths that includes the absorption peak, it may be possible to detect such peak even for very small concentrations, such as 10 ppb.

Let us estimate the efficiency of coupling of a single ion and a WGM for the resonators at hand. Consider a CaF_2 resonator with diameter of $100 \mu\text{m}$ and optical Q factor of 4×10^8 . Assume that it is doped with rare earth ions that have an electric dipole transition moment of $\mu = 1 D$ at a wavelength of $1 \mu\text{m}$ ($\nu = 3 \times 10^{14} \text{ Hz}$, $\omega = 2\pi\nu$). The CaF_2 refractive index at this wavelength is $n = 1.43$. Let us assume that we have only one such ion inside the volume occupied by the WGM and that it is located at the point of maximum of the electric field of the WGM. The single photon Rabi frequency and a strong coupling condition may be written as follows:

$$\Omega_r = \frac{\mu E}{\hbar}, \quad \Omega_r \gg (\gamma_{cavity}, \gamma_{rad}). \quad (3.6)$$

Here γ_{cavity} and γ_{rad} are the cavity decay rate and the atomic radiative decay rate. E is the electric field amplitude (CGS units) resulting from a single photon stored in the WGM [59]

$$E = \sqrt{\frac{2\pi\hbar\omega}{V_{eff}n^2}}, \quad (3.7)$$

where the effective volume of the mode V_{eff} can be derived using expression 1.14 from Sec.1.2.2. The formula for the volume is derived for silica microspheres and is assumed to be appropriate for our case, as the shape of an active region of our resonator is close to spherical. For the given parameters of the resonator we have $l = m = 422$ and $V_{eff} = 2 \times 10^{-9} \text{ cm}^3$. The single photon Rabi frequency is then $\Omega_r/2\pi = 8 \text{ MHz}$, which is significantly larger than the radiative decay rate $\gamma_{rad} = 71 \text{ kHz}$ and the cavity decay rate $\gamma_{cavity} = 0.7 \text{ MHz}$. Thus the strong coupling condition (3.6) can be realized. The radiative decay rate of an ion embedded in a lossless dielectric and the cavity decay rate were calculated using the following expressions [59]

$$2\pi\gamma_{rad} = \frac{4n\mu^2\omega^3}{3\hbar c^3}, \quad 2\pi\gamma_{cavity} = \frac{\omega}{Q}. \quad (3.8)$$

The idea of coupling a WGM cavity mode to optical transitions of ions is not new by itself. State of the art demonstration of this idea has recently been published [60]. The novelty of the idea discussed here is in the way the ions are coupled to WGMs, and in potential advantages a combination of zero phonon lines and crystalline cavities may bring. The optical cavity and the atomic trap are combined in a single crystalline microresonator. Taking into account the possibility of making smaller resonators with higher Q factors and a wide range of available inorganic dopants, we see

that crystalline WGM resonators open new horizons in quantum optics and atomic physics.

3.4 Resonators with reduced spectrum

In some situations it is desirable to obtain a high-Q-factor resonator which would have as few modes per FSR as possible and a relatively large diameter of around 5 mm. Such a resonator may be fabricated without the diamond-turning procedure. A simple polishing may produce a high-Q cavity with a light-guiding surface curvature radius as small as $10\ \mu\text{m}$ or even less. Calcium fluoride

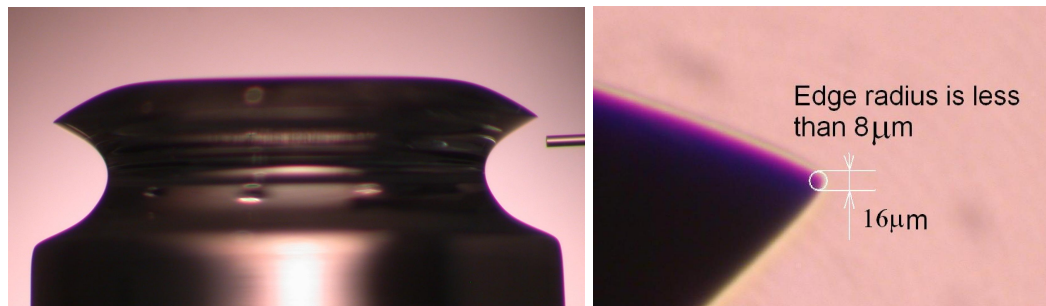


Figure 3.12: Resonator having small radius of curvature of the light guiding surface. Single mode fiber tip with $125\ \mu\text{m}$ diameter is present on the left photo for scale. Shadow photograph on the right represents resonator's edge and contains a $16\ \mu\text{m}$ diameter circle for scale. Such resonators approach single mode regime.

is a crystal with cubic lattice. It has a mechanical hardness anisotropy which leads to uneven removal rates during polishing and consequently to a surface that deviates from circular. This effect may be reduced to a minimum if special polishing conditions are applied. The resonator shown in Fig. 3.13



Figure 3.13: Fluorite resonator with narrow edge and a single mode fiber for scale.

and 3.12 may approach single-mode regime if the coupling element is small. An angle polished fiber coupler may be used. In this case the coupling may be adjusted so that only the fundamental mode is efficiently coupled and the observed spectrum has only several modes per cavity FSR.

Chapter 4

Optical quality factors of crystalline cavities

Optical quality factor Q is one of the most important parameters of the WGM resonators. These resonators demonstrate the highest optical Q ever achieved in resonators. The only notable exception are 4-kilometer-long LIGO interferometers. In these large Fabri-Perot resonators Q factor is proportional to resonator length.

For a linear oscillator, Q is numerically equal to the ratio of frequency to the width of the resonance curve at the level where amplitude decreases to $1/\sqrt{2}$ of its maximum: $Q = \omega/\Delta\omega$. Alternatively, $Q = \omega W/P$, where W is the energy stored in an oscillator and P is a power of losses. Quality factor determines the frequency discriminating ability of a system. In optical cavities it also defines how long a photon is stored in a cavity on average: $\tau = Q/\omega$ — cavity ringdown time. In a cavity with radius a and refractive index n the resonant increase of the intracavity intensity I_c over the input light intensity I at a free space wavelength λ is proportional to the Q factor: $I_c/I_0 = Q\lambda/(\pi^2na)$. For crystalline cavities presented in this dissertation this intensity may be increased by a factor of more than 10^7 . Even higher values may be possible in the future.

There are two basic methods of Q factor measurement for optical WGM resonators. One method measures the cavity ringdown directly or indirectly. A cavity mode may be excited and the excitation may be disabled much faster than the expected cavity ringdown time. The resonator will then continue to emit optical energy with exponentially decaying power. The time constant is the cavity ringdown time. This method requires good optical shutters, for which various electro optical and acousto-optical modulators may be used. In another method a laser having a linewidth narrower than the expected cavity resonance is scanned in frequency over a window which is expected to contain a resonance of the cavity. Recording the cavity response provides one with a Lorentzian-shaped curve, the width of which can be measured directly, thus providing a Q factor. Here a good laser is required and the measurement power must be low to avoid nonlinear processes in the resonator. There are also indirect methods for Q factor measurement. These include derivation of

cavity Q from the stimulated Raman scattering (lasing) threshold and a homodyne method. In the latter, the laser frequency is scanned quickly over the resonance and the cavity emission is mixed with laser. This produces oscillations with growing frequency and exponentially decaying amplitude (see Sec. 4.2.3 for an example).

The following sections provide examples of measurement of the record optical Q factors in crystalline WGM resonators. Theoretical analysis of Q factor limitations is also presented. Section 4.1 is based on a paper by I.S. Grudinin, V.S. Ilchenko, and L. Maleki published in *Physical Review A* [3]. Section 4.2 is a transcript of a paper by I.S. Grudinin, A.B. Matsko, and L. Maleki published in *Optics Express* [4]. Material is reproduced with permissions from APS and OSA.

4.1 Q factors of CaF₂ cavities in linear regime

Experimental demonstration of a record optical quality factor of $(6.3 \pm 0.8) \times 10^{10}$, corresponding to cavity ring-down time of $\tau \simeq 36 \mu\text{s}$, is made possible by avoiding nonlinear effects in a crystalline whispering-gallery-mode resonator. Various loss mechanisms in CaF₂ cavities and ways of achieving higher quality factors are discussed.

4.1.1 Introduction

Long storage times or long effective optical path lengths are important for efficient nonlinear interactions and for cavity quantum electrodynamics (CQED) experiments. It has been shown that extreme material purity and higher nonlinearities of crystalline WGM resonators may provide improved photon confinement times [30], enhanced second harmonic generation [31] and low threshold hyperparametric oscillations [61].

The interest in ultrahigh quality factors in support of new applications of WGM resonators requires new strategies for the fabrication and characterization of the resonators. The Q factor, for example, is commonly measured using either cavity ringdown or linewidth calibration techniques. The presence of strong nonlinear processes makes it difficult to properly determine the Q with these traditional techniques. The nonlinear processes include thermal and Kerr nonlinearities, stimulated Raman scattering and thermo-optical instability, all of which can influence an accurate determination of the intrinsic Q.

The purpose of the present work is to study the ultimate limit of the Q of the crystalline resonators and describe techniques for measuring ultrahigh values. The outline of the section is as follows. The results of Q factor measurements at three wavelengths are presented, including a record value for the quality factor of a WGM resonator. Difference in cavity resonance curves obtained at different pump power levels are also demonstrated. In the next section we analyze loss mechanisms that limit the Q factor of crystalline cavities and give estimates for CaF₂ resonators. In the section on the nonlinear

processes we discuss the influence they have on the shape of a resonant curve. The thresholds for Raman lasing, thermo-optical oscillations, thermal, and Kerr bistabilities are also discussed. It is shown that it is only possible to measure ultrahigh Q in the linear regime, by lowering the optical power. In the final section we discuss the role of impurities and means for achieving higher optical Q factors in crystalline cavities, together with some potential applications.

4.1.2 Fabrication of the WGM resonators



Figure 4.1: CaF_2 cavity with a record Q factor of $(6.3 \pm 0.8) \times 10^{10}$, 5.5 mm in diameter. White brackets show the area of WGM localization.

Crystalline WGM resonators were fabricated with a novel technique developed in our laboratory. A small cylinder is first cut out of a crystalline window. The axis of the cylinder coincides with the window axis, which is along [111] crystalline orientation. This cylinder is mounted onto an air bearing spindle of a home-made diamond-turning apparatus. Diamond cutting of a desired profile is performed with a precise computer-controlled lathe. This step produces resonators with optical Q factors of about 10^7 . The next step involves hand polishing with a sequence of diamond abrasives of decreasing grit sizes. A thorough cleaning procedure is performed after each polishing step. An example of a resonator is shown on Fig. 4.1. This fabrication technique is applicable to many optical crystals due to the versatility of the diamond grinding process. Resonators may be fabricated with any diameter down to a few tens of microns (Sec. 3.3). Moreover, many resonators may be fabricated on the same rod with small separations (Sec. 3.2). The resulting resonator chains may be utilized in filtering and other applications and are similar to coupled pendulums in mechanics [50].

4.1.3 Measurement of a Q factor

The author has measured the optical Q factor of CaF_2 resonators at laser wavelengths of 1064 nm and 1550 nm using direct observation of cavity resonances. Measurements were also performed at 780 nm

using a homodyne method (Fig. 4.2). Noise from our 780 nm grating-stabilized diode laser made it impossible to resolve the resonance curve directly. In a homodyne method, Q factor is derived from the decay time of the interference pattern formed by two beams. The first is the laser beam with its optical frequency linearly dependent on time and the second beam is the cavity emission. As the laser frequency is scanned, at some point it excites a cavity mode and stores some energy in it. This energy will then be emitted into the coupling element as a single-frequency, exponentially decaying optical beam. Interference of this beam with the laser beam results in exponentially decaying oscillations, from which a decay time may be extracted and the Q factor computed according to $Q = \omega T/2$ (Fig. 4.2).

In order to achieve the flexibility of using various wavelengths of light we utilized a conventional prism coupler to excite the modes of the cavity. The critical coupling efficiency was above 30 % at all wavelengths. All measurements were performed in a strongly undercoupled regime, where only a small fraction of light enters the cavity, leaving the measured Q factor close to the intrinsic value.

The 1064 nm Lightwave Nd:YAG and 1550 nm Coheras Adjustik lasers have narrow line of a few kilohertz, which made it possible to use direct observations of cavity resonances. Laser frequency was modulated with an internal piezo actuator. Signal generators were used to feed the sum of two signals to the laser head. The first is a sawtooth-shaped voltage for scanning the frequency back and forth over the cavity resonance. The second is a weak sinusoidal signal at 100 kHz for sideband modulation of the laser carrier. Sideband modulation provides calibration peaks shifted by 100 kHz both ways around the cavity resonance frequency. These peaks were recorded simultaneously with the cavity resonance curve and used for frequency calibration. A direct high-frequency modulation of the laser carrier through an internal piezo element results in a weak amplitude modulation. This amplitude modulation was rejected by the detector with long response time. Example of the Q factor measured with this method is shown on Fig. 4.3. The best value measured at 1550 nm was $Q = 1.1 \times 10^{10}$. The quality factor was also measured for a 1.5 mm CaF_2 cavity at 1064 nm and found to be 4×10^{10} . In a fluoride microresonator 100 μm in diameter values as high as $Q = 4 \times 10^8$ were found to be achievable for a UV-grade material at 1064 nm. The free spectral range of our cavities comprises many WGMs and the process of measurement included a search for the modes with the highest values of Q.

4.1.4 Q factor and pump power

In order to observe the influence of the input optical power that was used to excite the WGMs on the effective Q factor, we performed a series of measurements for a selected cavity mode. Measurements were performed for coupled pump power levels ranging from a few nanowatt to a microwatt. For each power level the laser was swept over the cavity resonance twice, first as its frequency was decreasing and second as it was increasing. This produced two resonant curves for each pump power level.

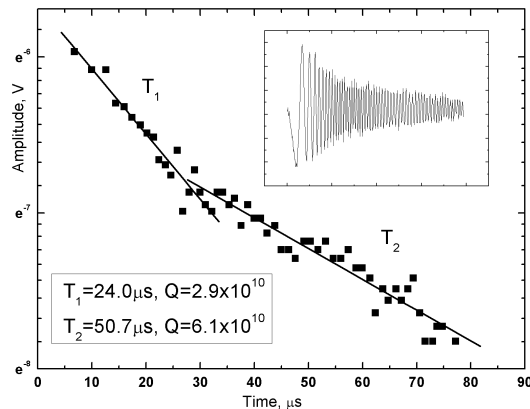


Figure 4.2: Example of “self-homodyne” measurement of ringdown time at 780 nm at low power. The insert shows the exponentially decaying oscillations resulting from the interference of the laser beam and the cavity emission.

Quality factors were obtained by fitting the cavity response curves to a Lorentzian for both laser frequency scan directions. We fit the dependence of the quality factor on power to exponentials for illustration — to delineate the data points. These exponentials converge to a single value of Q for low optical power, as expected. It should be noted that the intrinsic Q factor of a cavity generally should not depend on the optical excitation power. The observed divergence is generated by the method used to derive the Q factors. Fig. 4.5 serves to clarify this statement. It represents four measurements of the same WGM at coupled pump powers of 60 nW and 1 μ W. These measurements correspond to points A,B,C,D in Fig. 4.4. For the upper trace the pump power is well below the threshold of nonlinearities and the resonant curve is Lorentzian. For the lower trace the higher pump power causes the curves to deviate from the Lorentzian shape and become non-symmetric. The asymmetry arises from thermal nonlinearity, which in our case causes the cavity eigen-frequency to decrease as the laser beam begins to heat up the cavity material. As will be discussed in the following sections, measurements A and B correspond to a power level that is below the Raman lasing threshold, and thresholds of other nonlinear effects. For these measurements one may observe the linear oscillator response independent of the direction of the frequency scan and thus be able to obtain a reliable estimate for the cavity’s intrinsic Q factor. Occasional deviations from a Lorentzian were still observed, due to the acoustic noise perturbations and the high-pass filter in the AC-coupled input of the oscilloscope.

4.1.5 Losses in crystalline cavities

Given the Beer-Lambert law for light absorption $I(x) = I_0 e^{-\alpha x}$, which holds when the nonlinear optical processes are not present, the maximum value of the optical Q factor of a dielectric WGM

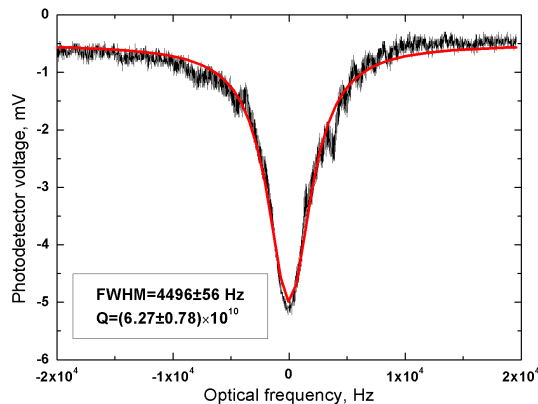


Figure 4.3: CaF₂ cavity resonance showing record optical Q factor and a Lorentzian fit. Measured at a coupled pump power of 100 nW in a strongly undercoupled regime. Out-of-resonance photodetector level is -0.5 mV.

resonator is given by

$$Q_{max} = \frac{2\pi n}{\lambda\alpha}. \quad (4.1)$$

Here α is a total optical loss coefficient in nepers per meter, which is a measure of the cumulative attenuation caused by different mechanisms:

$$\alpha = \alpha_{ss} + \alpha_{mat} + \alpha_{coupling} + \alpha_{rad}. \quad (4.2)$$

The contributions from several loss mechanisms are added: surface scattering, material losses, influence of the coupler, and the radiative loss. Surface scattering is induced by the imperfections of the surface. Material losses are caused by the fundamental absorption in the material, atomic impurities, and three types of bulk scattering: Raman, Brillouin, and Rayleigh. Radiative loss is only significant in small microresonators. The coupler losses can be made small by performing measurements in a strongly undercoupled regime.

4.1.5.1 Surface scattering

Surface roughness may be induced by frozen capillary waves, as in the case of the fused silica resonators, or by imperfections of polishing, in the case of crystalline resonators. In addition, some amount of micro- and nano-particles is almost always present on the surface of a resonator. One approach of estimating the surface-limited Q factor uses surface roughness (standard deviation σ) and B — length of exponential decay of surface autocorrelation function [54]:

$$Q_{ss} = \frac{K_{TE,TM}}{(K_{TE,TM} + 1)} \frac{3\lambda^3 a}{8n\pi^2 B^2 \sigma^2}. \quad (4.3)$$

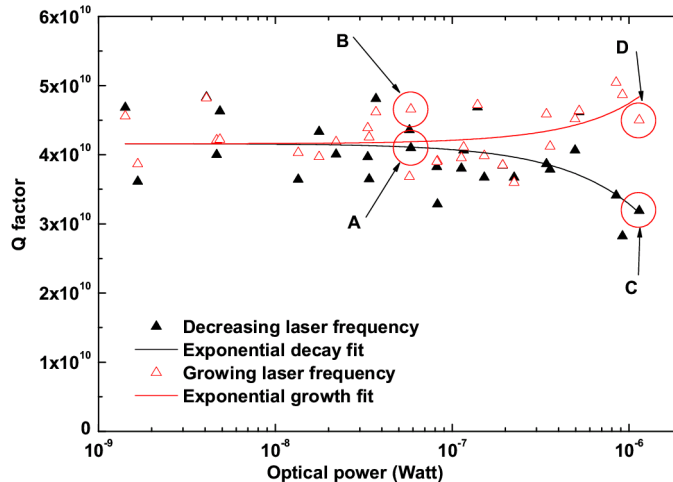


Figure 4.4: The quality factor measured by fitting the cavity response curve to a Lorentzian for several pump power levels. Measurements at points A,B,C,D were used to build Fig. 4.5.

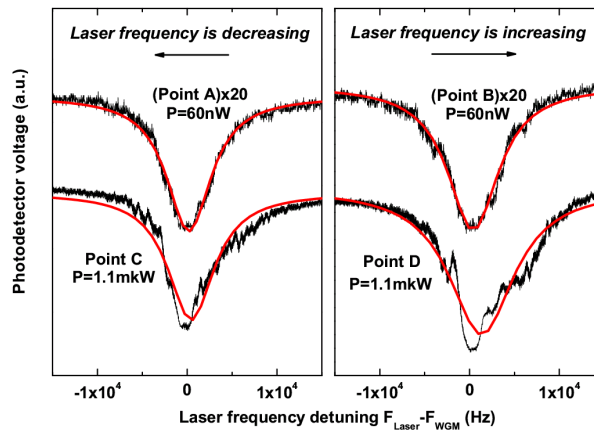


Figure 4.5: Cavity resonances recorded at pump power $P \simeq 60 \text{ nW}$ and $P \simeq 1 \mu\text{W}$. Red traces show Lorentzian fit. It can be seen that the resonance curves are not Lorentzian for higher values of the input power.

Here $K_{TE} = 2.8$, $K_{TM} = 9.6$ are scattering suppression coefficients for TE and TM whispering gallery modes in fused silica. Since the refractive index of fused silica $n = 1.45$ is close to that of CaF_2 , $n = 1.43$, we shall use fused silica suppression coefficients for our estimates. The formula was obtained as an approximation which takes the correlation length to be much smaller than the wavelength of light ($\sigma B^2 \ll \lambda^3$). We may use this equation to analyze the atomic force microscope (AFM) images of CaF_2 resonators taken in the WGM localization area (Fig. 4.6). Since noise due to the AFM and that of the surface roughness are independent, the variance of the image data is a sum of the surface and noise variances $\sigma_{image}^2 = \sigma_{surface}^2 + \sigma_{noise}^2$. Given the AFM empty image (noise) standard deviation of $\sigma_{noise} = 0.07 \text{ nm}$ we calculate surface roughness σ for the left and right image to be 0.186 nm and 0.151 nm , correspondingly. Calculations were made with a standard expression

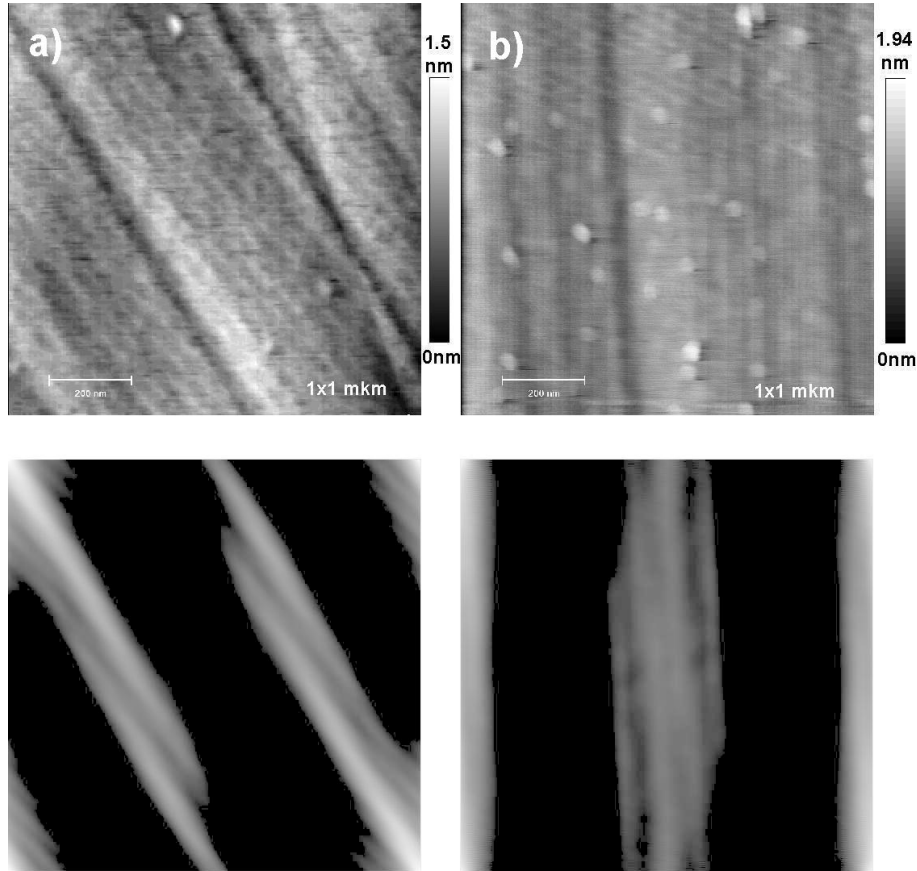


Figure 4.6: AFM surface scans of 2 regions of WGM localization and images of corresponding 2-dimensional autocorrelation functions. Squares are 1 x 1 micrometer.

for the unbiased variance. These values are significantly smaller than those typical of fused silica resonators [32], and demonstrate the capability of our fabrication technique. It is possible to achieve even better results if advanced polishing techniques are used. In order to use the analysis, the correlation length B should also be computed. We are interested in the correlation length along the direction of light propagation, which in our case is coincident with the direction of polishing traces. Computer algorithms of the image rotation generally alter the correlation function. In addition, the autocorrelation function depends on the direction of computation for our type of surface. In order to overcome these problems, a two-dimensional correlation function may be computed with the use of a Wiener-Khinchin theorem and fast Fourier transform algorithms. Computed autocorrelations are shown in Fig. 4.6 below the surface scans and are represented as levels in white. The black color corresponds to zero. Since polishing leaves some traces, as can be seen on Fig. 4.6, the two-dimensional autocorrelation functions decay slowly in the direction of polishing, masking short-range surface structures in this direction. We may use the correlation length measured in the direction orthogonal to polishing traces to obtain the characteristic radius of the surface features. Such an approach is justified as the shape of the scatterer is irrelevant [62]. For both images this gives

$B \simeq 40 \text{ nm}$. These computed parameters give $Q_a = 4.3 \times 10^{11}$ and $Q_b = 6.6 \times 10^{11}$ for surface-limited Q factors.

A number of inclusions with diameters of 30–50 nm protrude from the surface by only about 1–2 nm, and can be seen in Fig. 4.6. These inclusions could possibly be the “shadows” of the diamond nanoparticles, used in the polishing process, that were buried in the surface layer. The assumption that there are particles inside the surface is reasonable as it is known that a thin 0.1 μm surface layer may flow when the surface is being polished, thus trapping the polishing particles [63]. Particle scattering limited Q when K 50 nm diamond spheres are embedded into the surface is given by

$$Q_{sp} = \frac{2\pi n V_{lm1}}{K \lambda \sigma_{sp}}, \quad \alpha_{sp} = \frac{K \sigma_{sp}}{V_{lm1}}. \quad (4.4)$$

Here σ_{sp} is a classical cross section of a spherical scatterer [64]:

$$\sigma_{sp} = \frac{8\pi}{3} k^4 r^6 \left(\frac{\epsilon_s - \epsilon_c}{\epsilon_s + 2\epsilon_c} \right)^2, \quad (4.5)$$

α_{sp} is a corresponding loss decrement and V_{lm1} is a WGM volume, which may be estimated as (see Sec. 1.2.2)

$$V_{lm1} \simeq 3.4\pi^{3/2} \left(\frac{\lambda}{2\pi n} \right)^3 l^{11/6} \sqrt{2(l-m)+1}. \quad (4.6)$$

Here l and m are the mode indices, $l \simeq 2\pi a n / \lambda$. This gives $Q = 7 \times 10^{12} / K$ which means that even with 100 such embedded particles, a scattering limited Q of 7×10^{10} can be achieved. Unfortunately, available images cover only a minor portion of the surface area, so it is difficult to determine the actual concentration of nanoparticles on the surface of our resonators.

Another possible explanation for the observed particle-like structures in Fig. 4.6 might be the chemical reactions between the CaF_2 surface layer and the constituents of air. Air-induced roughness of cleaved CaF_2 surface was found to be characterized by randomly distributed nanometer-sized features. These features are believed to be induced by oxygen, and remain stable after formation [65].

4.1.5.2 Material absorption and scattering

An ideal crystal with no impurities and defects has its window of transparency defined by the tail of multiphonon absorption on the long wavelength side and by the tail of absorption caused by electronic transitions on the short wavelength side, also known as the Urbach tail. Raman, Rayleigh, and Brillouin scattering mechanisms are also present in ideal crystals. It was experimentally found, and theoretically verified, that the behavior of multiphonon and Urbach tails can be quite generally described by an exponential law. As will be discussed later, of all scattering processes, only Raman scattering plays a significant role in crystalline cavities. Thus, bulk losses in CaF_2 may be

approximated by the following phenomenological expression [63, 66]:

$$\alpha_{mat} = \alpha_{uv}e^{\lambda_{uv}/\lambda} + \alpha_{rm} \left(\frac{\lambda_r}{\lambda} \right)^{-4} + \alpha_{ir}e^{-\lambda_{ir}/\lambda}. \quad (4.7)$$

Here α_{uv} , α_{ir} , λ_{uv} , and λ_{ir} are the constants obtained by fitting the experimental data for UV and IR absorption coefficients. Coefficient α_{rm} accounts for scattering suppression in the case of whispering gallery modes $\alpha_{rm} = K_{(TE,TM)}^{-1}\alpha_r$, where α_r is mostly Rayleigh scattering losses measured at λ_r .

Experimental data on the UV absorption for determining the parameters of the Urbach tail in CaF_2 are rather scarce. Another complication is the dependence of the parameters on temperature. Impurities may have a strong effect on the UV absorption spectra of CaF_2 [67]. The UV absorption coefficient is also known to be fluence dependent [68]. From Fig. 4.7 it can be seen that as

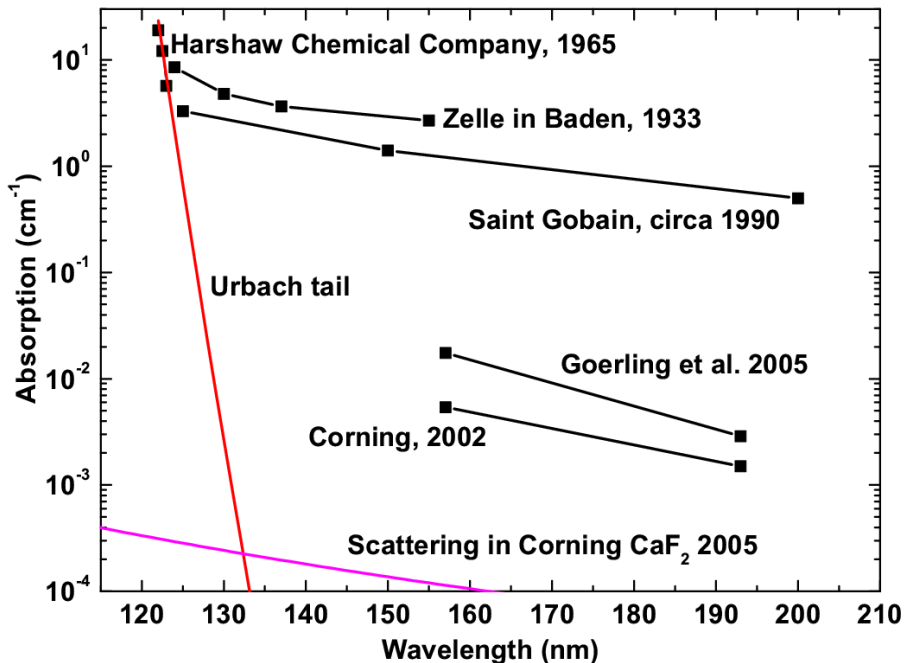


Figure 4.7: Absorption in CaF_2 and Urbach tail. Data from 1965 [69] corresponding to the three shortest wavelength points were also used to estimate the Urbach tail parameters. The 1933 data is from [70]. Saint Gobain and Corning data were obtained from the websites of these manufacturers. The scattering data was derived from [71]. Measurements by Ch. Goerling [68] are the first to separate the coefficients of bulk and surface absorption. Lines connect the data from the same source.

technology has advanced, CaF_2 blanks of higher purity have appeared. We assume that absorption for wavelengths longer than the UV cut-off is determined by impurities. The absorption coefficient for the cut-off wavelengths follows an exponential law. We have found that the data by Laufer et al. [69] may be used to estimate the parameters of the Urbach tail as they represent measurements in the UV-cut off region. Parameters of the multiphonon absorption wing were estimated from IR absorption data for Corning CaF_2 .

In a thorough study it was found [71] that in the best samples of CaF_2 Raman scattering accounts for less than 10% of the total scattering and thus can be neglected. Stimulated Raman scattering, however, can not be neglected in our cavities as will be shown below. Elastic component of Rayleigh scattering in CaF_2 was found to be equal to the bulk Brillouin scattering in a crystal. In a WGM cavity the acoustic phonon spectrum is modified and Brillouin scattering is further inhibited. As will be shown in Sec. 5.2, however, stimulated Brillouin scattering can be observed under special conditions in WGM resonators. In comparison to high-purity fused silica (HPFS), for the best CaF_2 specimens the intrinsic Rayleigh scattering loss is 0.0035, Brillouin loss is 0.005, and extrinsic, defect induced Rayleigh is 0.0015. The total scattering measured in CaF_2 samples at 90 degree is $\alpha(90^\circ) = 6 \times 10^{-4} \text{ Np/m}$ at 193 nm. This gives a total integrated loss coefficient of $\alpha_r = 8\pi\alpha(90^\circ)/3 = 5 \times 10^{-3} \text{ Np/m}$.

4.1.6 Maximum Q factor and its limitations

With the parameters from the two previous sections we have determined the maximum bulk-loss-limited Q factor of a CaF_2 WGMR (Fig. 4.8). Experimental dependence of the refractive index on the wavelength was taken into account. Curve “a” shows what Q factor is possible for an ideal-surface resonator. Electronic absorption is responsible for a sharp decline of the transparency and Q factor for $\lambda < 200 \text{ nm}$. In the visible and near the IR region, the Q factor is mostly determined by Rayleigh scattering. The decline of Q beyond $3 \mu\text{m}$ is explained by multiphonon absorption processes. Curve “b” shows that surface scattering would be the main limitation on the Q factor of our cavities if there were no impurities.

The TM modes are closer to the surface, so more scattered light goes back into the modes as compared to the TE modes, giving the higher Q. For the real cavity the TM modes suffer from additional surface scattering and the difference in Q factors is not so pronounced anymore.

4.1.7 Nonlinear processes in crystalline WGM resonators and optical Q factor

When measuring the optical Q factor, it is important to ensure that nonlinear processes are not present. One way to make sure this is the case is to directly observe the resonant response of a cavity, which for a linear oscillator is known to be described by a Lorentzian lineshape. Deviations from the ideal linear oscillator behavior could serve as a qualitative measure of nonlinearity. In our experiments we found that when the optical power approaches the bistability or the stimulated Raman scattering threshold, the resonator’s response is no longer Lorentzian. The Raman lasing threshold is inversely proportional to the square of the Q factor [72], so when ultrahigh Q factors are expected, reducing the optical power used for measurements to low-enough levels is a challenge.

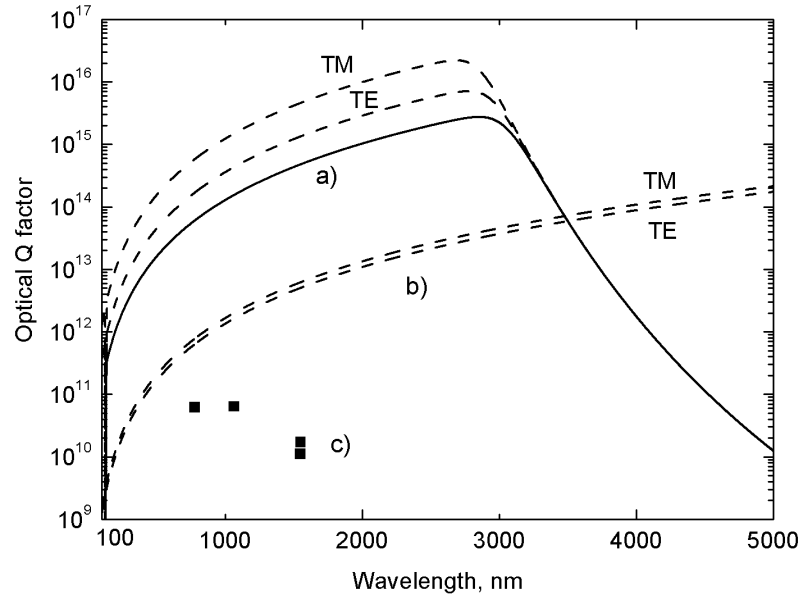


Figure 4.8: Maximum intrinsic Q factor of CaF_2 resonator at room temperature. a) Q factor limited by Rayleigh scattering, multiphonon absorption and electronic absorption in an ideal crystal, along with values modified by the geometry of a WGMR for TE and TM modes; b) surface roughness limited Q factors; and c) experimental data.

Thermo-optical oscillatory instability and thermal nonlinearity [52, 73] were also observed in the nonlinear regime. Linear resonant curves were only observed in a 5.5 mm cavity at coupled pump power levels of less than 100 nW.

As an example, we measured the cavity response at a pump power of $3 \mu\text{W}$. This power was found to be slightly higher than the Raman lasing threshold in our 5.5 mm cavity and is more than an order of magnitude lower than the smallest reported threshold value so far (for an integrated fused silica device [72]). The cavity response at this pump power is strongly non-Lorentzian, with thermo-optical oscillations also present. Interestingly, the onset of the thermo-optical instability was found to be approximately coincident with the Raman lasing thresholds in large (5 mm) and small (0.1 mm) cavities. Further investigations might show that Raman lasing may be involved in the generation of the oscillations in thermo-optical instability.

Kerr and thermal nonlinearities may explain the departure of the cavity response from the Lorentzian shape, as seen in Fig. 4.5 and 4.4. We may derive the bistability threshold, or the power needed to shift the eigenfrequency of a WGM by its width at half maximum $\Delta f = c/(\lambda Q)$, using a

semiclassical approach. Nonlinear index of refraction Δn is given by [74]

$$n = n_0 + n_2 \langle E^2 \rangle = n_0 + \frac{n_2 E_0^2}{2} = n_0 + \Delta n. \quad (4.8)$$

The shift of the cavity's eigenfrequency f is related to a change in the refractive index:

$$\Delta f = -\frac{\Delta n}{n_0} f. \quad (4.9)$$

It follows, that the change in refractive index that would shift the cavity resonance by its width is

$$\Delta n = \frac{cn_0}{f\lambda Q}. \quad (4.10)$$

For the energy density created by the K photons stored in a cavity we have

$$\frac{E_0^2 \varepsilon_0 n_0^2}{2} = \frac{K \hbar \omega}{V_{eff}}, \quad (4.11)$$

hence the nonlinear refractive index is

$$\Delta n = \frac{n_2 E_0^2}{2} = \frac{n_2 K \hbar \omega}{V_{eff} \varepsilon_0 n_0^2}. \quad (4.12)$$

Combining the expression for the nonlinear part of the refractive index and the required Δn we obtain K , the number of photons in the cavity sufficient for bistability:

$$K = \frac{V_{eff} \varepsilon_0 n_0^3}{Q n_2 \hbar \omega}. \quad (4.13)$$

The intensity buildup factor,

$$\frac{I}{I_0} = \frac{Q\lambda}{\pi^2 a n_0} = \alpha \quad (4.14)$$

implies that if we send K/α photons per second to the cavity, the resulting intensity inside the cavity will be equivalent to K photons per second passing each cross section of the WGM. Since each photon completes $\nu_{photon} = c/(2\pi a n_0)$ round trips around the cavity each second, one needs to send

$$\frac{K \nu_{photon}}{\alpha} = \frac{K \omega}{4Q} = \frac{K}{4\tau} \quad (4.15)$$

photons per second as an external excitation to have K photons present in the cavity. This flux of photons gives us the bistability threshold power:

$$W_{bist} = \hbar \omega \frac{\omega}{4Q} \frac{V_{eff} \varepsilon_0 n_0^3}{Q n_2 \hbar \omega} = \frac{\omega V_{eff} \varepsilon_0 n_0^3}{4Q^2 n_2}. \quad (4.16)$$

If one uses the relation for third-order susceptibility given in [74], which is valid for a linearly polarized laser beam in isotropic materials and for the beam linearly polarized along [100] axis of a cubic crystal,

$$n_2 = \frac{12\pi\chi_{1111}^{(3)}}{n_0}, \quad (4.17)$$

and a relation between the systems of units [75]

$$(n_2)_{MKS} = \frac{1}{9} \times 10^{-8} (n_2)_{esu}, \quad (4.18)$$

the CGS units formula for bistability threshold is

$$W_{bist} = \frac{V_{eff}\omega n_0^4}{192\pi\chi^{(3)}Q^2}. \quad (4.19)$$

In comparison with equation (3) in [19], this formula is different by a factor of 1/6, but it correctly gives the values of bistability threshold cited in that paper.

The value of the nonlinear refractive index of CaF_2 is $n_2 = 4.78 \times 10^{-23} \text{ m}^2/\text{V}^2$ [76, 74]. Thus the bistability threshold for 1.5 mm cavity ($V_{ll1} = 2.93 \times 10^{-13} \text{ m}^3$, $Q = 4 \times 10^{10}$) is $W_{bist} = 44 \text{ nW}$. For a 5 mm cavity with $Q = 6 \times 10^{10}$ the threshold is about $0.2 \mu\text{W}$. This shows that a very low input power could shift the eigen-frequency of a crystalline cavity. The fact that the resonant curves presented on Fig. 4.5 for a pump power of 60 nW are Lorentzian even though the power is 1/3 of the bistability threshold implies that the excited mode was probably not a fundamental WGM, but rather a mode with a large effective volume, $l - m > 1$. For such a mode the bistability threshold is larger than 200 nW and scales with the modal volume, proportional to $\sqrt{2(l - m) + 1}$ (see Sec. 1.2.2).

The third-order susceptibility associated with the thermal nonlinearity and a specific response time depending on mode configuration may be estimated for TE_{lm1}, TM_{lm1} modes as follows (formula in CGS units from [19]):

$$\chi_T^{(3)} \simeq \frac{n_0 \alpha c \tau_T}{80\pi^2 N k T}, \tau_T = \frac{\lambda^2 l^{2/3} \rho c_p}{\beta n_0^2 \pi^2}. \quad (4.20)$$

Here α is a bulk attenuation coefficient, k -Boltzmann constant, β -thermal conductivity, and c_p -heat capacity. We have observed that the difference in Q factors for TE and TM modes was much smaller than what might be expected if the Q were limited by scattering. In this case Q factors would have been proportional to the scattering suppression coefficients $Q_{TE}/Q_{TM} \sim K_{TE}/K_{TM}$. The demonstrated Q factor of $(6.27 \pm 0.78) \times 10^{10}$ gives a new upper limit on the absorption coefficient in CaF_2 at 1064 nm of $\alpha \simeq 1.4 \times 10^{-4} \text{ Np/m}$, derived from equation (4.1). Thus, the given value of α reflects losses in the bulk crystal and the optical Q factor in our cavities is limited by the internal absorption. Using parameters for CaF_2 : $\beta = 12 \text{ W}/(\text{mK})$, $\rho = 3180 \text{ kg}\cdot\text{m}^{-3}$, $c_p = 853 \text{ J}/(\text{kg}\cdot\text{K})$.

K), $a=2500\ \mu\text{m}$ and $\lambda = 1.064\ \mu\text{m}$ we estimate room temperature values $\tau_T \simeq 10\ \mu\text{s}$ and $\chi_T^{(3)} \simeq 7.3 \times 10^{-12}\ \text{cm}^3/\text{erg} = 8.1 \times 10^{-21}\ \text{m}^2/\text{V}^2$. The concentration of CaF_2 was computed as $N = 2.45 \times 10^{28}\ \text{m}^{-3}$. We see that the thermal nonlinearity is dominating in our cavity, which agrees with the experimental observation.

4.1.8 Impurities and possibilities for higher Q factors

Measurements of the Q factor at 1550 nm yielded $Q = 1.1 \times 10^{10}$, which is smaller than the previously reported value of $Q = 1.7 \times 10^{10}$ in [30]. This may be explained by the difference in specific fluorite blanks and by the fact that the resonance curve in that work is nonlinear. While theoretical estimates show that the Q factor should increase with the wavelength in the region of experimental measurements (780–1550 nm), we found the opposite to take place, indicating an increase of bulk losses for longer wavelengths (Fig. 4.8). The development of pure fluorite blanks is mostly driven by the industrial demand for high quality crystals suitable for lithographic lenses transparent in the UV region. Thus one may expect such fluorite blanks to have a reduced amount of impurities absorbing at shorter wavelengths, explaining the lower Q at longer wavelength. For the best fluorite blank from Corning, the total absorption is about an order of magnitude larger than the bulk light scattering [71]. Taking into account the argument from the previous section regarding surface scattering, it follows that the absorption and scattering by impurities is the main loss mechanism in our crystalline WGM cavities.

The crystals used for fabrication of WGM in this work are the purest available excimer-grade CaF_2 blanks. Nevertheless, these crystals contain significant amounts of atomic impurities such as rare earths and other elements. For a typical excimer-grade CaF_2 there may be more than 20 impurities with more than 10 ppb concentration, and the total amount of impurities exceeds 10 ppm, a significant fraction of which is represented by strontium, magnesium, iron, and zinc in the case of our crystals. Strontium was found to improve the radiation resistance of CaF_2 [77]. Ultrahigh Q factors are only achievable at low circulating optical power, where even a minor amount of impurity ions can influence the response of the crystalline medium through resonant Mie-type atomic fluorescence. Unfortunately, the information on the absorption spectra of certain ions in CaF_2 is not always available. The optical properties of impurities are characterized by sharp lines, which correspond to optical transitions. The width of these lines increases with temperature. Thus, one possibility of avoiding the influence of impurities in WGM cavities is to operate them at lower temperatures outside of the spectral regions corresponding to optical transitions of the impurities. According to the analysis presented in Fig. 4.8, one may expect the Q factor to approach the surface scattering limit of $Q = 10^{12}$ at $\lambda = 1\ \mu\text{m}$ if the impurities are “frozen out”. If a better surface is fabricated, the material-limited Q factor for the available fluorite crystals should approach $Q = 10^{14}$ at $\lambda = 1\ \mu\text{m}$ and $Q = 10^{15}$ at $\lambda = 3\ \mu\text{m}$ if the impurities are not taken into account. The latter would

give an average photon confinement time in excess of one second. There are other ways of improving optical quality of crystals. Annealing may be used to modify absorption spectra of color centers and reduce concentration of dislocations and other defects. This technique has recently been used on CaF_2 and the evidence of significant improvements in Q factor were recorded [78]. Thermoelectric oxidization has also been found useful for improvement of optical damage characteristics of lithium niobate crystals [79].

4.1.9 Possible applications and conclusion

As the intrinsic optical Q factor of a WGM cavity increases, the power buildup coefficient grows, which in turn lowers the threshold for nonlinear processes. We have shown that by reducing the optical power circulating in an ultrahigh Q crystalline cavity it is possible to achieve a linear mode and reliably measure the ultrahigh optical Q factors. We have demonstrated values as high as $(6.27 \pm 0.78) \times 10^{10}$, which gives a new upper limit on the absorption coefficient in untreated CaF_2 at 1064 nm of $\alpha \simeq 1.4 \times 10^{-4} \text{ Np/m}$. The measured Q factors are the highest values reported for any optical resonator with these dimensions, making crystalline cavities extremely attractive tools in optics. Possible applications of crystalline cavities include compact integrated Raman lasers, cavity QED experiments with crystalline microresonators, and quantum nondemolition measurements.

As the threshold of Raman lasing is inversely proportional to the square of the Q factor, crystalline cavities represent new possibilities for the realization of tunable, fiber-compatible Raman lasers operating with high efficiency. Another interesting application of high Q crystalline cavities is based on optical parametric oscillations [61]. It might be possible to fabricate an all-optical, fiber-coupled, solid-state frequency standard and a single ion clock based on these devices.

Estimates for a 100 μm LiNbO_3 cavity show that a single photon would shift the cavity resonance by as much as 6 Hz. Such a shift can be detected with optical techniques. This opens new possibilities for quantum nondemolition (QND) measurements of the number of photons in a cavity. However, thermal effects may cause much larger random shifts at room temperature [24].

As was discussed in Sec. 4.1.5.1, a number of polishing particles remain attached to the surface of the cavity and if the particles are small enough, the high Q factor is preserved. Observation of these particles suggests the possibility for imprinting quantum-dot-containing diamond or other nanoparticles into the surface while preserving the Q factor on a very high level, even for the small WGM cavities suitable for cavity QED experiments. In similar experiments with silica microspheres, the application of nanoparticles through deposition usually leads to a significant degradation of the Q factor of the cavity.

The extreme Q factors of crystalline cavities open new opportunities in optical filtering and spectroscopy. A single-mode cavity made with lithium niobate could operate as a tunable, fiber-coupled etalon, more compact and with a higher finesse than a Fabry-Perot cavity. For these

applications, resonators with large mode volumes must be selected to reduce the undesirable effects of nonlinearities.

In conclusion, we have demonstrated measurements of a record-high optical Q factor of a fluorite WGMR, fabricated with a diamond-grinding technique. We analyzed possible loss mechanisms in crystals and the influence of nonlinear processes. We showed that in order to measure the higher Q factors in linear regime, lower pump power levels must be used to avoid nonlinear processes.

4.2 Fundamental limits and cryogenic Q factor of crystalline resonators

This section is based on a paper published in *Optics Express* [4] called “On the fundamental limits of Q factor of crystalline dielectric resonators”.

The temperature dependence of the processes which fundamentally limit optical quality factor of ideal crystalline whispering-gallery-mode resonators is investigated. The example of CaF_2 is used to show that spontaneous Raman scattering is the main limitation of the quality factor at low temperatures. Stimulated Raman scattering is also shown to be important at any temperature. We experimentally demonstrate nonlinear absorption due to stimulated Raman scattering in a real cavity at room temperature and theoretically derive Raman gain of CaF_2 . We conclude that optical storage times in excess of one second could be achieved in millimeter-sized cavities.

Recent progress in fabrication of whispering-gallery-mode (WGM) resonators with crystalline materials has resulted in the highest demonstrated quality factors (Q) for these types of cavities [30, 78], (Sec. 4.1). The mechanical polishing techniques used in the fabrication process essentially eliminate surface scattering and surface absorption as loss mechanisms at the achieved material transparency levels (see Sec. 3.3). The only remaining physical mechanisms limiting the ultimate achievable Q with this approach are linear and nonlinear attenuation in the dielectric material.

Optical transparency of ideal dielectric crystals is restricted by the fundamental blue and red wings of photon absorption. The blue wing is defined by optically allowed transitions between valence and conduction electron bands. The red wing results from the interaction between light and phonons in the crystalline medium. Both absorption mechanisms have a strong frequency dependence, so the absorption of light in a dielectric within the transparency band can be extremely low. The question is how low it can be, and is there any other transparency-limiting mechanism. A similar question has been discussed for optical fibers [62]. It was shown that the scattering loss mechanisms — such as Rayleigh, Brillouin and Raman — determine the extent of optical attenuation. These mechanisms are present in ideal optical crystals and limit their transparency as well.

In this section we analyze the minimum light attenuation achievable with ideal crystals at room and cryogenic temperatures. We use a real, almost-perfect fluorite crystal as an example. It was

shown previously that the attenuation of UV light in artificially grown CaF_2 is nearly completely limited by Brillouin and thermodynamic Rayleigh scattering [71] at room temperature. We show that the spontaneous Raman scattering is primarily responsible for the attenuation in an ideal crystal at low temperatures. Applying this result to the crystalline WGM resonators, we find the limits to the IR quality factors. We also show that, in contrast to the low-temperature regime, spontaneous Brillouin scattering, as well as stimulated Raman scattering (SRS), determine the Q factor of a WGM resonator under realistic experimental conditions at room temperature. We measure the influence of SRS on the Q factor of a millimeter-sized resonator using a ring-down technique, and show that this scattering becomes important at input power levels higher than a few microwatts.

4.2.1 Three types of scattering

Let us consider Rayleigh, Brillouin, and Raman scattering in a perfect crystal. Thermodynamically limited Rayleigh scattering is small in an ideal crystal, and Brillouin scattering dominates. The quantitative ratio of Rayleigh and Brillouin scattering can be estimated using the Landau-Plachek relationship (see, e.g., [80]):

$$\frac{\alpha_{Ri}}{\alpha_B} \simeq \frac{\beta_T}{\beta_S} - 1 \quad (4.21)$$

where β_T and β_S are the isothermal and isobaric compressibilities, respectively. This ratio is generally less than unity in crystals and vanishes with temperature decrease in the low-temperature limit ([81], p. 219):

$$\frac{\beta_T}{\beta_S} - 1 = \frac{C_P}{C_V} - 1 \sim T^4|_{T \rightarrow 0}, \quad (4.22)$$

where C_P and C_V are the specific heat capacities at constant pressure and constant volume, respectively. Rayleigh scattering can be neglected in a perfect crystal at low temperature, as the result of (4.22).

Temperature dependence of spontaneous Raman and Brillouin scattering mechanisms is determined by the number of participating phonons, given by a Bose population factor [82]. The corresponding light attenuation coefficient accounting for both Stokes and anti-Stokes components may be estimated as follows (see also [80], p. 99)

$$\alpha_{B,R} \approx \alpha_{B0,R0} \left(\frac{\lambda_0}{\lambda} \right)^4 \left[\left(\exp \frac{\hbar\Omega_{B,R}}{k_B T} - 1 \right)^{-1} + \frac{1}{2} \right] \quad (4.23)$$

where λ is the wavelength of light, $\alpha_{B0,R0}$ are the scattering parameters given by the properties of a particular crystal corresponding to λ_0 , Ω_B is the Brillouin frequency shift for 90° scattering, and Ω_R is the Raman frequency shift.

In writing of (4.23) we have assumed that the crystal has a single phonon branch. Using data evaluated for CaF_2 at $T=300$ K in [71]: $\hbar\Omega_B/k_B T \simeq 1/300$, $\hbar\Omega_R/k_B T \simeq 1/4$, $\lambda_0 = 0.532 \mu\text{m}$, $\alpha_B =$

$2.411 \times 10^{-7} \text{ cm}^{-1}$, $\alpha_R \simeq 4.34 \times 10^{-8} \text{ cm}^{-1}$ we obtain $\alpha_{B0} \simeq 8 \times 10^{-10} \text{ cm}^{-1}$, $\alpha_{R0} \simeq 1.1 \times 10^{-8} \text{ cm}^{-1}$. It is easy to see that Brillouin scattering is significantly suppressed and the attenuation of light in a perfect crystal is determined by the spontaneous Raman scattering at low temperature. The room temperature attenuation, on the other hand, is given by spontaneous Brillouin scattering.

It is shown in [71] that the existing calcium fluoride crystals have transparency close to the fundamental limit (4.23) in the UV. However, such a low attenuation is yet to be demonstrated in experiments with visible and infrared light. The measured transparency is two to three orders of magnitude lower than the fundamental limit in those frequency bands (see [30], Sec. 4.1 and Sec. 3.3) because of the extrinsic and intrinsic impurities of the material.

4.2.2 Properties of fluorite WGM resonators

We now discuss the optical properties of fluorite WGM resonators. The maximum quality factor of the resonator is given by $Q_{max} = 2\pi n(\lambda)/[\lambda\alpha(\lambda)]$, where $n(\lambda)$ is the refractive index of the material, λ is the wavelength of light in vacuum, and $\alpha(\lambda)$ is the total loss coefficient of the bulk dielectric material. This formula is not entirely correct for scattering losses. A coherent scattering loss, where some part of scattered light is deflected back into the mode, leads to the enhancement of the Q factor by up to an order of magnitude [54]. We still use the formula as the role of scattering is minor in the case of an ideal fluorite cavity, which we consider in this study. In such a cavity the surface roughness is given by the lattice constant and the corresponding optical storage time can reach 1 s for a resonator having 1 cm in diameter for $\lambda = 1 \mu\text{m}$.

In case of a real cavity, the surface roughness can limit Q factor. Some estimates made in Sec. 4.1 for a particular fluorite cavity show an upper limit for Q of about 10^{12} . However, this is a technical limitation given by the particular polishing procedure. A further investigation is required before storage time beyond 1 s is achieved.

In what follows we neglect the surface scattering and consider only unavoidable attenuation mechanisms. The corresponding wavelength dependence of the attenuation as well as Q factor for CaF_2 , given by Raman and Brillouin scattering as well as by blue and red wing absorption, are shown in Fig. 4.9. The approximation of the maximum quality factor of CaF_2 WGM resonators found in [30] using existing experimental results nearly coincides with the fundamental limit presented in this paper at room temperature. The wavelength dependence of the index of refraction of the material at $T = 300 \text{ K}$ was found using the 4-term Sellmeier equation [83]. Blue and red absorption wings can generally be approximated by a simple exponential dependence [63, 66]. Parameters for the blue wing have been derived from [69]. Red wing parameters were obtained from [84] and the experimental data publicly available for Corning CaF_2 . For our analysis we have assumed both wings to be temperature independent, as the temperature dependence is known to be weak. According to Fig. 4.9, the lifetime of a photon in a fluorite WGM resonator can exceed 1 s for $\lambda = 1.5 \mu\text{m}$.

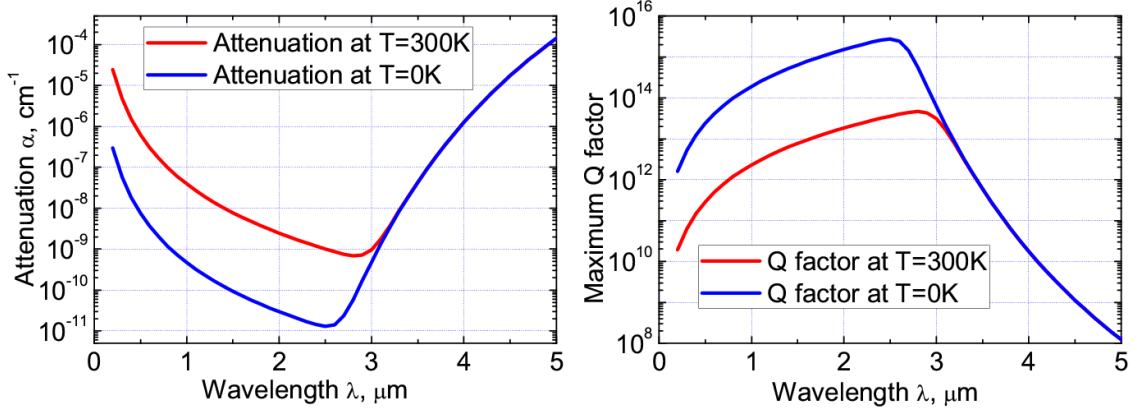


Figure 4.9: Attenuation in ideal CaF_2 (left), and Q factor (right) of ideal fluorite WGM resonators at room and nearly absolute-zero temperature. Contributions from spontaneous Brillouin, Rayleigh, and Raman scattering, as well as blue and red wing absorption, are added.

We now show that not only spontaneous, but also stimulated scattering is important in macroscopic WGM resonators. Stimulated Rayleigh scattering is not experimentally observable in high-Q WGM resonators as it is suppressed by a mismatch of modal structure of a typical cavity and the gain profile for this process [80]. Stimulated Brillouin scattering is suppressed because of the absence of phase matching between acoustical and optical modes in the WGM resonators (however, see Sec. 5.2). The resonantly enhanced, stimulated Raman scattering is always possible if the frequency difference between subsequent modes of the same mode family (free spectral range, FSR) is less than the spectral width Γ of the optical phonons. In fluorite at room temperature $\Gamma = 450 \text{ GHz}$ [85]. Hence any resonator with radius $R \geq c/(2\pi n(\lambda)\Gamma) \simeq 75 \mu\text{m}$ is not immune to SRS.

Stimulated Raman scattering, as well as spontaneous Raman scattering, is present in even an ideal crystalline lattice at nearly absolute-zero temperature. It is one of the fundamental causes of light absorption in a WGM resonator. The stimulated scattering generates optical phonons in the material. The phonons decay due to the multiphonon scattering, which results in heating of the crystal and growing of the entropy. To estimate the maximum quality factor achievable in a crystalline WGM resonator if SRS is allowed, we consider a resonator supporting a pump and several first-order Stokes modes. Such a system can be described at low temperature by a set of rate equations [86]:

$$\dot{n}_S = -2\gamma_S n_S + \hbar\omega_p \frac{c^2}{n^2} \frac{g_b}{V} n_p n_S, \quad (4.24)$$

$$\dot{n}_p = -2\gamma_p n_p - \hbar\omega_p \frac{c^2}{n^2} \frac{g_b}{V} \sum_S n_p n_S, \quad (4.25)$$

where n is the refractive index, $n_p \gg 1$ and $n_S \gg 1$ are the averaged photon numbers in the pump and Stokes modes, V is the mode volume, and $2\gamma_S = \alpha(\lambda_S)c/n$ and $2\gamma_p = \alpha(\lambda_p)c/n$ are the total

linear decay rates of Stokes and pump modes respectively. The rates take spontaneous scattering decay into account. We assume that the modes completely overlap and have the same volume V . These equations were derived from (25) and (26) of [87] by replacing spatial derivatives ($dP_{p,S}/dz$, $P_{p,S}$ is the power of pump and Stokes light) with temporal derivatives ($\dot{n}_{p,S}$).

The bulk Raman gain g_b is related to the attenuation due to spontaneous Raman scattering as ([86], p. 371)

$$g_b(\lambda_p) = \frac{\alpha_R(\lambda_p)\lambda_p^4 \omega_p}{8\pi^2 c^2 n^2 \hbar \Gamma}, \quad (4.26)$$

where we assume that $\lambda_S = \lambda_p$. The wavelength dependence of the gain is shown in Fig. 4.10(c). It is easy to see that for CaF₂ the value of the bulk Raman gain is $g_b = 2.4 \times 10^{-11}$ cm/W at $\lambda = 1 \mu\text{m}$.

An approximate temperature dependence of the spectral width of the Raman phonons is given by [88]

$$\Gamma = \Gamma_0 \left[1 + \frac{2}{\exp(\hbar\Omega_R/2kT) - 1} \right], \quad (4.27)$$

if we assume that phonons experience degenerate two-particle anharmonic decay.

According to equation (4.25) the effective decay rate of the pump radiation due to SRS is

$$2\gamma_{SRS} = \hbar\omega_p \frac{c^2}{n^2} \frac{g_b}{V} N_S n_S, \quad (4.28)$$

where N_S is the total number of Stokes modes the light decays into, and n_S depends on the pump power. The quality factor of the pump mode, Q_{SRS} , is going to be smaller than Q when the pump power exceeds P_{th} [89]:

$$\frac{Q}{Q_{SRS}} = \sqrt{\frac{P}{P_{th}}}, \quad (4.29)$$

where SRS threshold power is given by

$$P_{th} = \frac{\pi^2 n^2}{g_b Q_p Q_S} \frac{V}{\lambda_p \lambda_S}, \quad (4.30)$$

and the external pumping P is assumed to exceed the threshold significantly $P \gg P_{th}$. Selecting the realistic values for a 1 mm cavity $g_b = 2.4 \times 10^{-11}$ cm/W, $n = 1.43$, $V = 1.4 \times 10^{-7}$ cm³, $Q_p = Q_S = 10^{10}$, $\lambda_p = \lambda_S = 1 \mu\text{m}$, we obtain $P_{th} \simeq 120$ nW. Pumping the resonator with $1 \mu\text{W}$ of light for these parameters will result in a reduction of the effective quality factor of the corresponding WGM down to $Q_{SRS} = 3.5 \times 10^9$. It should be emphasized that this quality factor is related to the pump light only. To observe this Q factor decrease, the Stokes light should be blocked from reaching the photodetector when using a ringdown technique. We may combine equation (4.30) with equations (4.27) and (4.26) to derive temperature dependence of SRS threshold power for this cavity. It is also interesting to estimate the threshold power in terms of a photon number given by the expression $P_{th} T_R / \hbar\omega$, where $T_R = Q/\omega$ is the ringdown time. The results are presented in

Fig. 4.10.

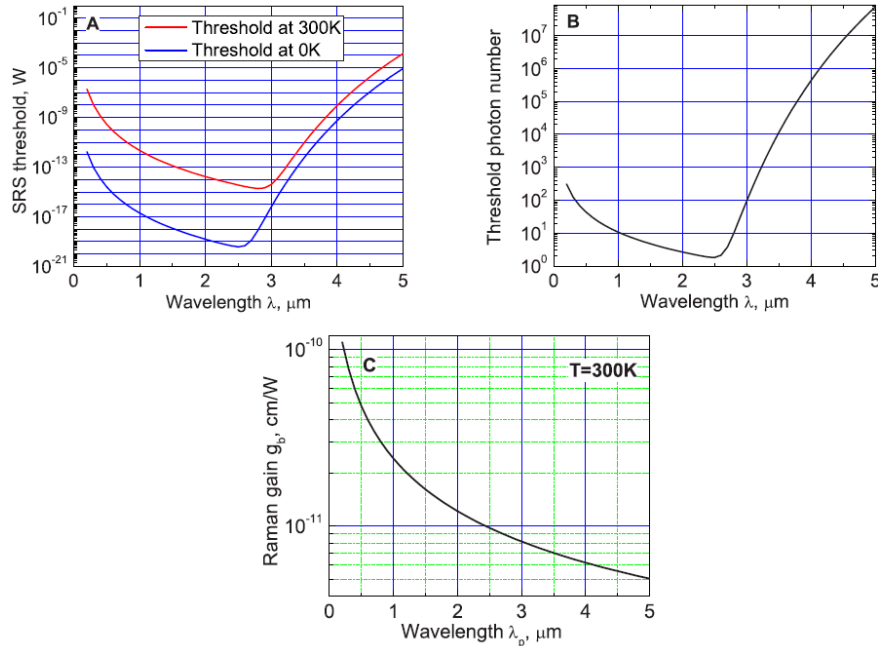


Figure 4.10: A) SRS threshold for a 1 mm ideal-surface cavity made with an ideal CaF_2 . B) Low temperature SRS threshold for a 1 mm ideal cavity made with CaF_2 in terms of photon number. C) Theoretically evaluated wavelength dependence of the Raman gain in CaF_2 .

4.2.3 Experimental observation of nonlinear attenuation

We have performed an experiment to demonstrate the nonlinear attenuation caused by SRS. Measurements at 780 nm were performed with an external cavity stabilized diode laser. Free beam emission from the laser was coupled to a fiber, which had an output collimator attached. Light from the collimator lens was sent into a glass prism, which served as a coupler for a CaF_2 WGM resonator. Coupling efficiency of the pump light to WGMs was better than 30%. The output light that went through the coupler was collimated with a lens and collected on a photodetector. Although the Stokes light should be blocked to observe the nonlinear behavior, in this experiment we did not employ specific measures to do so. We suppose the Stokes light was partially blocked accidentally by dispersive properties of the setup components.

We observed ringdown signals obtained by periodic scanning of the laser frequency over many resonator modes with the internal piezo of the laser head. Time-dependent signals resulted from the interference between the pump radiation and the emission from the resonator. According to our observations the signal had a clearly non-exponential time dependence (Fig. 4.11), which supports the above discussion.

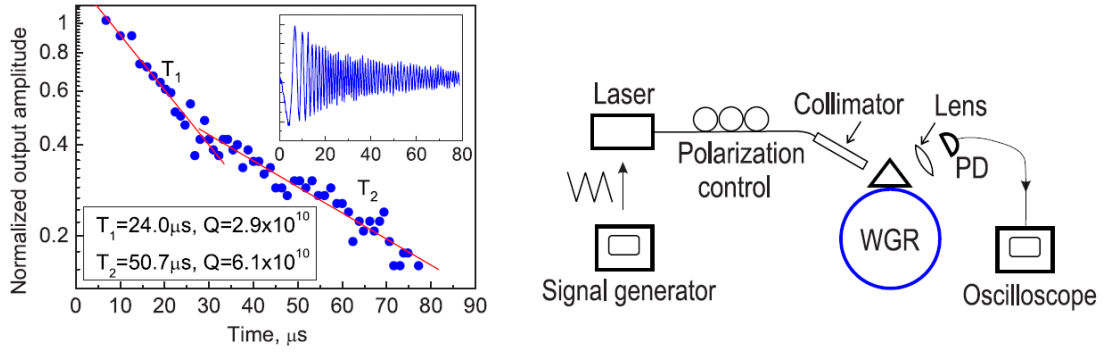


Figure 4.11: Experimental observation of the ringdown signal of a calcium fluoride resonator and setup scheme. The observations were performed at 780 nm. The threshold power of the SRS process was on the order of a few microwatts. Linear fits of the amplitude decay are presented by red lines, emphasizing two different ringdown constants at the beginning and at the end of the process. Inset shows the actual signal recorded on the photodetector. Blue points in the graph represent the amplitude of the signal shown in the inset.

4.2.4 Conclusion

We have presented theoretical as well as experimental studies of light attenuation resulting from fundamental scattering in crystalline WGM resonators. We show that the spontaneous Raman scattering results in the fundamental restrictions of the resonator quality factor at low temperatures. Stimulated Raman scattering also restricts the quality factor at any temperature if the power of the light used in the resonator exceeds the threshold of the stimulated process.

Chapter 5

Photon–phonon interactions in crystalline resonators

There are three major scattering mechanisms in optical fibers. These mechanisms are named after Rayleigh, Raman, and Brillouin. If the intensity of light in fiber is high enough, a stimulated process may occur in which the scattered wave is amplified at the expense of the input beam. All three scattering mechanisms are present in WGM crystalline resonators. Rayleigh scattering is caused by non-propagating, frozen density fluctuations and is theoretically absent in pure crystals at low temperatures. At higher temperatures there may still be Rayleigh scattering due to microscopic temperature fluctuations. Raman scattering is caused by interaction of photons and vibrational states of molecules of which the crystal is made, or optical phonons. Brillouin scattering is an interaction between photons and acoustic phonons, or scattering from density fluctuations caused by acoustic waves. In a stimulated Brillouin scattering, the energy is transferred from the optical beam to the acoustic wave through electrostriction and the frequency of phonons is clamped to a specific value defined by energy and momentum conservation. It depends on optical wavelength, material composition, and, to some extent, temperature and pressure. While spontaneous scattering events limit the optical Q factor of a resonator, stimulated process is useful in that it enables WGM-based Raman and Brillouin lasers, which are expected to have very good characteristics as compared to the counterparts based on the fiber-ring resonators. Advantages include lower threshold and higher conversion efficiency as well as narrow linewidth. Raman and Brillouin lasing in crystalline WGM resonators are demonstrated in this work for the first time.

Results presented in this chapter are based on papers published in *Optics Letters*, *Journal of Optical Society of America B* and *Physical Review Letters* (submitted) [5, 6, 7]. Reproduced with permission from OSA.

5.1 Stimulated Raman scattering.

5.1.1 Introduction

Scattering of light by optical phonons was experimentally discovered by Raman and Krishnan in liquids, and independently by Mandelshtam and Landsberg in crystals [90, 91]. Lasers based on the stimulated Raman scattering (SRS) effect have found numerous applications in material science, molecular spectroscopy, and in many biological studies. SRS can be used to convert one optical frequency into another, making it possible to access virtually any wavelength within the Raman-active material's transparency window. Generation of stimulated Raman scattering requires high levels of optical power, which may be reduced if a Raman-active medium is placed into an optical resonator. In this case, Raman laser characteristics are also defined by the properties of the resonator. Existing configurations include Raman lasers based on variations of Fabry-Perot cavities [92], Bragg grating resonators [93], fiber-ring cavities [94] and WGM resonators [72, 95]. The latter, while being compact and fiber compatible, exhibit the lowest lasing thresholds as extremely high optical power density in the cavity is easy to achieve. For example, in a $100\ \mu\text{m}$ fused silica WGMR with $Q = 5 \times 10^8$, injected power of 1 mW builds up to intensity of $12\ \text{GW}/\text{cm}^2$. The high optical Q factors of WGMRs make it possible to easily achieve high intracavity power to enhance nonlinear effects [96, 33, 27, 31, 94]. Low threshold makes miniaturization of a Raman laser possible. The recently demonstrated [95] integrated Raman laser based on a fused silica microsphere has a lasing threshold on the order of $100\ \mu\text{W}$, owing mostly to high intracavity intensity buildup factor. However, the Q factor of fused silica cavities is subject to degradation due to atmospheric water and is limited to about eight billions for mm-sized resonators by material purity achievable with today's technology. Fluorite cavities have certain advantages over their fused silica counterparts. The lower loss of the crystalline material allows for higher Q factors and the associated intracavity optical power buildup which, along with a higher Raman gain of the fluorite (Sec. 4.2), lead to lower thresholds of Raman lasing. This material may easily be superpolished to subnanometer surface roughness as demonstrated in Sec. 4.1, and the resulting surface does not absorb water vapor. The refractive index of fluorite is smaller than that of fused silica, making it possible to use common optical fibers to couple light in and out of the cavity. A coupling efficiency exceeding 80% is routinely achieved in our lab. Finally, it is possible to use diamond machining techniques to produce fluorite cavities with a predesigned spectral response and single-mode cavities (Sec. 3.1).

We demonstrate efficient and ultralow threshold Raman lasing with ultrahigh Q CaF_2 whispering gallery mode (WGM) resonators. Continuous wave emission threshold is shown possible below $1\ \mu\text{W}$ with a 5 mm cavity, orders of magnitude lower than in any other non-WGMR Raman source. Achieving a low lasing threshold may be possible by increasing the Q factor, as opposed to decreasing the cavity diameter. Indeed, the threshold of Raman lasing in a WGM cavity is given by the following

formula [87]:

$$P_{th} = \frac{\pi^2 n^2}{\xi g_c Q_S Q_P} \frac{V_m}{\lambda_P \lambda_S}. \quad (5.1)$$

Here n is the refractive index, Q_P and Q_S are cavity quality factors for pump and Stokes wavelengths, λ_P and λ_S . The cavity Raman gain factor g_c is equal to the bulk Raman gain factor. V_m is the WGM volume and the factor ξ accounts for non-critical coupling and imperfect overlap of pump and Raman WGMs. If the Q factor is the same for pump and probe wavelengths, the Raman threshold is proportional to the ratio V_m/Q^2 . In a realistic cavity the scattering-limited Q factor is proportional to the mode volume $Q \sim V_m$ and the threshold becomes inversely proportional to the latter. From equation (5.1) one can easily see that if a Raman lasing threshold for a 100 μm cavity with $Q = 10^8$ is 100 μW , then for a 5 mm cavity with $Q = 5 \times 10^{10}$ the threshold decreases to 0.5 μW .

To our knowledge, we present the first observation of regular and cascaded operation of CaF_2 Raman laser, and the first observation of cascaded lasing in a fiber-compatible crystalline laser at a pump power below 1 mW. Stokes components of up to 5th order were observed at a pump power of 160 μW , and up to the 8th order at 1 mW. Lasing threshold of 15 μW was also observed in a 100 μm CaF_2 micro-cavity. Conversion efficiency above 60 % is demonstrated for a crystalline Raman laser. The resonators are fiber compatible and are fabricated with a very simple technique. We also demonstrate a single-mode operation of the laser in a multi-mode cavity, as well as a multi-mode operation of the laser in a single-mode cavity. Potential applications are discussed.

5.1.2 Fabrication of the resonators

We have used a very simple polishing technique to fabricate WGM resonators out of a CaF_2 crystal. A small cylinder is initially cut from a UV-grade CaF_2 blank. The cylinder is glued onto a cap which is then installed onto a high speed motor and a thin thread with diamond abrasive is used to create a region that supports the WG modes. This fabrication technique can be automated, and resonators with radius of curvature down to 10 μm and below may be produced (see Chap. 3). Diamond turning of the crystalline workpiece, followed by a conventional polishing technique was also used to fabricate single-mode resonators and microresonators. The cavities made with pure CaF_2 monocrystals are used as Raman lasing elements. One resonator was made with excimer-grade fluorite with a diameter of 5 mm. The geometry of this multimode resonator is such that its free spectral range (FSR) is 13 GHz and the cavity supports many non-fundamental WG modes within each FSR. The other cavity was made with a UV-grade fluorite with a diameter of 0.1 mm. The two resonators were cut with their axes parallel to the crystalline (111) orientation.

5.1.3 Low-threshold and cascaded generation of Raman Stokes

Cavity modes were excited with an angle-polished fiber coupler, which also serves as an output coupler for the pump and Stokes radiation. The couplers are similar to those presented in [25] and are made by cleaving the fiber at a right angle followed by angle-polishing. Such a coupler has a phase-matching evanescent field region to couple light to the WGMs of the resonator (see Fig. 5.5). In our case the fluorite resonator was 5 mm in diameter and the angle of the coupler was around 10° . We have used a single mode fiber “P3-980A-FC-5” from Thorlabs to fabricate couplers. The output of the coupler was divided between the photodetector and the spectrum analyzer with help of a beam splitter. A narrow linewidth Nd:YAG laser manufactured by Lightwave Electronics, emitting at 1064 nm, was used to excite the WGMs in the cavity. Raman emission was observed with an optical spectrum analyzer. All experiments were carried out in a clean room and all measurements were performed for TE polarization of the WGMs. A simplified Pound-Drever-Hall (PDH) locking technique [12] allowed us to continuously pump the WGM mode of the cavity, and the resulting Raman emission was monitored in a CW mode. Simplified schematics of the setup are shown in Fig. 5.1. In the process of threshold measurement, the laser was locked to a cavity mode at several

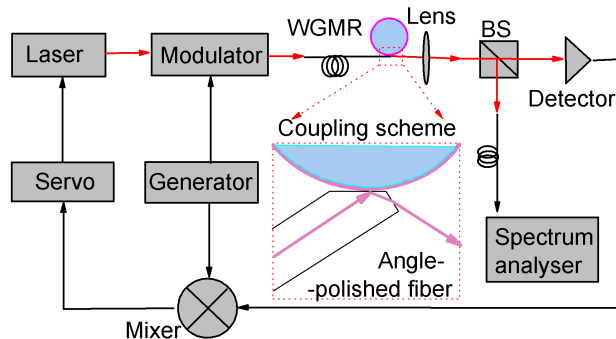


Figure 5.1: Setup diagram with inset showing the coupling schematics. A PDH-locking technique is used to stabilize the power in a cavity.

pump power values. Pump power refers to the power absorbed in the cavity. The results presented in Fig. 5.2 correspond to Raman lasing when a WG mode with a loaded optical $Q = (2.6 \pm 0.3) \times 10^{10}$ is used, with a coupling efficiency of 40% as measured from the critical coupling point. Clamping of the intracavity power is evident at a point where the second Stokes component appears. This behavior is natural for WGM-based Raman lasers, as was shown elsewhere [95]. Given the threshold of $3 \mu\text{W}$ at this Q factor and equation (5.1), we see that if a different mode with a Q factor of 5×10^{10} and the same effective volume is used, a threshold well below $1 \mu\text{W}$ should be expected. It was shown [95] that the optimal coupling for Raman lasing is about 89% of critical, which also implies some

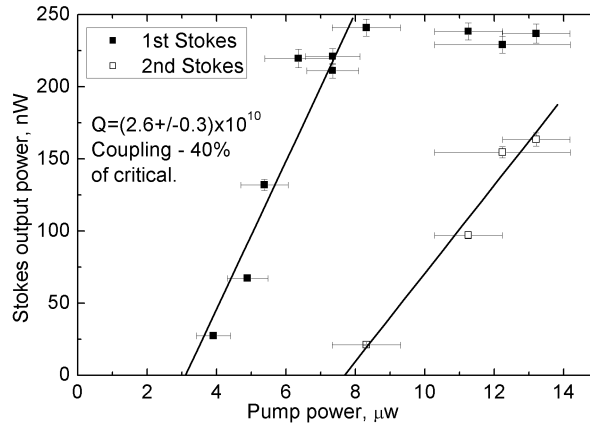


Figure 5.2: The output optical power as a function of the pump power for non-optimized operation of the Raman laser based on a 5 mm cavity

room for further optimization. Thus the crystalline WGM resonator has the lowest Raman lasing threshold available today, as the threshold of other sources is at least 20 times higher. The efficiency of our laser was made small by operating in an under-coupled regime with the purpose of measuring the lasing threshold. The maximum observed unidirectional efficiency for the 1st Stokes component was $P_{Stokes}/P_{pump} = 0.24$ in cascaded mode with 7 Stokes components present.

The vibrational spectrum of CaF_2 has nine phonon branches — six optical and three acoustic. Only one vibration with $\nu = 322 \text{ cm}^{-1}$ is Raman-active. The Raman wavenumber and gain linewidth depend on temperature [97, 98]. The wavelengths of the Stokes components may be computed and are found to be in direct agreement with the experimental results presented in Fig. 5.3. The inset

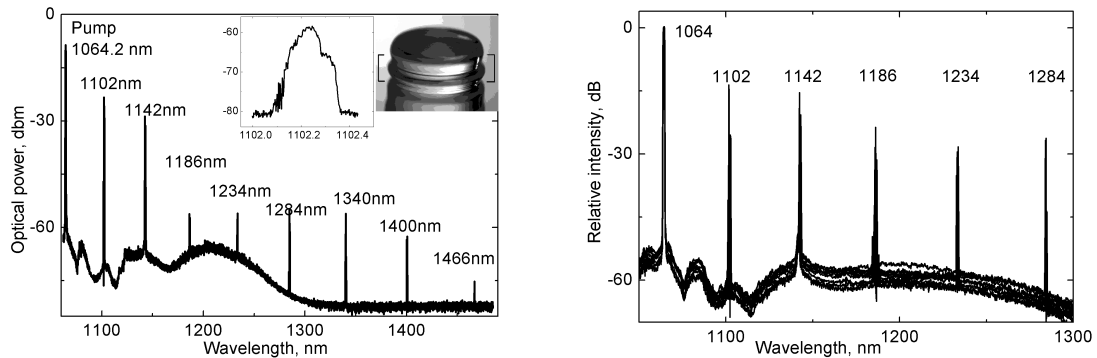


Figure 5.3: Left panel: cascaded operation of the Raman laser. Insets show the photograph of a cavity and the detailed spectrum of the first Stokes component. Power is as seen on the spectrum analyzer; the actual pump power is 1 mW. Right panel: cascaded operation of the Raman laser. The pump power is $160 \mu\text{W}$. The spectrum is combined from 9 consecutive measurements obtained in an unlocked regime.

shows the 1st Stokes spectrum, which is formed by many WG modes lasing within each FSR of the cavity. The spectrum width gives a rough estimate for the Raman gain linewidth $\delta\nu \simeq 1.7 \text{ cm}^{-1}$.

Cascaded operation of the laser with Stokes components of up to the 8th order was observed in an unlocked regime, when the pump laser frequency is quickly scanned around the WGM. A high pump power of about 1 mW produced a nonlinear behavior of the mode so pronounced that the PDH locking was impossible. As a consequence, the power levels of Stokes components in Fig. 5.3 were fluctuating over the time of the measurement. These components only indicate the presence of Raman emission at the given wavelengths. Cascaded Raman lasing has been previously observed in microdroplets. One exotic example is SRS in liquid hydrogen droplets [27] observed at rather high input power levels. Efficient Raman lasing with 5 Stokes orders was also observed in fused silica microcavities [72].

We have also observed Raman emission from a smaller cavity made with a different specimen of CaF_2 . It is interesting to compare the operation of our laser with the one discussed in [72]. The

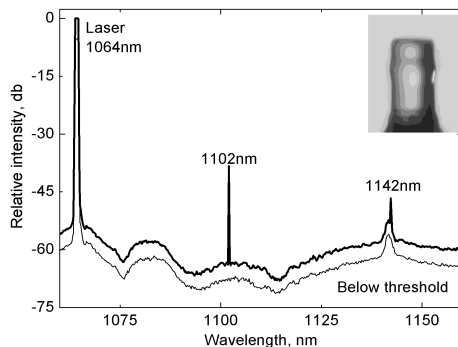


Figure 5.4: Cascaded Raman lasing in a $100 \mu\text{m}$ fluorite microcavity. The pump power is about $100 \mu\text{W}$.

microsphere with the lowest threshold had a diameter of about $55 \mu\text{m}$, a quality factor $Q = 10^8$, and a first Stokes threshold of about $60 \mu\text{W}$. In the fluorite cavity presented here, the modes occupy a larger space as the resonator diameter is $100 \mu\text{m}$. The value of the quality factor $Q = 10^8$ is obtained with direct linewidth measurements. The Raman lasing threshold in the fluorite cavity is estimated to be below $15 \mu\text{W}$, which may suggest a stronger Raman gain in CaF_2 . This argument is supported by a study of scattering in fluorite [71] where the gain for CaF_2 was found to be higher as compared to fused silica, while having much narrower spectral width. Raman gain was also theoretically estimated in Sec. 4.2. At a pump power of about $100 \mu\text{W}$, cascaded operation of the Raman microlaser is observed. No anti-Stokes emission was found for our cavities.

5.1.4 High-efficiency and single-mode Raman lasing

The example of the coupler and the profile of a resonator that was used in this set of experiments are shown on Fig. 5.5. To implement a PDH frequency lock, the pump beam was phase-modulated at

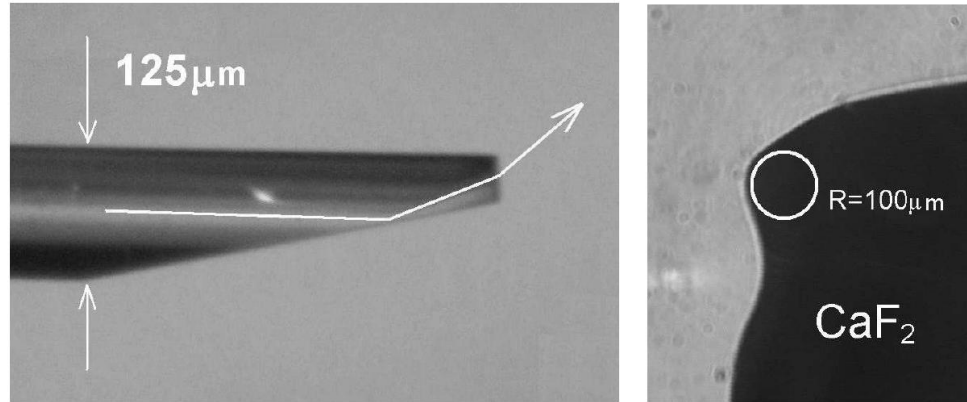


Figure 5.5: An angle-polished fiber coupler (left). Single mode fiber is polished at an angle, which was computed to optimize coupling to a 5 mm CaF_2 disk. An approximate ray path is shown with a white arrow. Shadow photograph of a CaF_2 resonator (right). The white circle shows that the radius of curvature of the disk in the WGM localization area is around $100 \mu\text{m}$.

0.6 MHz with a resonant electro-optical modulator (EOM) and the WGM cavity acted as a frequency discriminator. The amplitude of the reflected portion of the pump beam, produced at the output of the coupler contains a component at the modulation frequency. This component was recorded by a Thorlabs photodetector “DET10C” and multiplied by a phase-shifted modulation signal with the help of a mixer to obtain the PDH error signal. Schematics of the experimental setup is similar to the one from the previous section and is shown on Fig. 5.6. Phase shifting, used to optimize the

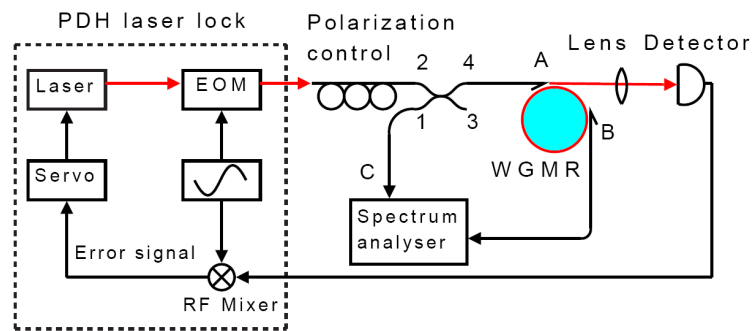


Figure 5.6: The setup diagram. A PDH locking technique is used to stabilize the power in a cavity. 'A' and 'B' denote input and output angle-polished fiber couplers.

error signal, was achieved by varying the frequency of excitation of the resonance transformer in the phase modulator. The error signal was amplified and filtered with a low noise voltage amplifier “SR560”, and fed back to the laser piezo. Typical error, transmission, and reflection signals for the

case of linear modes in a resonator are shown in Fig. 5.7. Pumping of the Raman laser is performed

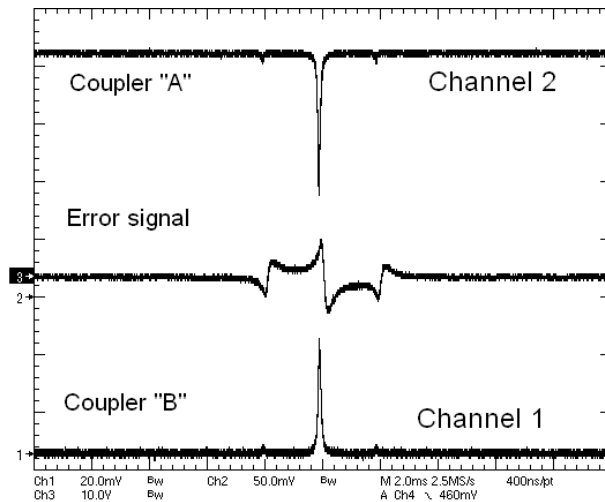


Figure 5.7: Optical power from coupler “A” (channel 2), “B” (channel 1) recorded with the photodetectors and the error signal

by the same mode that is used for frequency locking. It should be noted that the observed WG modes were non-Lorentzian, as thermal and Kerr nonlinearities were present at the level of power that was used. Nevertheless, the error signal still had a linear region which allowed us to successfully lock the laser. When the laser was frequency-locked to a cavity, the amplitude noise of the reflected signal was around 20 %, which may be significantly reduced by upgrading the servo.

When a resonator is pumped, the Raman gain is created symmetrically for the counter-propagating sets of WG modes. It may be argued that the coupling losses seen by each of the modes in the pair of counter-propagating modes might be different due to the asymmetry of the refractive index inside the angle-polished fiber coupler. However, coupling losses are defined by the overlap integral between the cavity mode and the field configuration in the fiber and do not depend on the sign of the wave vector, as the WGM resonator is linear and symmetric [99, 100]. We assume that the power in each of the Raman lasing modes of a pair is equal. The lasing linewidth, or coherence of the pair of lasers, could in principle be measured by recording a beatnote of the pair of modes on the photodetector.

The two fiber couplers and the reflection port (90/10 coupler) were used to monitor these two laser outputs simultaneously. The free beam formed by the coupler “A” suffered attenuation from the reflection loss at the cleaved fiber surface, lens, and detector surfaces. If we assume these losses to be 4% each, which corresponds to the reflection coefficient at a glass surface, then the power inside the fiber is higher than that observed at the detector by a factor of $\simeq (0.96)^{-4} = 1.18$. This correction is taken into account in the following estimates.

The maximum measured coupling efficiency was above 70 % for the input “A” and above 80 % for the output “B” coupler. It is worth noting that critical coupling approaching 100 % may be

achieved for the WGM resonators. The intrinsic optical Q factor of the WG mode, measured at pump wavelength of 1064 nm, is found to be $(6.9 \pm 0.7) \times 10^9$. This value was derived from the linewidth ($\simeq 40.5$ kHz) of the mode resonances in the undercoupled regime, when no Raman lasing was present. A splitting of around 135 kHz caused by the Rayleigh-scattering-induced coupling between the counter-propagating modes was also observed. In a particular measurement, the mode

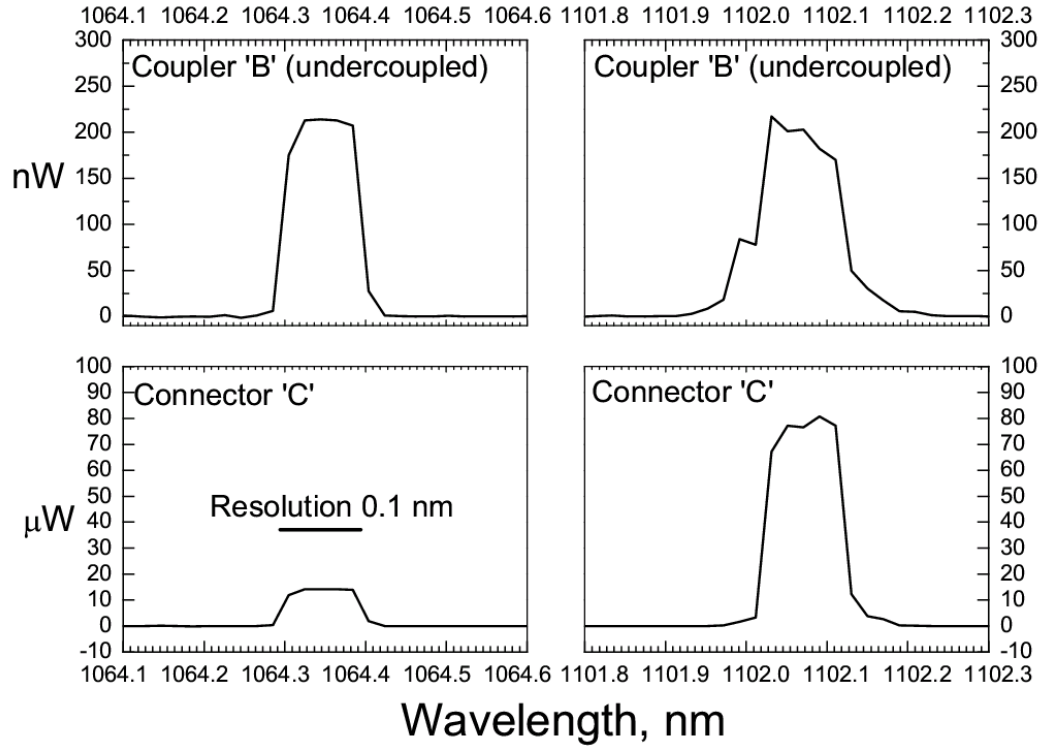


Figure 5.8: Spectra of input and output power as recorded by the coupler B and the fiber connected to output 4 of the port. See Fig. 5.6 for details.

was pumped so that the input coupler transmission loss was around $244 \mu\text{W}$. This doesn't include the forward Stokes power which was emitted at a different angle and missed the detector. The maximum achievable coupling for the WG mode corresponded to $277 \mu\text{W}$ transmission loss or about 50 % of the coupler transmission. Fig. 5.8 shows power spectra of the transmitted and reflected optical signals as seen on the spectrum analyzer "Yokogawa AQ6319". A transmission ratio for 4-1 direction of the reflection port was measured to be 0.0145 at the pump wavelength, so the reflected power measured with a spectrum analyzer was adjusted accordingly, giving the optical power values in the fiber. The 90/10 coupler was designed for 1550 nm, so the actual transmission ratios at the wavelength of 1064 nm was different from 90 % and 10 %. From Fig. 5.8 it can be seen that there is $14 \mu\text{W}$ of reflected pump laser radiation and $80 \mu\text{W}$ of backward Stokes radiation, shifted by 9.72 THz (38 nm) from the pump laser frequency. From the forward coupler we see that the power of the pump laser and the Stokes component are equal, and since Raman lasing is symmetrical for counter-propagating modes

we derive the forward lasing Stokes and pump laser power of $80 \mu\text{W}$. This adds up to $254 \mu\text{W}$ which is the total power loss in the cavity, within the experimental uncertainty. Thus the bidirectional Raman conversion efficiency for this particular mode is $100\% \times 160/244 = 65\%$. As compared to the 24% unidirectional efficiency of Sec. 5.1.3 observed when 8 cascaded lasing multimode Stokes components were present, the 32% unidirectional efficiency in the present experiment is observed for the single lasing Stokes component and a near-single-mode operation.

The refractive index of fluorite at pump and Stokes wavelength is 1.43 and the mode TE_{111} of a 5 mm cavity has a volume of $2.7 \times 10^{-12} \text{ m}^3$. We assume Q_S and Q_P to be 3.5×10^9 and a Raman gain coefficient of $2.4 \times 10^{-13} \text{ m/W}$ (as derived in Sec. 4.2). Using equation 5.1 we obtain a Raman threshold of $16 \mu\text{W}$ for $\xi = 1$, comparable to the measured threshold of $78 \mu\text{W}$. The discrepancy may be understood if we assume that the excited mode was not fundamental TE_{111} mode, but rather a mode with larger effective volume. The threshold would increase with increasing volume of the mode. Additionally, the intermodal coupling which is responsible for the counter-propagating mode splitting also leads to the reduction of the intracavity power buildup by a factor of 2 in the case of strong modal coupling [95]. The factor ξ in equation (5.1) is less than 1 as the coupling and modal overlap are not ideal.

From additional measurements it was found that the spectrum of Fig. 5.8 typically consists of several lasing Stokes WG modes, as presented on the left panel of Fig. 5.9. The strongest lasing mode exceeds the other modes by at least 15 dB, making it nearly a single-mode lasing spectrum. The right panel of this figure presents a similar measurement on a linear scale. Only forward Stokes emission was recorded, making it impossible to obtain the efficiency. The spectra in Fig. 5.9 were obtained

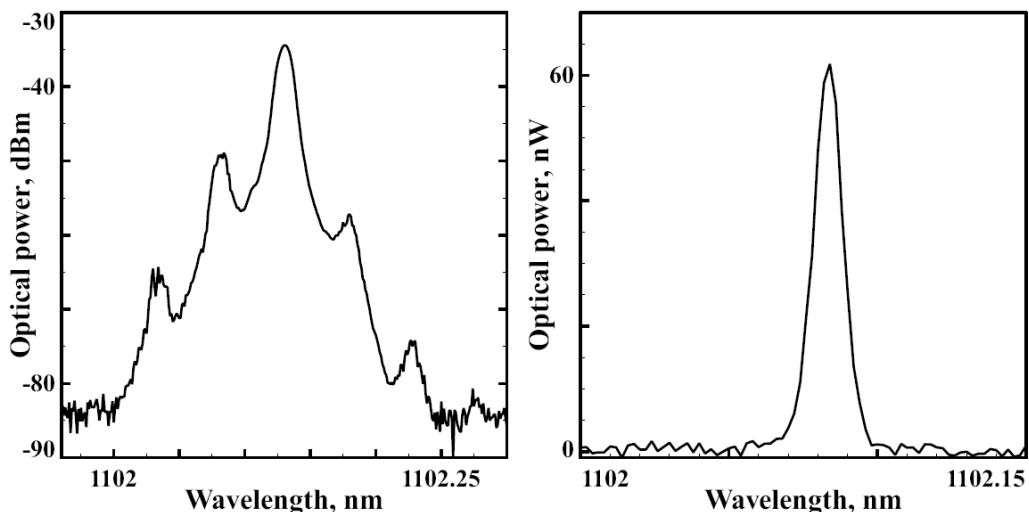


Figure 5.9: Optical power spectrum of lasing Stokes component on log-linear (left) and linear scales. Spectra were recorded for 2 different pumping WG modes. Optical power is not calibrated.

for different pumping WG modes with intrinsic Q factor of 7×10^9 for the left spectrum and 10^{10}

for the right spectrum. It is seen that the lasing modes are separated by the resonator FSR, so that only the modes from a particular family of modal indices lmq , with different l and similar $l - m$, are lasing. The number of lasing modes was experimentally found to depend on loading conditions and modal Q factor. Increasing the Q factor reduced the number of peaks in the spectrum. Even though the spectrum of our multimode cavity is rich with higher-order azimuthal modes, the combination of a high Q factor and a narrow Raman gain made it possible to observe single-mode lasing. In these measurements the Stokes power was equal to the pump power in the forward direction, as monitored by the output coupler in the undercoupled regime. The spectrometer's resolution in Fig. 5.9 is 0.012 nm, and the cavity's free spectral range (FSR) is 0.049 nm.

We have also observed Stokes lasing modes in a special single-mode cavity (Fig. 5.10). This cavity is a cylinder on which a small 5×3 micron waveguide is formed with a diamond-turning process. Such a waveguide supports only one WG mode per cavity FSR. Although many Stokes modes separated by the cavity's FSR were found to be lasing in this resonator at a pump power of 2.4 mW, a true single mode operation may be achieved if the Q factor is high enough and mode competition for Raman gain is strong. The multimode lasing in a single mode cavity may be explained by weak

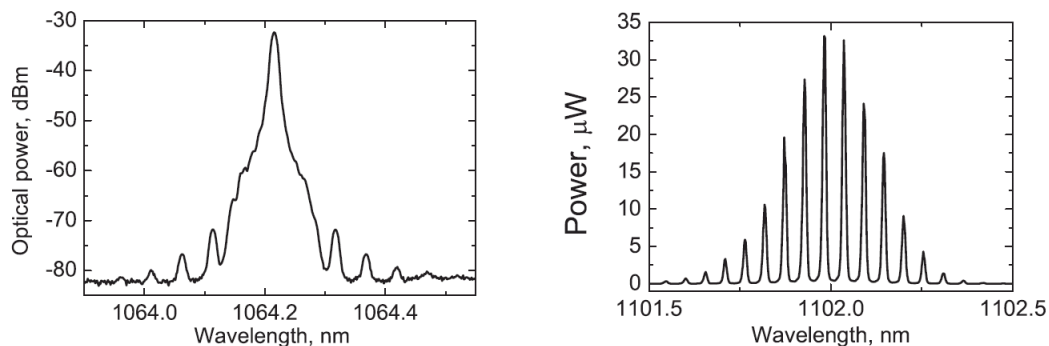


Figure 5.10: Pump and Stokes spectra for the single mode WGMR. Resolution is 0.01 nm. Pump power is 2.4 mW. About 40 lasing modes were observed above the noise level.

mode competition. The loaded Q factor of around 4×10^8 , intrinsic $Q = (7.2 \pm 0.1) \times 10^8$, was too low for any specific mode to consume all the Raman gain available. Our diamond-turning apparatus was not accurate enough to provide the single-mode cavity with a Q factor higher than 10^9 . The application of a more elaborate diamond-turning process should enable higher Q factors, and thus a true single-mode operation of a Raman laser based on a single-mode fluorite cavity. The sidebands on the pump laser spectra were only observed in the forward direction. These weak features might be explained by four wave mixing between the pump and the Stokes components.

5.1.5 Conclusion

The power that can be obtained from our Raman lasers is limited by Kerr and thermal nonlinearities and by cascaded Raman lasing process. Increasing the power in the pump mode leads to cascaded lasing where higher-order Stokes components appear, which limits the efficiency of single-mode operation. Nonlinearities also make the shape of the cavity mode significantly different from a Lorentzian at higher pump powers, making the PDH locking technique unreliable. If a higher power is required, a WG mode with a larger volume and lower Q factor may be selected. Another solution would be to reduce the Q factor at the Stokes wavelength by introducing a wavelength-selective absorber.

We have demonstrated Raman lasing with CaF₂ WGM cavities. Lasing threshold at the microwatt level, high efficiency, and single-mode operation were achieved. The low Raman lasing threshold and efficient cascaded operation are made possible by the ultrahigh optical quality factors of the WGMs of crystalline cavities. For a 5 mm cavity diameter, the threshold of the first Stokes was demonstrated to be as low as 3 μ W. Cascaded operation with 8 Stokes components is observed for the first time with only 1 mW of pump power. Efficiency of Raman conversion as high as 65% was observed. A high-Q-factor, single-mode WGMR may be used to generate a single-mode emission. Alternatively, a smaller cavity with a near-single-mode spectrum and high Q factor may be used. Single-mode Raman emission is useful in many spectroscopic applications. Additionally, the multi-mode emission could be used to generate relatively stable GHz-range beatnote signals. It was shown in [101] that the millimeter-sized cavity may have its mode frequency relatively stable at the 10^{-14} level in 1 second, which corresponds to 3 Hz if the wavelength is 1 μ m. Thus one may expect the Raman laser to be relatively stable and have a narrow linewidth, leading to narrow microwave beatnote signals that may be generated. Fiber compatibility of our laser may be utilized in compact and efficient optoelectronic devices. A wide variety of optical crystals in combination with crystalline WGM technology make compact, fiber-compatible, tunable Raman lasers possible. By a proper choice of a nonlinear crystal, one may achieve the generation of many different Stokes components with low threshold power and high efficiency.

5.2 Stimulated Brillouin scattering

Stimulated Brillouin scattering with both pump and Stokes beams in resonance with different whispering gallery modes of an ultrahigh Q CaF₂ resonator is demonstrated for the first time. The resonator is pumped with 1064 nm light and has a Brillouin lasing threshold of 3.5 μ W. Potential applications include optical generation of microwaves and ultrasensitive gyros.

5.2.1 Introduction

Generation of the reflected Brillouin Stokes component in a fiber ring resonator may be viewed as a lasing process. Instead of a population inversion, the gain is provided by light scattering on the acoustic wave, which is generated through electrostriction. While scattering may be a power limiting factor in fiber communications, Brillouin lasers have several attractive features. Stokes components may be generated in a cascaded mode with threshold below 1 mW [102, 103, 104]. Detecting these components together may generate microwave signals in the 10–100 GHz range. An interesting feature of Brillouin lasers is the linewidth narrowing effect [105, 106] where width of the Stokes line may be reduced by a factor of up to 10^4 , as compared to the pump laser linewidth [107]. Stokes linewidths as narrow as a few hertz were demonstrated [108, 109] in a fiber-ring cavity with finesse of around 100, implying good short-term stability of a microwave signal that can be generated. In addition, it was found that a relative intensity noise is also reduced in a Brillouin laser [110]. Thus applications of the Brillouin fiber-ring laser include laser gyros [111, 112], linewidth narrowing, microwave frequency generation [113, 114] and high-rate amplitude modulation.

Ultrahigh Q WGM micro- and mini-resonators [49, 115, 96, 33] are optical elements in which the efficiency of many nonlinear optical processes exceed what can be achieved with fiber-ring resonators by orders of magnitude. These include three- [31, 116] and four-wave mixing [61, 117, 118]. Strong spatial confinement of light combined with a long interaction time with the nonlinear medium of the resonator results in a significant decrease of the threshold for regular lasing [119, 120], stimulated Raman scattering, and other nonlinear processes [121, 23, 5]. Scattering of light from low-frequency mechanical modes of the silica microtoroids has also been studied recently [122].

Unique features of WGM resonators and Brillouin fiber lasers lead one to expect superb characteristics of a WGM-based Brillouin laser. In particular, the linewidth narrowing depends on both the optical and acoustical quality factor of the resonator and may be computed as follows [105]:

$$\Delta\nu_{Stokes} = \frac{\Delta\nu_{pump}}{\left(1 + \frac{\pi\gamma_B}{\Gamma_C}\right)^2} \quad (5.2)$$

where γ_B is the Brillouin gain bandwidth and Γ_C is the optical loss rate of a cavity. We can estimate reduction ratio for a crystalline CaF_2 resonator. Brillouin gain bandwidth in fluorite is 12.2 MHz [123], and resonators with a quality factor on the order of 10^{11} were recently demonstrated [3, 78]. Thus linewidth-narrowing factors on the order of 1.6×10^8 may be possible at a pump wavelength of $1 \mu\text{m}$, which is 4 orders of magnitude better compared to fiber-ring resonators. If the pump laser linewidth is 5 kHz, the expected Brillouin laser linewidth is just $30 \mu\text{Hz}$. Mixing two Stokes from the same cavity could produce microwave beatnotes with narrow linewidth:

$$\Delta\nu_{microwave} = \sqrt{\Delta\nu_{B1}^2 + \Delta\nu_{B2}^2} = 42\mu\text{Hz}. \quad (5.3)$$

Theoretical analysis shows [101] that a laser locked to a crystalline cavity may have stability on the order of 10^{-14} . Hence a crystalline WGMR-based Brillouin laser could be used for optical frequency standards, sensitive optical gyros, and all optical compact microwave generators, as well as laser-line-narrowing devices. It should be noted, however, that at room temperature the linewidth of the Stokes component will be limited by noises caused by temperature fluctuations. If SBS were to be observed in fused silica WGM resonators, the linewidth reduction ratio would be limited at around 2.8×10^6 by the value of the maximum optical Q factor. Silica resonators also require isolation from atmospheric water, and do not support spectrum tailoring as was recently demonstrated for crystalline resonators (Chap. 3).

Stimulated Brillouin scattering (SBS), while being a common nonlinear optical effect, is generally believed not possible in the ultrahigh-Q solid-state microresonators, even though the bulk Brillouin gain generally exceeds the Raman gain. One reason is that the width of an SBS gain is generally around tens of MHz, while the FSR of WGM resonators is typically three orders of magnitude larger, and the cavity resonance does not cover both pump and Stokes frequencies. It is argued, that there would be no WG mode present at a Brillouin offset to support the Stokes beam. In addition, the acoustic frequency has to be resonant with one of the mechanical modes of a microresonator, otherwise the acoustic wave interferes destructively with itself. Finally, pump mode, Stokes mode and acoustic mode must have a non-vanishing overlap integral. Speed of sound depends on direction and polarization in crystals, making it harder to fulfil the resonant SBS conditions in crystalline microresonators. This situation is alleviated in either large ring resonators, where FSR is comparable to the Stokes offset, or in low-Q liquid microdroplets, where optical resonance covers both pump and Stokes frequencies [124, 125, 126, 127, 128, 129, 130, 131, 132]. Microdroplets, however, have low Q and are not fiber compatible, while fiber-ring resonators have low Q and large dimensions. The density of the WGM spectrum increases with WGM size. Therefore, it is reasonable to expect that SBS could be present in any millimeter-scale WGM resonator.

This section shows that SBS can occur in ultrahigh-Q, millimeter-scale WGM resonators that support two modes separated by the SBS frequency shift. The first ever observation of an efficient SBS in a CaF_2 WGM resonator is presented. It is shown that SBS can be either enhanced or suppressed by manipulating the modal structure of the optical resonator.

5.2.2 Experimental observation of Brillouin and Raman lasing

Two ultrahigh-Q, single-crystal CaF_2 WGM resonators were fabricated. Resonator 1 was fabricated with a UV-grade fluorite from Edmund Optics and had a larger radius of curvature as compared to resonator 2, made with an excimer-grade fluorite from Corning. A Nd:YAG laser with 5 kHz linewidth manufactured by Lightwave Electronics was used to excite WGMs at the wavelength of 1064 nm. The diameters of the resonators were determined from the FSR, measured as a spacing

between multiple Raman lines observed at 1102 nm, and the value of the refractive index of CaF_2 at this wavelength, $n = 1.4283$. The cavities are shown in Fig. 5.11. The spectra of the resonators contain an abundance of modes with the average spacing of 25 MHz for both polarizations. The laser

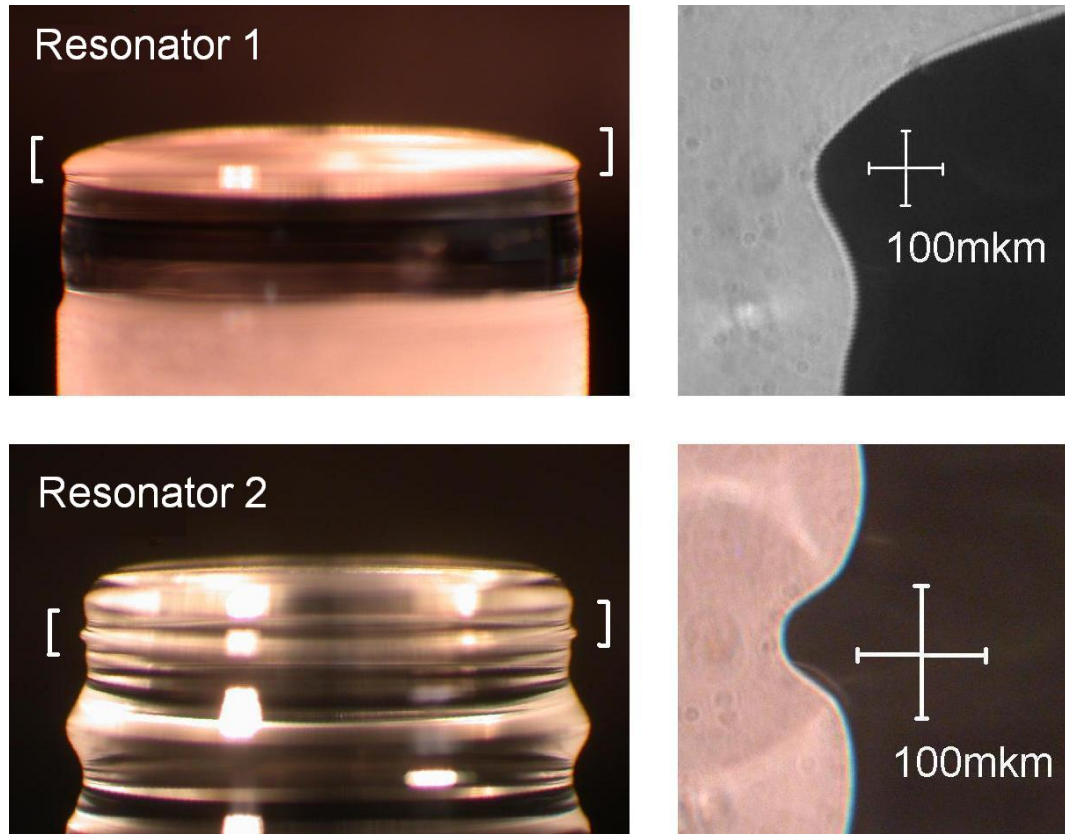


Figure 5.11: Fluorite resonators. WGM localization areas are highlighted with the white brackets on the left. Shadow photographs of the highlighted regions are on the right. Diameters are 5.52 mm for resonator 1 and 5.21 mm for resonator 2.

frequency was locked to a selected cavity mode using a simplified Pound-Drever-Hall technique. A signal generator was used to provide the excitation for the resonant phase modulator. This signal was also used to synchronize the lock-in amplifier SR844, which operated as a frequency mixer and servo. This technique made it possible to maintain a fixed optical power in the cavity mode.

Alignment of the angle-polished fiber couplers, similar to those presented in [25], mounted onto the three-axis piezo positioning stages provided input and output coupling efficiencies of up to 80%. The light that was scattered backwards by the cavity mode was branched into the arm of a 90/10 fiber coupler. The setup schematically shown in Fig. 5.12 was used to measure the power and spectral properties of both forward and backward beams with help of a Yokogawa AQ6319 optical spectrum analyzer and a Thorlabs detector “DET10C”. A WGM was excited with approximately $50 \mu\text{W}$ of optical power in a measurement conducted with the first cavity. The spectrum of light from the coupler B (Fig. 5.13) revealed the presence of a Stokes line offset by 34.9 GHz and a weak Stokes

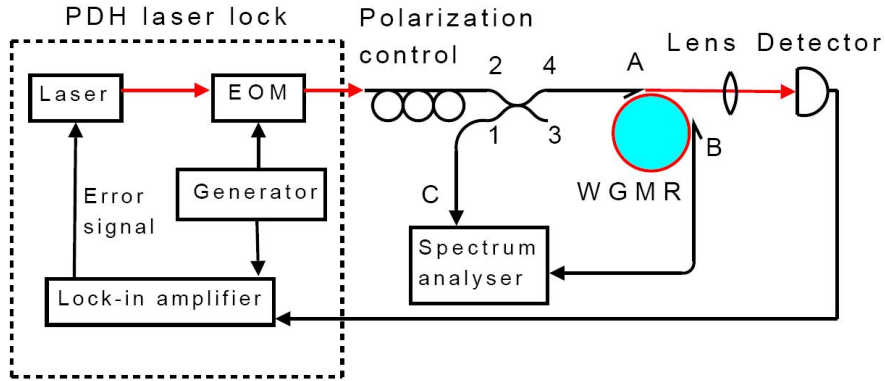


Figure 5.12: Experimental setup diagram. Laser is locked to a cavity mode; the optical power in the fiber can be monitored in forward and backward directions.

line offset by 17.5 GHz. The intensity of the Stokes line at 34.9 GHz was 13.9 dB weaker than the pump. Neither stimulated Raman scattering (SRS) nor four-wave mixing (FWM) oscillations were observed in this measurement. The difference of intensities of the pump and the Stokes line at 34.9 GHz decreased to 9.4 dB when the pump optical power was further increased. Two groups of SRS lines appeared around 1101.8–1102.3 nm and 1142.4–1142.9 nm with this increase of power. The peak level of the Raman lasing lines were -16.2 dB for the 1st Stokes and -11.9 dB for the 2nd Stokes with respect to the pump. A set of similar measurements was made with the second cavity.

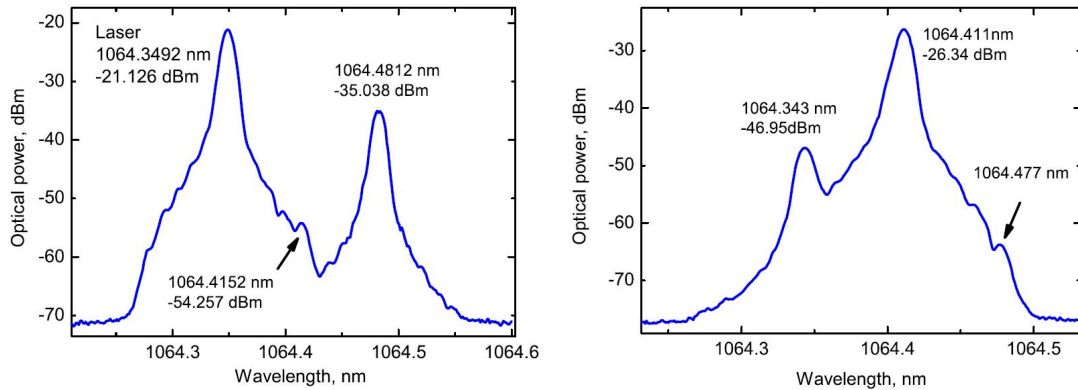


Figure 5.13: (Left) Optical spectrum around the laser line for resonator 1 obtained from coupler B. The pump power is $50 \mu\text{W}$. The gap between coupler B and the cavity was increased, which explains lower power at the spectrum analyzer. The two Stokes lines have frequencies red-shifted by 17.465 GHz for the weak Stokes and by $17.465 \times 2 = 34.93$ GHz for the strong Stokes line. The width of each line is limited by the optical spectrum analyzer resolution of 0.012 nm. (Right) Backward signal from coupler C for resonator 2. Stokes offset is 18 GHz for the first and 17.5 GHz for the second relative to the first.

This time the pump power was lower, and no Stokes line around 35 GHz was observed. However, we carried out simultaneous measurements of the forward and backward optical spectrum using couplers B and C (see Fig. 5.12). Typical spectra are shown on Fig. 5.14. From this spectrum we

see that the intensity of the backscattered Stokes line exceeds the backscattered pump light. The asymmetry of the spectra may be explained by the residual power leakage between inputs 2 and 1 of the 90/10 coupler, increasing the backward signal at the pump wavelength. The excited WGM had

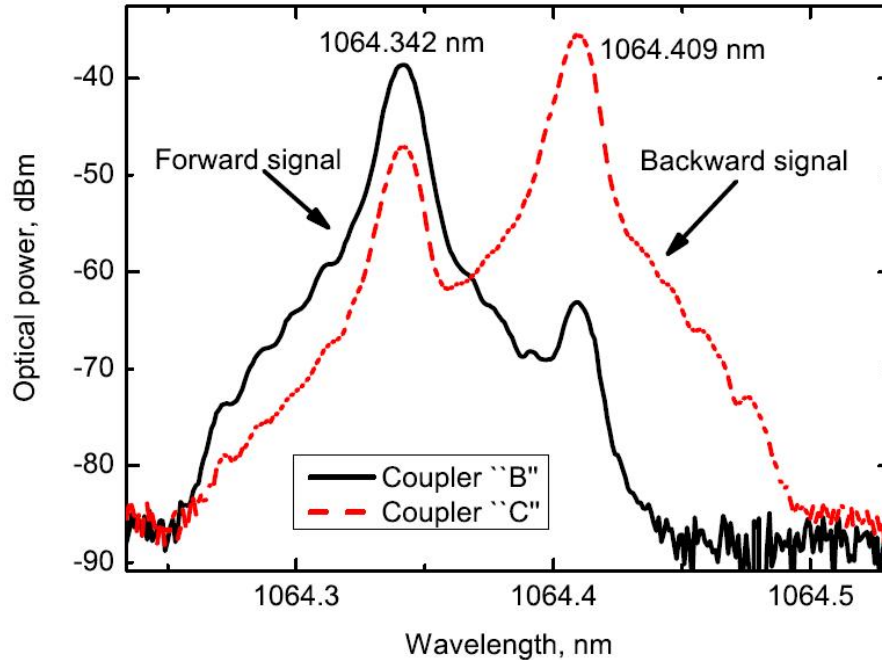


Figure 5.14: Typical optical spectra from couplers B and C, representing forward and backward signals. Stokes offset is 17.7 GHz.

a coupling efficiency of 70%, loaded Q factor of 4×10^9 , and an intrinsic Q of around 1.4×10^{10} . The spectrum of the light exiting the resonator in the backward direction is shown in Fig. 5.13 (right). Optical pump power was reduced to $2.9 \mu\text{W}$, below which the first Stokes line was still present but weak. Above this power the intensity of the Stokes line jumps by around 10 dB and grows quickly until it reaches the levels presented in Fig. 5.13 (right). Hence, the threshold of the process was estimated to be around $3 \mu\text{W}$ for the mode with loaded Q of 4×10^9 . At pump power well above $10 \mu\text{W}$ Raman lasing was observed, the spectrum of which is shown on Fig. 5.15. A modulation of the SRS intensity similar to the spectrum of the Stokes line observed near the pump is visible.

5.2.3 Interpretation of experimental results

The experimental data from the previous section represents a direct observation of SBS. The spectra of the resonators had no observable resonance splitting, which means that only a minor amount of Rayleigh scattering is present for any given WGM. The excitation of a WGM at 1064 nm created a Stokes line offset by 17.5 GHz, which propagated in the direction opposite to the pump, as shown in Fig. 5.13 (right). The optical field of this line creates a cascaded Stokes component at the additional

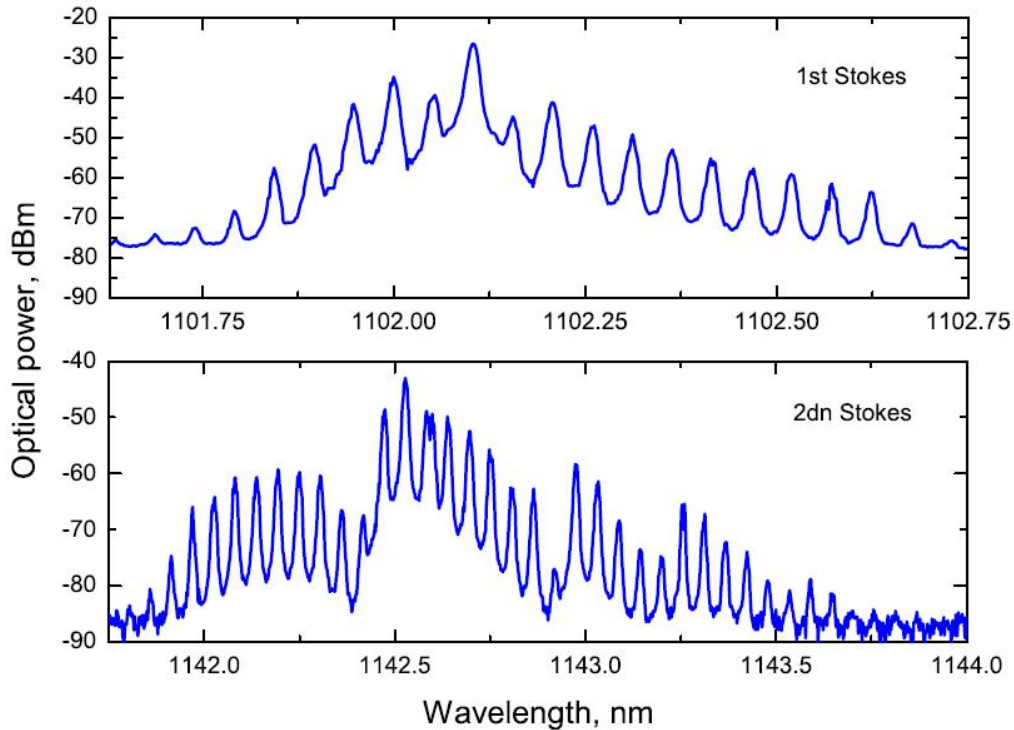


Figure 5.15: Raman lasing Stokes observed at pump power above $10 \mu\text{W}$ in the second resonator

offset of 17.5 GHz propagating in the same direction as the initial pump beam (Fig. 5.13 (left)). A small feature at the double offset on Fig. 5.13 (right) may be explained as Rayleigh scattering from the second Stokes line visible at Fig. 5.13 (left). The weak feature at Fig. 5.13 (left) may be understood also as Rayleigh scattering from the first Stokes line seen at Fig. 5.13 (right). These two Stokes lines modify the Raman gain in the resonator, which leads to the SRS spectrum with modulated intensity as seen in Fig. 5.15. Given the OSA resolution of 0.012 nm and the wavelength repeatability of 0.002 nm (offset error of 1 GHz), we conclude that the two offsets of the observed SBS Stokes lines are multiples of 17.7 GHz. In what follows we show that this scattering is given by the longitudinal phonon branch of the fluorite crystal.

5.2.4 Brillouin scattering in fluorite

Let us compute the Brillouin offset in a CaF_2 WGM resonator. The WGM is modeled as a toroid with axis along the (1,1,1) crystalline orientation. It is assumed that the phonons participating in the SBS do not form standing waves in the resonator. The phonon lifetime $\tau_{ph} \approx 0.08 \mu\text{s}$ is the inverse of the spectral width of the SBS gain, which is approximately 12.2 MHz full width at half maximum [123], and is much smaller than the roundtrip time of the sound wave in the resonator — $2\pi a/V_s = 2 \mu\text{s}$. Hence stimulated Brillouin scattering in millimeter-sized resonators is similar to

Brillouin scattering in bulk.

To find the frequency offset of the SBS one needs to know the direction of the wave vector of light in the WGM with respect to the crystalline axes. Frequencies of the SBS active phonon branches do not depend on the polarizations of participating photons. The propagation direction of the electromagnetic wave is given by the following vector:

$$\mathbf{k} = \left(\frac{\cos \phi}{\sqrt{6}} - \frac{\sin \phi}{\sqrt{2}}, \frac{\cos \phi}{\sqrt{6}} + \frac{\sin \phi}{\sqrt{2}}, -\sqrt{\frac{2}{3}} \cos \phi \right), \quad (5.4)$$

where ϕ is the azimuth angle, representing different points along the resonator circumference. The geometry of the system allows back scattering only, so the Stokes wave has a wave vector

$$\mathbf{k}' \simeq -\mathbf{k}. \quad (5.5)$$

The wave vector for the phonons participating in the scattering is $\mathbf{q} = \mathbf{k}' - \mathbf{k}$, so the unit wave vector for the acoustic wave is $\vec{\kappa} = -\mathbf{k}$. Calcium fluoride is a cubic crystal described by three independent elastic constants [133, 134, 135], which are also given in the specification sheet of our fluorite sample: $C_{11} = 1.6420$, $C_{12} = 0.4398$, $C_{44} = 0.3370$ [$\times 10^{11}$ Pa]. Substituting these values into the set of equations presented in [80] we numerically find the frequency shifts of the Brillouin Stokes components as a function of angle ϕ for three different elastic waves (see Fig. 5.16). Computations were carried out in “Maple” and “Mathematica” software packages. Only one

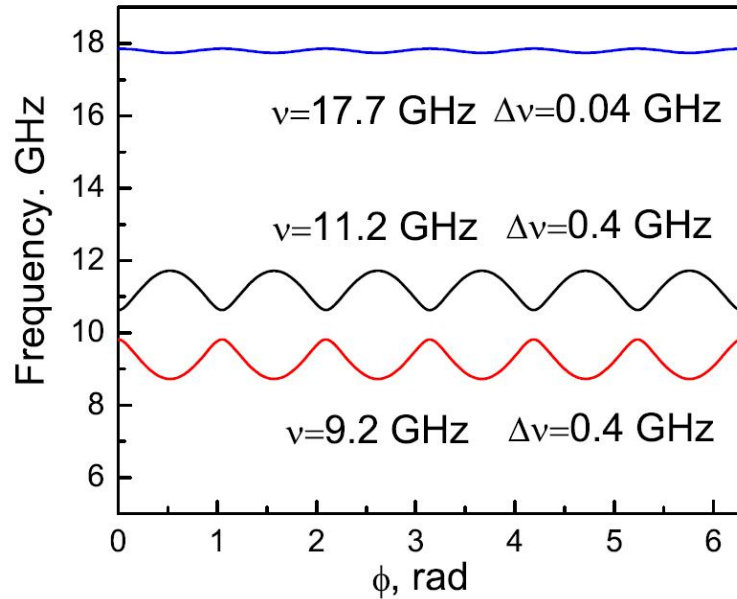


Figure 5.16: Characteristic frequency of the acoustic wave as a function of the azimuth angle

solution has a frequency shift that depends weakly on the azimuth angle. The standard deviation is

computed to be 40 MHz for this case, with 112 MHz peak-to-peak frequency change. The other two elastic waves have a standard deviation of frequency of about 0.4 GHz. Therefore, the 17 GHz branch has the maximum probability for exciting the stimulated process in the resonator. This prediction is in agreement with the experimental observations. It is worth noting that the Brillouin frequency shift for the case of backscattering along the axis of a cubic crystal can be approximately found as

$$\nu = \frac{2n}{\lambda} \sqrt{\frac{C_{11} + C_{12} + 2C_{44}}{2\rho}} \simeq 17.7 \text{ GHz.} \quad (5.6)$$

Fig. 5.16 corresponds to off-axis light scattering, as modeled for the resonator. Further analysis shows that polarization of the phonons is nearly collinear with their wave vector in the case of the highest-frequency branch. Hence, the observed SBS process results from the interaction of light and longitudinal sound wave.

In the ideal case of spectrally singular pump and Stokes optical beams, the bulk Brillouin line-center gain g_b can be estimated as (see Eq. 8.3.24 of [86])

$$g_b = \frac{\gamma_e^2 \omega^2}{2\pi n V_s c^3 \rho \Gamma_B}, \quad (5.7)$$

where we assume that Stokes and pump wavelengths are equal: $\lambda_{Sj} = \lambda_p = 2\pi c/\omega$. The electrostrictive constant is $\gamma_e = [\rho(\partial\epsilon/\partial\rho)]_S \simeq 0.7$ [136], the fluorite refractive index at $\lambda = 1 \mu\text{m}$ is $n = 1.429$, the density $\rho = 3.18 \text{ g/cm}^3$, and the speed of sound is $V_s = [(C_{11} + C_{12} + 2C_{44})/(2\rho)]^{0.5} = 6.6 \times 10^5 \text{ cm/s}$. It is easy to see that for CaF_2 the value of the bulk Brillouin gain is equal to $g_B = 2.8 \times 10^{-9} \text{ cm/W}$ at $\lambda = 1 \mu\text{m}$, and is two orders of magnitude larger than the bulk Raman gain ($g_r = 2.4 \times 10^{-11} \text{ cm/W}$).

The SBS threshold power for the first Stokes sideband can be computed similarly to the stimulated Raman scattering case [87]:

$$P_{th} = \frac{\pi^2 n^2}{g_b Q_p Q_{S1}} \frac{V}{\lambda_p \lambda_{S1}}. \quad (5.8)$$

Selecting realistic values for a 5 mm cavity, $V = 5 \times 10^{-6} \text{ cm}^3$, $Q_p = Q_{S1} = 10^9$, $\lambda_p = \lambda_{S1} = 1 \mu\text{m}$, one obtains $P_{th} \simeq 3.6 \mu\text{W}$, which is close to the experimentally observed values.

5.2.5 Conclusion

To the best of our knowledge we have for the first time observed a stimulated Brillouin scattering in high-Q whispering-gallery-mode resonators and provided theoretical analysis verifying the experimental results. The observation of doubly resonant SBS in miniature optical WGM resonators opens new possibilities for making ultranarrow-linewidth Brillouin ring lasers for sensitive optical gyros and stable microwave-signal generation. The record-high optical Q factor, mechanical stability, and

robustness of the crystalline WGM resonators make them naturally attractive elements for such application.

Since Brillouin lasing may be detrimental in applications of crystalline WGM resonators other than those involving Brillouin Stokes, a method of suppressing this effect would be valuable. Tailoring the resonator spectrum represents one such technique. A single mode fluorite resonator was fabricated with Q factor approaching 10^9 and diameter of 5 mm. This cavity had an FSR of around 11 GHz and no modes were present at the Brillouin offset. No SBS was observed in this cavity.

Chapter 6

Laser linewidth narrowing with a WGM cavity as a frequency reference

The present section is a work in progress, which has been periodically slowed down by funding issues during the last months of the author's affiliation with JPL. It was stimulated by a requirement of a tunable and stable laser source. The narrow-linewidth laser can be used for spectroscopy and specifically for the precise measurements of ultrahigh Q-factor values in crystalline resonators.

A commercial external cavity diode laser (ECDL), based on a Littman-Metcalf design, was locked to a reference represented by a whispering gallery mode of a fluorite resonator. Phase lock is achieved with a Pound-Drever-Hall (PDH) stabilization technique [137, 138, 139, 138, 140, 141, 142, 143, 144] and linewidth is reduced from around 3 MHz to below 10 kHz.

Widely tunable laser sources with narrow linewidth are important for applications in spectroscopy, metrology, atomic physics, and quantum optics. Diode lasers provide good selection of lasing wavelengths, however the frequency stability and linewidth are generally poor. Stabilizing the diode lasers to an external cavity using an optical feedback provides linewidth on the order of megahertz and tunability over tens of nanometers. Fabri-Perot resonators are typically used as external cavities for laser stabilization. Diode laser linewidth was narrowed to about 10 Hz using the PDH technique [145]. WGM resonators represent another alternative to a Fabri-Perot resonator for laser stabilization. Optical feedback was used to lock a diode laser frequency to a mode of a fused silica microresonator with resulting linewidth of 20 kHz [146]. This is impressive, as the WGM resonator was not thermally stabilized or isolated. Using the optical feedback is not directly applicable to ECDLs. Additional stabilization technique is required to further narrow the linewidth.

Crystalline WGM resonators appear particularly attractive as short-term frequency references. It was shown that crystalline WGM resonators may be used as frequency references providing stability on the order of 10^{-14} over a one second interval [101]. Crystalline resonators are tunable, so a

stabilized diode laser with narrow linewidth and broad tunability may be possible. Mechanical resonances of the WGM cavities are typically in the megahertz range. In contrast to bulky Fabry-Perot resonators, crystalline cavities are compact, fiber compatible, and provide the highest possible optical quality factors. Zero phonon lines in crystals have also been used as absolute frequency references [147]. Combination of crystalline resonators and rare earth ions is of particular interest for single-ion atomic clocks and secondary frequency standards.

Optical resonators made with CaF_2 were used in the experiments presented in this section. Quality factor of the optical modes was $Q \simeq 5 \times 10^8$ and resonator diameter is 5 mm. Angle-polished single mode fiber couplers were used to couple light in and out of the resonator, as shown on Fig. 6.1. The resonator was installed into a holder which provided squeezing and temperature stabilization functionality. The resonator was installed onto a piezo element, and a Peltier element was attached to the holder for active temperature control. Mechanical axial squeezing provided tuning of the eigen frequencies of the resonator over a range of 30 MHz with a voltage of 5 V. A New Focus ECDL Vortex

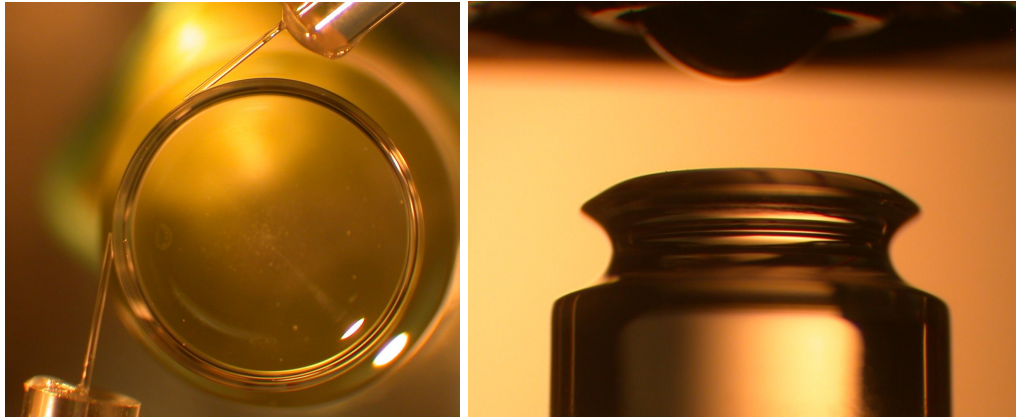


Figure 6.1: Fluorite resonator used as a frequency reference for ECDL laser stabilization

6000 laser was used for phase locking. Laser head model 6017, emitting at 794 nm, was installed onto an optical breadboard with simple vibration isolation. Phase modulation of the laser beam was provided by a resonant electro-optical modulator New Focus EOM 4001, operating at 10 MHz. Optical isolator EOT 780 was also utilized. Setup schematics of Fig. 6.2 are shown. The laser and the resonator were installed on two different tables. Phase modulator is used to place frequency sidebands onto a laser beam. Signal reflected from the resonator contains phase-shifted sidebands, which are detected with a photodetector equipped with a transimpedance amplifier (Fig. 6.3). The electrical signal is multiplied by a phase-shifted copy of the modulation signal in a Minicircuits ZAD-6 mixer. Phase shifting of the modulation signal is achieved by synchronous generation of a phase-shifted copy of the signal with an auxiliary signal generator. The error signal from the mixer is high-pass filtered with a simple RC filter and is conditioned with a servo. Laser frequency is controlled through two channels. One is a slow piezo frequency modulation channel with a response

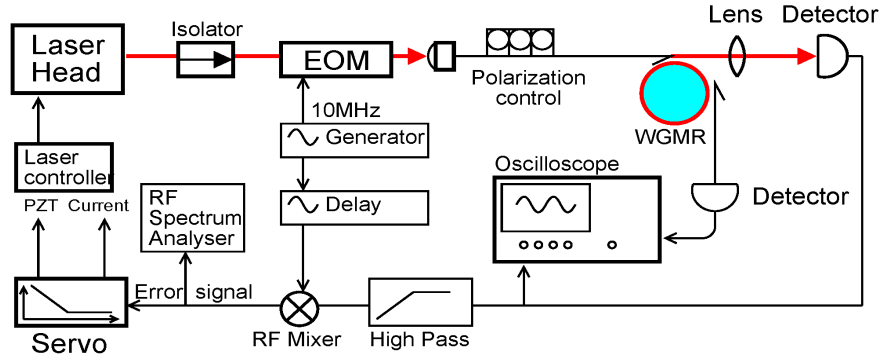


Figure 6.2: Schematics of the optical installation for laser stabilization using a PDH locking technique

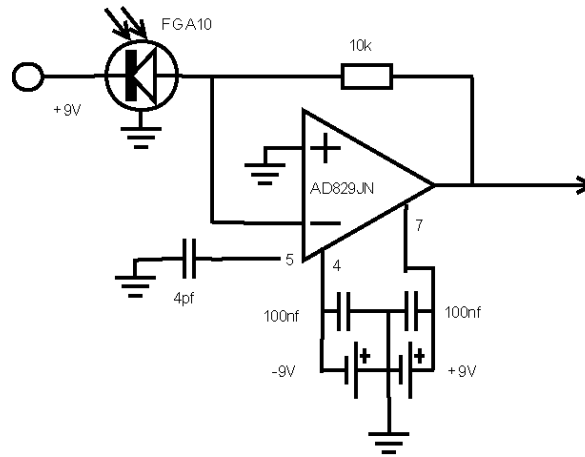


Figure 6.3: Circuit diagram of a “PIN”-type photodetector FGA-10 from Thorlabs in a configuration with a transimpedance amplifier with $10\text{ k}\Omega$ resistor. Peak response is tuned to be close to the modulation frequency of 10 MHz .

of 0.58 MHz/V , and the other is a slow current modulation with a response of 11.4 MHz/V . The servo electronics control these two channels independently, providing a higher gain for a piezo channel with 40 dB per decade slope of the gain to suppress high noises at lower frequencies. The faster current channel has a bandwidth of around 1 MHz and the piezo channel resonance is estimated to be in the 100 Hz range. Consequently, the crossover frequency of the two channel servo loop gain functions is chosen to be around 90 Hz in order to avoid piezo-caused instability in the loop. Servo electronics schematics is shown on Fig. 6.4. It includes two integrators for the piezo channel and two faster integrators for the current channel. The gain of the faster channel is rolled off at frequencies corresponding to the optical cavity roll-off. Usage of slower operational amplifiers for a PZT channel has no special reasons besides lower cost. Faster amplifiers AD829 or similar may be used for all the channels. Locking is achieved by first tuning the laser close to the WGM frequency and switching a

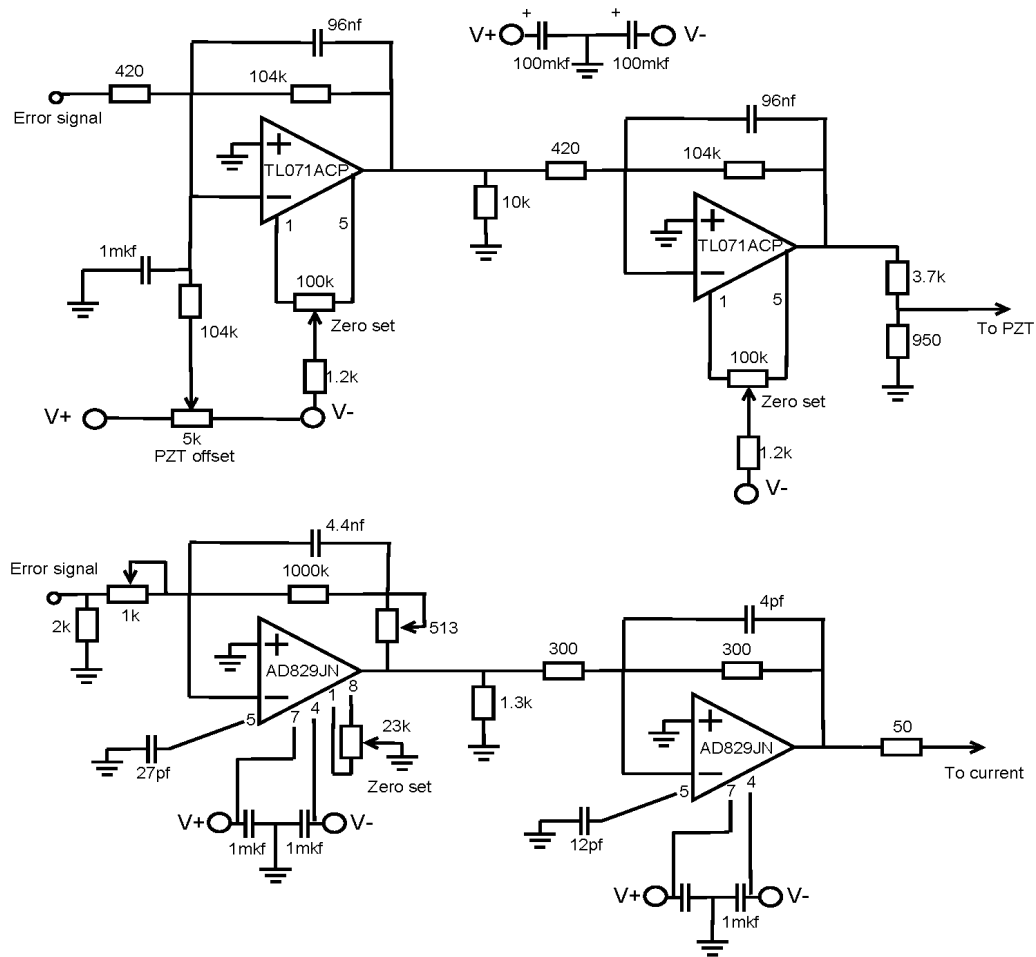


Figure 6.4: Circuit diagram of servo control electronics

fast current gain channel on. This locks the laser to the cavity, once the laser frequency comes close to the WGM frequency. The slower piezo channel is then turned on to compensate for low-frequency noises and drifts. DC voltage offset of current and piezo channels can be adjusted separately. In order to monitor the error signal, a voltage follower circuit capable of driving $50\ \Omega$ loads was added to the schematics shown at Fig. 6.4. The monitoring of the error signal provides a measure of the stability of the closed loop.

Fig. 6.5 is an example of signals observed in laser scan mode and in the locked mode. The upper screenshot is obtained by scanning the laser frequency over a selected WGM frequency. A Lorentzian profile of a cavity mode scanned by a laser which has significant frequency noise is itself noisy, as can be seen on the picture. An optical resonator acts as a low-pass filter for this noise, so cavity transmission has much less noise. Irregularities of the Lorentzian profile are caused by large low-frequency noise. Another example of laser-lock performance is presented in Fig. 6.6. On the left

side of this figure a cavity transmission signal is presented as it was recorded during a short, $60 \mu\text{s}$, time interval. WGM Lorentzian is distorted by a high-frequency laser frequency noise. On the right is the same signal when the servo electronics are keeping the laser locked to a cavity mode. Servo bandwidth was limited by bandwidth of a current modulation channel in a laser controller to about 1 MHz. Noises at higher frequencies could not be efficiently suppressed. A good representation of a lock performance is a spectral density of frequency fluctuations of the laser relative to the cavity mode frequency. The error signal is an electrical representation of this, and can be recalibrated into a relative frequency noise by known value of the cavity discrimination coefficient. For instance, if the error signal is 20 mW peak-to-peak and the cavity mode is 0.5 MHz FWHM, then the coefficient is $D = 0.4 \times 10^{-7} \text{ V/Hz}$. If the error signal spectral density is measured with a 50Ω load in dBm units, the spectral density of relative frequency noise may be obtained as follows:

$$S_f^2 = \frac{50 \cdot 10^{-3} \cdot 10^{\left(\frac{P_{dBm}}{10}\right)}}{D^2 \cdot Bw}, \quad (6.1)$$

where Bw denotes electronic spectrum analyzer bandwidth, and P_{dBm} is a power spectral density in dBm units. This equation was used to derive the frequency spectrum shown on Fig. 6.7. In case of a tight servo lock, laser linewidth is given by a simple expression: πS_f^2 , which for our spectrum corresponds to 10 kHz. The peak around 3 MHz on Fig. 6.7 is explained by relaxation oscillations inside a laser diode. This is a work in progress and further improvements may be done. Noises could be suppressed with proper filtration and servo gain function could be improved. Linewidth below 1 kHz should be achievable. If a servo loop is implemented to directly control laser head transducers (piezo and fast current modulation) better results could be achieved, as laser control electronics would not introduce unknown transfer functions. The phase-modulation frequency should be chosen to be well outside the laser noise sidebands, and the error signal should be band-pass filtered before the mixer.

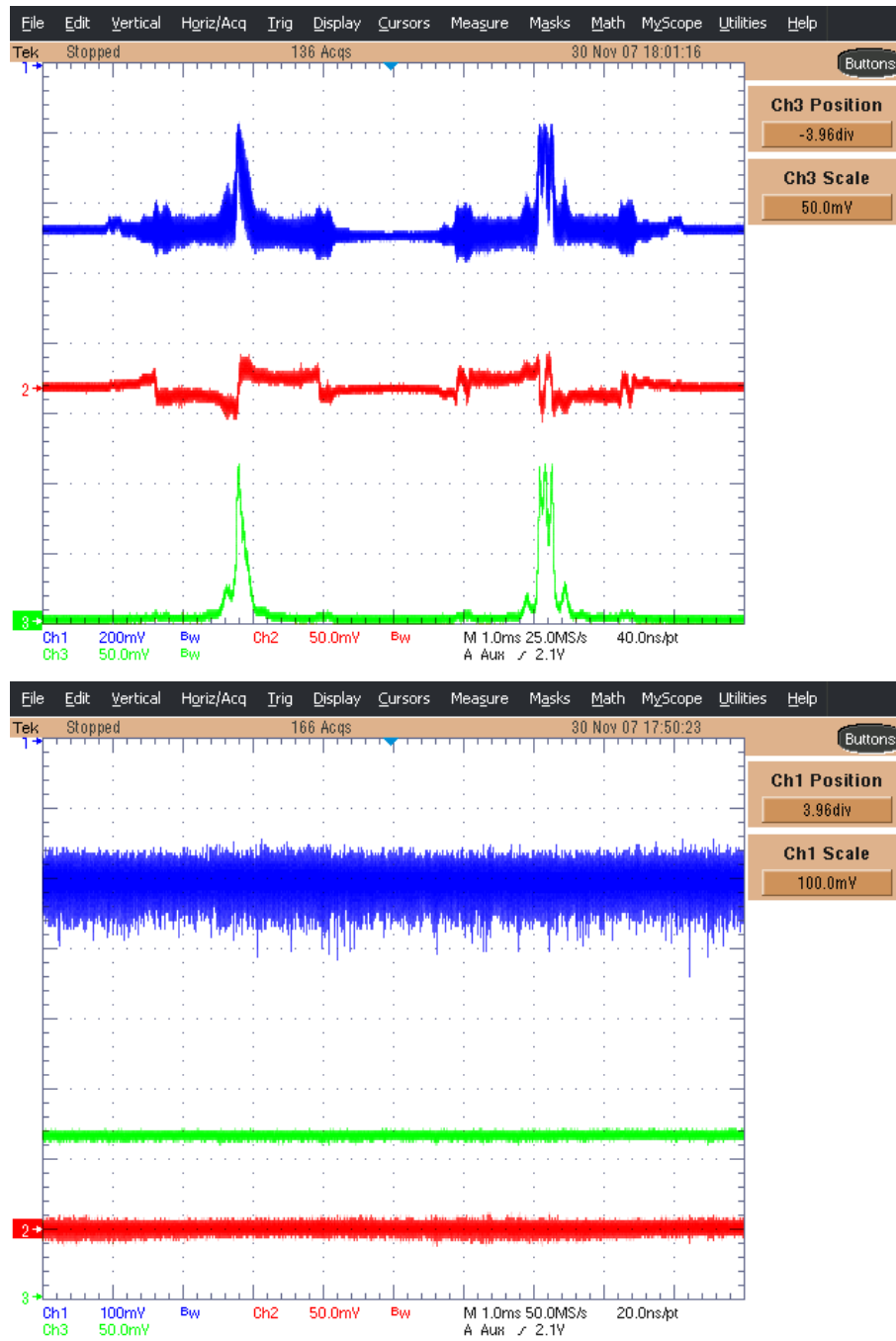


Figure 6.5: Upper panel: signals obtained from the photodetectors measuring reflection and transmission of the optical resonators along with an error signal. Signals from top to bottom: cavity reflection, error signal, cavity transmission. Right panel: signals in a locked state. Signals from top to bottom: cavity reflection, cavity transmission, error signal. Note reduced amplitude noise in cavity transmission signal, as the resonator acts as a low-pass filter.

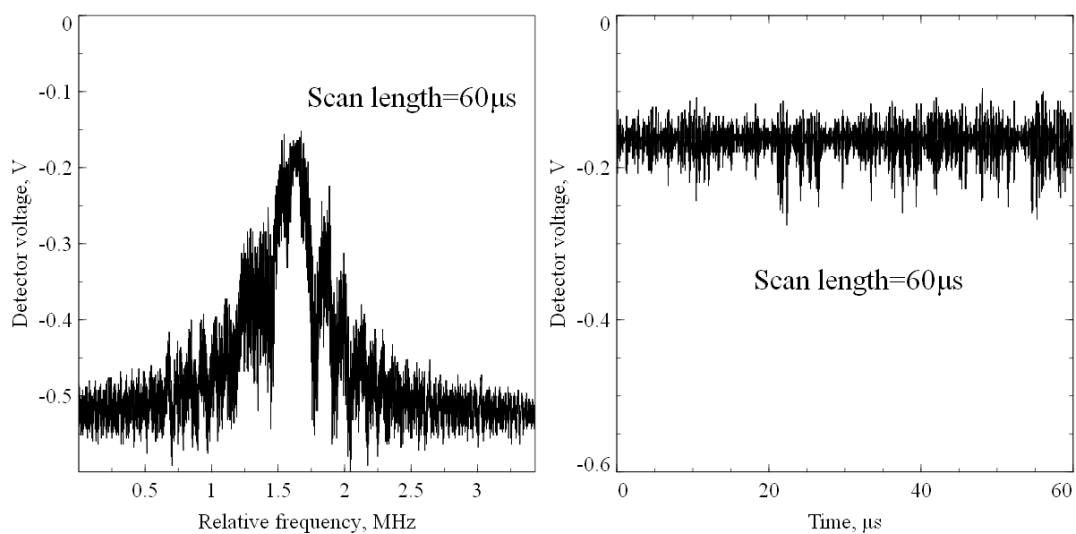


Figure 6.6: Scan of a WGM as a cavity transmission signal, where laser's frequency noise is detected by a cavity. On the right is the record of the same signal in a locked regime. Noise ripples are at frequencies above 0.8 MHz, where the servo is not efficient enough.

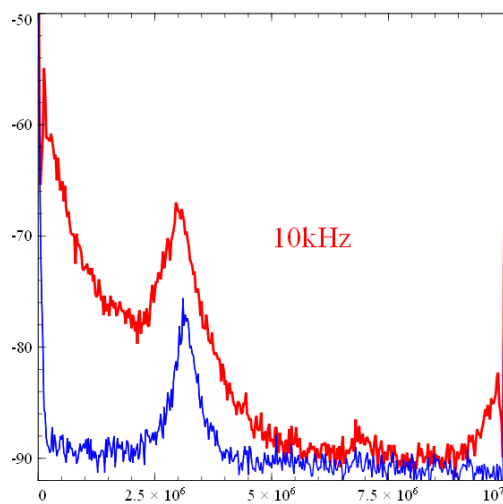


Figure 6.7: Power spectral density of relative frequency noise in dBm units. This spectrum shows how much the laser frequency deviates from the cavity mode frequency. Recalibration leads to a linewidth of better than 10 kHz (corresponding to a horizontal line at -60 dBm level). The lower spectrum represents electronic noise when the laser is not locked to the WGM.

Chapter 7

Cryogenic apparatus

Prospects of interesting experimental results, such as ultrahigh optical Q factor and single-ion spectroscopy in crystalline resonators prompted development of a cryogenic setup. The major requirement was the operation of WGM resonators at cryogenic temperatures, which included optical input and output, along with reliable coupling. The challenges included the small, 4 inch inner diameter of the available cryostat, which was used for He₃ research some 20 years ago. The insert included a 1 K liquid helium evaporative cooling pot, with another lower temperature stage installed on it. Most of the insert had to be removed or modified. An additional hurdle was the huge amount of time spent on fixing numerous leaks in the insert, which arose from the notable age of the device. Nevertheless, most of the problems were solved and the WGMs were observed at the temperature of 77 K. The cryostat included a 5-foot-high superinsulated evacuated helium dewar with 4 inch inner diameter and 11 liters volume (Fig. 7.1). The vacuum chamber of a cryostat insert is a copper cylinder on

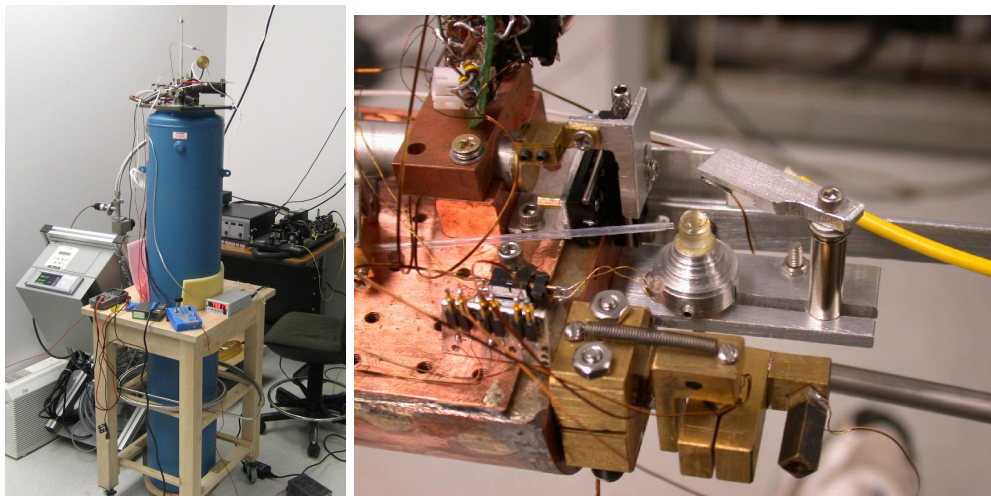


Figure 7.1: Left: helium dewar with a pump and a laser. Right: optical setup of the insert. Copper 1 K pot, resonator, optical fibers, and the cryogenic nanopositioner are visible.

brass flanges with indium sealing. The chamber is 1.8 liters in volume. Optical input was provided

through a single mode fiber glued into the insert. Multimode 1 mm fused silica fiber was used as an output optical window. The 1 K pot served as a frame to the sides of which other parts were attached. These included the post for holding the WGM resonator, a three-axis nanopositioner used for moving the angle-polished fiber coupler, a web camera, a thermometer, and a light source.

One of the most critical parts of the setup is a positioner used for coupling. The optical fiber tip must be put within 50 nm of the resonator surface and its position must be controllable to about 10 nm. The positioner must have a footprint of less than one inch and a range of motion of about a millimeter at cryogenic temperatures. The only technology capable of meeting all these requirements is a stick-slip positioning. Commercial devices are rather costly (\$20 thousand) so an alternative was built, which utilized the same principle (see Fig. 7.2). The positioner has three stages for the X,Y,Z directions, 3 millimeter motion range, and can be controlled in either stepper mode or in continuous scanning mode. The amplified oscillator circuit was built to provide a high-current sawtooth-shaped signal to the piezo elements of the positioner. Slow expansion followed by a rapid contraction leads to a slipping action resulting in a single step. Continuous variation of voltage applied to a PZT element leads to a smooth position shift. A regular web camera was equipped with a set of resistors glued to

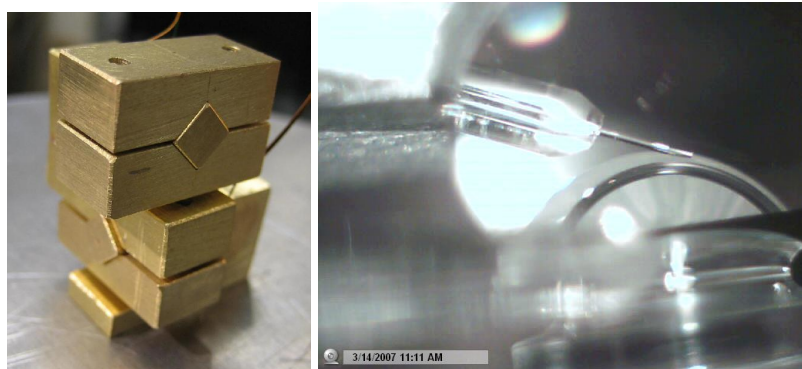


Figure 7.2: Prototype of a stick-slip nanopositioner on the left. Crystalline resonator and a coupler as seen through a web camera on the right.

the circuit board. These were used for heating and for temperature sensing. The camera could be heated inside the insert, which made its operation possible in a cryogenic environment. Heating of a camera to 270 K in a cryogenic environment leads to radiative dissipation of only around 1 W of heat. Since operation of a camera is only required for coupler adjustment, this heat did not interfere with measurements (Fig. 7.2).

Unfortunately, in addition to many other leaks, a cold leak was found. This leak only revealed itself when the dewar was filled with liquid nitrogen and could not be located with a helium leak detector. This and other problems at JPL made it impossible to continue this experiment.

Chapter 8

Applications of optical resonators

8.1 Bessel beam generation

The author of this dissertation was given an opportunity to perform the first experiment on generation of truncated Bessel beams with the fused silica devices. Full account of the work is given in paper [8], of which this section is a partial reproduction. Material reproduced with permission from OSA.

8.1.1 Introduction

We demonstrate a method of generating the beams of light with large angular momenta. The method utilizes whispering-gallery-mode resonators that transform a plane electromagnetic wave into high-order Bessel beams of a silica waveguide. Interference pattern among the beams as well as shadow pictures induced by the beams are observed and studied.

Optical vortices or light beams with nonzero angular momenta are interesting not only because of their underlying physics, but also because of potential applications. Generation of such vortices and the study of their properties has recently attracted considerable attention. The beams have been realized with both passive and active schemes (see [148, 149, 150, 151] for review). Generation of beams with orbital angular momentum exceeding $10^4 \hbar$ per photon is possible [152] but is not easily achievable experimentally. To our knowledge, the highest orbital angular momenta of photons observed so far are approximately $25 \hbar$ [152] and $30 \hbar$ [153]. Beams with angular momenta of up to $300 \hbar$ were recently demonstrated [154]. In this paper we discuss another method for generation of photons with large orbital momentum. We report on a proof-of-principle experiment validating the application of a low-contrast whispering-gallery-mode (WGM) resonator that supports modes with high angular momenta for the generation of high-order Bessel beams [155]. By “low contrast” we mean a new design whereby the resonator is a part of the waveguide, but has a slightly larger radius than the waveguide. The resonator can be made by cutting and polishing a bump pattern

on the waveguide surface. Such a resonator has an important distinction from the ordinary WGM resonators since its modes decay primarily into the Bessel modes of the waveguide, and not to the outside environment. By changing the resonator shape and the radius of the waveguide it is possible to change the resonator loading and to allow light propagation from the resonator to the waveguide. Free-space propagation distance of the beams with angular momenta defines the

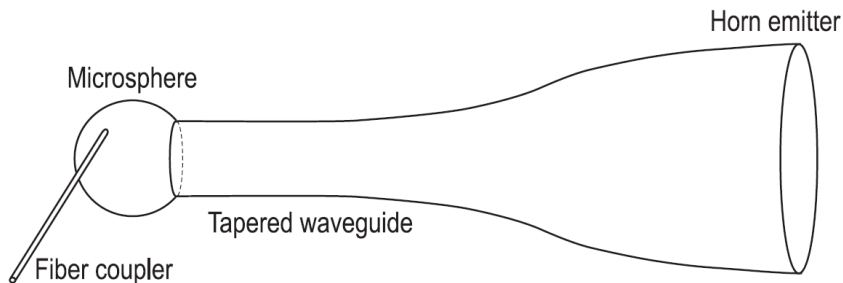


Figure 8.1: Schematics of the device used to generate Bessel beams

feasibility of practical applications. A high-order Bessel wave that penetrates into a cylindrical waveguide from the resonator through evanescent field coupling cannot leave the waveguide. It runs until the end of the waveguide and reflects, because of the total internal reflection. It is possible to manipulate the wave inside the waveguide. However, the complete confinement of the waves in the waveguide reduces the spectrum of their applications. We used a cleaved waveguide to release the Bessel beam into free space. We have been able to generate Bessel beams with orders exceeding a thousand, and have studied interference of multiple beams with different angular momenta as well as pictures of the shadow of an object placed in front of them. The shadow has properties that arise from the far-field interference of the beams of different orders at different points at the exit of the waveguide. This interference experiment allowed us to estimate the propagation distance of the optical vortices. The distance drastically decreases with an increase of the value of the angular momentum.

The experiments with shadows have shown that a shadow of a straight rod illuminated with a Bessel beam is not a straight line. This result may be explained theoretically in the frame of geometrical, not wave, optics [8].

8.1.2 Experimental generation of truncated Bessel beams

We fabricated several low-contrast fused-silica WGM resonators as integral parts of tapered waveguides (Fig. 8.1). In one experiment, a segment of a fused-silica multimode fiber rod is cleaved and the cleavage plane is polished. The diameter of the fiber is 1 mm. The other end of the rod is

stretched into a conical shape in a hydrogen burner. This end is fused to form a WGM resonator about $300\ \mu\text{m}$ in diameter as an integral part of a cone. This cone starts at the WGM resonator at a diameter of about $250\text{--}280\ \mu\text{m}$ and expands to $1\ \text{mm}$ in diameter over $1\ \text{cm}$ distance (Fig. 8.2). Another resonator we made has a $500\ \mu\text{m}$ diameter, and the taper diameter changes from $450\ \mu\text{m}$

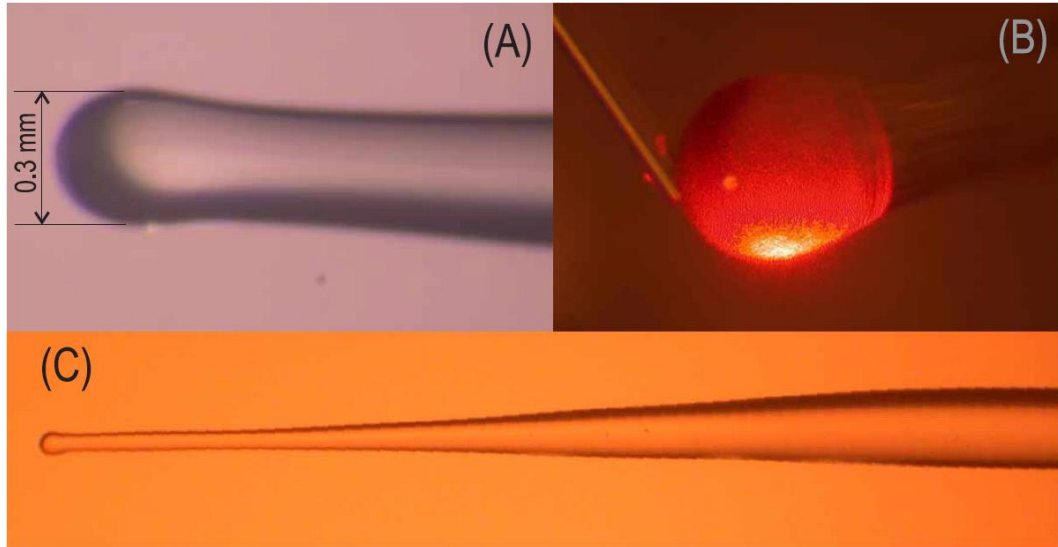


Figure 8.2: A low-contrast whispering gallery mode resonator for Bessel beam generation. The resonator is created by the local increase of the waveguide radius. A tapered waveguide is used to generate a Bessel beam in the free space. Increasing the waveguide radius changes the wave vector of the light, guaranteeing escape of the light from the waveguide into the free space. (A) A low-contrast fused silica WGM resonator attached to the tapered waveguide. (B) Coupling light into the WGMs of the resonator using cleaved fiber. (C) Tapered fiber used to release generated Bessel beam into free space

to $3\ \text{mm}$ over a $3\ \text{cm}$ distance. The resonators were optically pumped with $650\ \text{nm}$ light using an angle-polished fiber coupler. We excited a family of WGMs that interacted with the modes of the tapered fiber. The fiber coupler is shown in Fig. 8.2(b). It is easy to see the glow on the resonator surface resulting from the scattering of the light in the WGMs, which abruptly disappears in the vicinity of the coupling point between the resonator and the tapered fiber. This glow shows the geometric localization of light in the resonator. As the WGMs of the resonator decay into the fiber, light propagates and exits the fiber into the free space as truncated Bessel beams. Because the ratio of the taper entrance over the exit diameters was small ($r_{exit}/r_{entrance} = 6$ or less) and the mode order was high ($> 10^3$), the propagation distance of Bessel beams in free space did not exceed ten millimeters. The beams spread out creating peculiar interference shapes in the far-field region (Fig. 8.3(a)). This observation has a certain similarity with the interference pattern of zero- and first-order Laguerre-Gauss beams presented in [156]. The interference pattern in Fig. 8.3 could be explained if we consider the interference of multiple radially truncated high-order Bessel waves with nearly the same diameter but different angular momenta. Light from an angle-polished fiber coupler

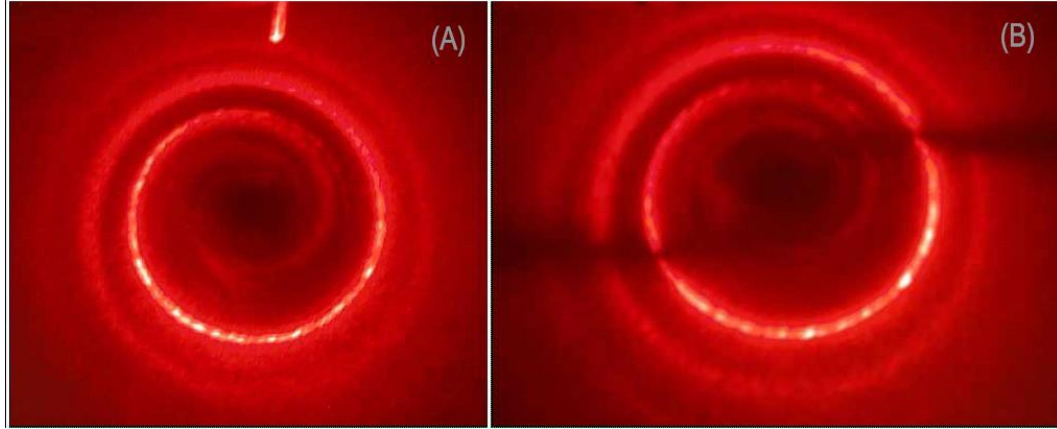


Figure 8.3: (A) Far-field interference pattern of multiple co-propagating Bessel beams. (B) Far-field shadow of a 250-micrometers-thick needle placed in the path of the beam emerging from the fiber taper.

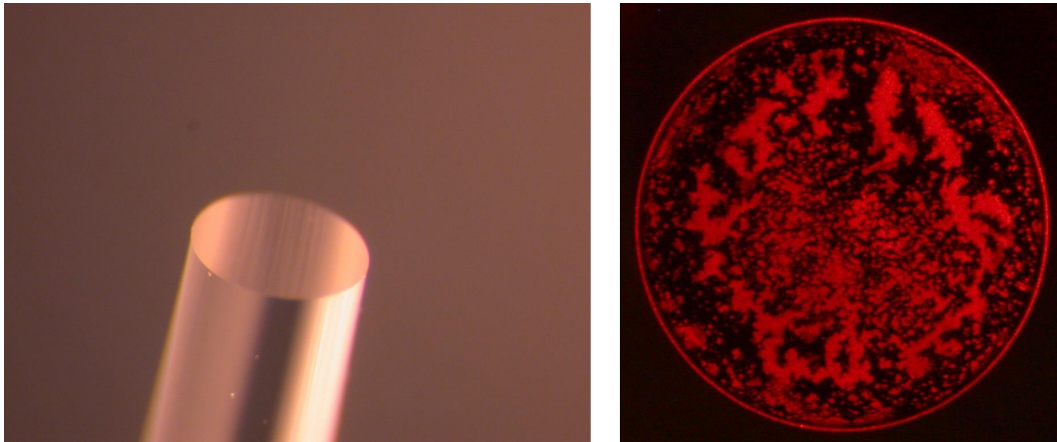


Figure 8.4: (A) Close-up view of the fused silica waveguide output. (B) Carbon powder was applied to the end of the waveguide and covered most of the surface. The red ring corresponds to the localization of Bessel beam energy inside of the waveguide.

(Fig. 8.2(b)) excites many modes of the resonator with different quantum numbers and the same frequency. These WGMs excite the Bessel waves in the tapered waveguide. The waves have different propagation constants along the Z axis and, hence, different dispersion. The initially narrow angular distribution of light in the taper broadens up with the propagation distance and forms the spiral pattern.

Aside from the interference, we have observed peculiar shapes of the shadow of a straight, thin, needle. This needle was $250\ \mu\text{m}$ thick and was set parallel to the waveguide surface so that it crossed the symmetry axis of the beam with large angular momentum (Fig. 8.3(b)). The shadow is orthogonal to the needle in the center of the interference pattern, and is parallel, but displaced, away from the center. The shape of the shadow depends on the distance of the object from the surface of the taper. The closer the wire is, the longer is the region of the orthogonal shadow. We have

repeated the same experiment using a 532 nm laser and a 25- μm -thick piece of a tungsten wire, and obtained similar result. Images and video in the paper elucidate this explanation and suggest that the twisting of the shadow is a consequence of the beam's angular momentum.

8.1.3 Conclusion

We have demonstrated the generation of optical beams with angular momentum exceeding a thousand using fused-silica whispering-gallery-mode resonators. The beams propagate more than a centimeter in the free space. Exactly the same approach would allow efficient generation of Bessel beams with momenta exceeding 10^5 . Interference patterns of the multiple beams, as well as the peculiar shadow pictures created with the beams, are demonstrated experimentally and explained theoretically.

8.2 Enhanced photothermal displacement spectroscopy

This section is based on a study — “Enhanced photothermal displacement spectroscopy for thin-film characterization using a Fabry-Perot resonator” — published in the *Journal of Applied Physics* [12] and also attached below with permission from AIP. Prior to joining the JPL group, the author participated in a project aimed at measuring thermal properties of thin optical coatings. These properties define thermal noise caused by the surface of heavy mirrors of LIGO interferometers.

From thermal expansion of mirror surface caused by minute absorption of light pulse it is possible to derive thermal expansion and temperature conductivity coefficients for the material. The expansion is measured with an interferometric technique where a Fabry-Perot cavity is used to boost the pulse power and to enhance sensitivity to the surface expansion of the mirror. If a thin coating is present on the mirror, it is possible to measure thermal properties of only the coating material by applying high-frequency optical pulses to the surface. If the frequency is high enough, only the coating is contributing to thermal expansion. The main result of this work is the upgrade of the previous technique, which made it possible to perform measurements at significantly higher frequencies and probe the properties of thin coatings. An opto-mechanical beam chopper was replaced with an electro-optical amplitude modulator and the experimental procedure was automated. This allowed us to perform measurements at frequencies of up to 1 MHz, as compared to the previous limitation of a few kilohertz.

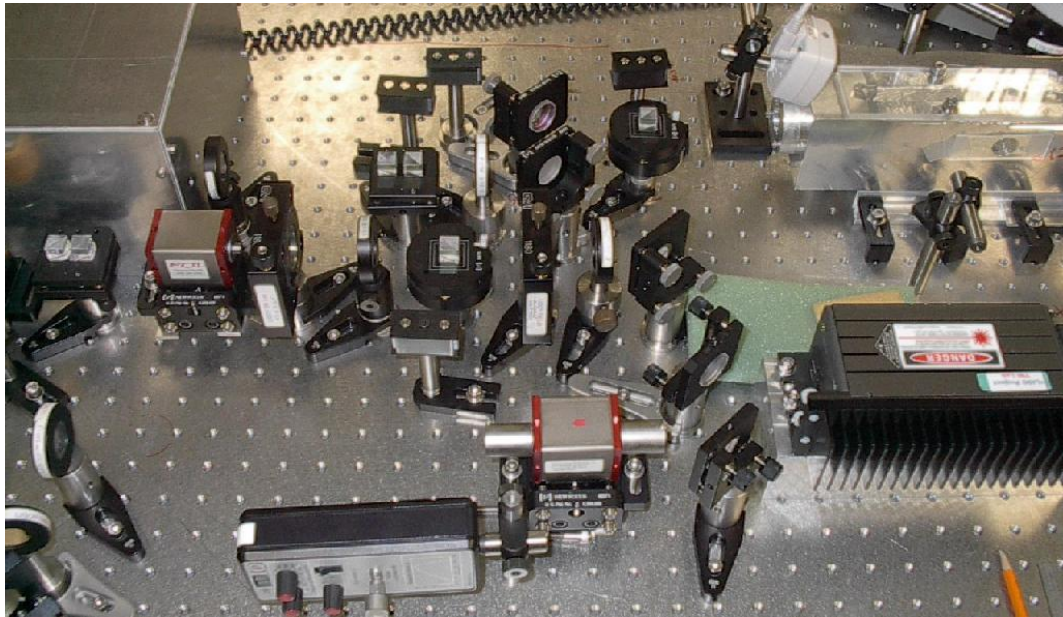


Figure 8.5: Optical setup was initially built by Shanti Rao, part of which is shown here. It was subsequently upgraded by the author.

Enhanced photothermal displacement spectroscopy for thin-film characterization using a Fabry-Perot resonator

Eric D. Black, Ivan S. Grudinin, Shanti R. Rao, and Kenneth G. Libbrecht
LIGO Project, California Institute of Technology, Mail Code 264-33, Pasadena, California 91125

(Received 23 October 2003; accepted 5 March 2004)

We have developed a technique for photothermal displacement spectroscopy that is potentially orders of magnitude more sensitive than conventional methods. We use a single Fabry-Perot resonator to enhance both the intensity of the pump beam and the sensitivity of the probe beam. The result is an enhancement of the response of the instrument by a factor proportional to the square of the finesse of the cavity over conventional interferometric measurements. In this paper we present a description of the technique, and we discuss how the properties of thin films can be deduced from the photothermal response. As an example of the technique, we report a measurement of the thermal properties of a multilayer dielectric mirror similar to those used in interferometric gravitational wave detectors. © 2004 American Institute of Physics. [DOI: 10.1063/1.1728312]

I. INTRODUCTION

Recently there has been much interest in understanding noise mechanisms in dielectric coatings of mirrors used in advanced interferometric gravitational wave detectors.^{1–8} One noise mechanism that could potentially limit the sensitivity, and hence the astrophysical reach, of an advanced detector is coating thermoelastic-damping noise.^{1,2,9,10} In order to accurately predict the level of this noise and to design coatings in which this noise source is minimized, we need to have accurate values for the thermal properties of the thin films that make up these dielectric coatings. Specifically, we need to know the thermal expansion coefficient α and the thermal conductivity κ of the coating materials in thin-film form.

It is well known that the thermal conductivities of materials in thin films can differ markedly from those of the same materials in bulk form,^{11–15} and there is evidence of a similar deviation in the thermal expansion coefficient.^{16–18} Thus, there is a need to directly measure the thermal properties of candidate coatings in order to select ones that exhibit the lowest thermoelastic-damping noise.

We have constructed an apparatus to characterize dielectric coatings on mirrors for the purpose of selecting the best coating for an advanced interferometric gravitational wave detector. We use interferometric photothermal displacement spectroscopy, a technique well suited for measuring the thermal conductivity and expansion coefficient of a thin film,^{19–24} but our method differs from conventional photothermal-displacement-spectroscopy techniques in one important point. We use a Fabry-Perot cavity to substantially enhance both the pump-beam heating power applied to the sample and the sensitivity of the probe beam.

In this paper we both describe the apparatus and discuss a simple and intuitive way of looking at the physics of the photothermal response over a broad range of frequencies.

II. THE INSTRUMENT

Traditional interferometric photothermal displacement spectroscopy uses separate pump and probe beams, some-

times with different wavelengths, to locally heat a sample and measure the resulting thermal expansion. One widely used configuration uses the sample as the end mirror in one arm of a Michelson interferometer (see, for example, Ref. 19). DeRosa *et al.*²⁵ have observed the differential photothermal response in a pair of Fabry-Perot cavities, in a configuration originally conceived as an optical readout for a resonant-bar gravitational-wave detector. Their experiment nicely demonstrated the photothermal effect in Fabry-Perot cavities, verifying the theory of Cerdonio *et al.*¹⁰ for the frequency-dependent photothermal response of a homogeneous material.

There is currently a need to characterize the thin-film dielectric coatings that are expected to be used in advanced interferometric gravitational wave detectors. We have the need to measure both the thermal expansion coefficient and thermal conductivity of such coatings, and so we have constructed an instrument based on interferometric photothermal displacement spectroscopy to perform such measurements on candidate coatings. Our apparatus uses a single Fabry-Perot cavity, as shown in Fig. 1, with the sample forming one of the mirrors in the cavity.^{26,27}

Figure 1 shows a diagram of our experimental apparatus. Both the pump and probe beams are provided by the same laser, so that both can resonate simultaneously inside the cavity. The pump and probe beams are distinguished from each other by having orthogonal polarizations. The first half-wave plate after the laser adjusts the polarization, determining how much goes into the pump or probe paths via a polarizing beam splitter. We phase modulate the probe beam using an electro-optic modulator (EOM) and lock it (and by extension the pump beam) to the cavity by the use of the Pound-Drever-Hall method.^{28,29} We amplitude modulate the pump beam using an acousto-optic modulator (AOM) and use lock-in detection to measure the photothermal response from the error signal.

For a pump beam sinusoidally modulated at a frequency f that is much higher than the unity-gain frequency of the servo, the error signal is given by

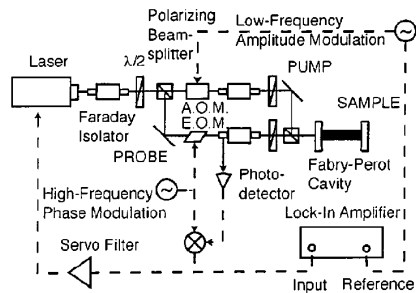


FIG. 1. A diagram of our experimental apparatus. We use a polarizing beam splitter to separate the horizontally and vertically polarized components of a laser beam into pump and probe beams, respectively, both of which resonate simultaneously in the Fabry-Perot cavity. We then phase modulate the probe beam, via an electro-optic modulator (EOM), and use it to measure the length of the cavity. The pump beam is amplitude modulated, using an acousto-optic modulator (AOM), and this periodically heats the back (absorbing) mirror in the cavity to generate the photothermal displacement. A half-wave plate ($\lambda/2$) allows us to tune the polarization of the beam before the beam splitter and thus to adjust the relative power in the probe and pump beams.

$$\varepsilon = -8RP_{probe} \frac{LF}{\lambda} J_0(\beta) J_1(\beta) \left\{ \frac{\delta L}{L} \sin 2\pi ft \right\},$$

where R is the (rf) response of the photodiode, P_{probe} is the power in the probe beam, L and \mathcal{F} are the length and finesse of the Fabry-Perot cavity, λ is the wavelength of the laser light used, β is the phase modulation depth (in radians), and $\delta L \sin(2\pi ft)$ is the deviation in L from the ideal resonance condition $2L = N\lambda$. J_0 and J_1 denote Bessel functions of order 0 and 1.

Thus the signal we are measuring is proportional to $(\mathcal{F}\delta L/\lambda)$, as opposed to simply $(\delta L/\lambda)$ for the conventional Michelson interferometer. The finesse \mathcal{F} of the cavity, and hence the enhancement to the sensitivity to the photothermal displacement δL , can, in principle, be made quite large, with values of $\mathcal{F} = 10^5$ achievable with standard techniques.

In addition to enhancing the sensitivity to a given photothermal displacement δL , the Fabry-Perot cavity also enhances the displacement itself. If P_{pump} is the power in the pump beam, incident on the cavity, then the power incident on the sample inside the cavity is approximately $P_{inc} \approx \mathcal{F}P_{pump}$. As we shall see below, the photothermal response δL is proportional to the total power absorbed by the sample, which in turn is proportional to P_{inc} . Thus the Fabry-Perot cavity enhances the signal measured at the lock-in amplifier by a factor of \mathcal{F}^2 .

This enhancement of the signal over conventional methods opens up many possibilities for photothermal measurements. For example, it should be possible to measure the thermal properties of very-low-absorption samples that would otherwise be inaccessible to photothermal techniques.

The sensitivity of this method is, in practice, limited by two things. First, it is limited by a combination of noise in the cavity length and laser-frequency noise. Intrinsic cavity length noise is thermal in origin and is typically small enough to be negligible for photothermal experiments except at the mechanical resonant frequencies of the cavity itself.³⁰

Extrinsic noise in the cavity can be suppressed by suitable isolation methods, including suspension from seismic isolation platforms and enclosure in a vacuum apparatus.

A solid-state Nd:YAG (YAG—yttrium aluminum garnet) laser, such as the Lightwave 126 (Ref. 31), typically has a frequency noise of $\delta\nu(f) \approx 100 \text{ Hz}/\sqrt{\text{Hz}} \times (100 \text{ Hz}/f)$, where f is the measurement frequency.³² For a 30 cm cavity, this corresponds to an equivalent length noise of

$$\delta L_{eq-freq}(f) = \frac{L\lambda}{c} \delta\nu(f) \approx 1 \times 10^{-13} \frac{\text{m}}{\sqrt{\text{Hz}}} \left[\frac{100 \text{ Hz}}{f} \right] \times \left(\frac{L}{30 \text{ cm}} \right) \left(\frac{\lambda}{1.064 \mu\text{m}} \right).$$

The fundamental shot noise limit for measuring the length of the cavity is much lower and, well below the cavity pole, is²⁹ given by

$$\delta L_{eq-shot} = \frac{\sqrt{\hbar c}}{8} \frac{\sqrt{\lambda}}{\sqrt{P_{probe}}} \approx 8.1 \times 10^{-19} \frac{\text{m}}{\sqrt{\text{Hz}}} \left(\frac{100}{\mathcal{F}} \right) \times \left(\frac{\lambda}{1.064 \mu\text{m}} \right)^{1/2} \left(\frac{500 \text{ mW}}{P_{probe}} \right)^{1/2}.$$

Second, the sensitivity is limited by the degree to which the pump and probe beams can be made orthogonal and therefore isolated from each other. For the photothermal signals we have observed that we have had no difficulty in reducing this pump-probe cross-coupling noise to much less than the amplitude of our signal, even at the highest modulation frequencies and lowest signal levels.

III. THE PHOTOTHERMAL RESPONSE

A rigorous modeling of the photothermal response requires a complete, multidimensional solution to the diffusion equation to solve for the temperature distribution inside the sample, and then a solution to the Navier-Stokes equations to solve for the resulting thermal expansion. This has been done in a variety of contexts,^{33–37} but the form of the solutions is somewhat involved, and fitting them to experimental data to extract a sample's thermal properties, especially those of a sample that includes a thin, inhomogeneous surface layer, is computationally intensive.

We may gain considerable insight into the relationship between the photothermal response and thermal properties of a sample by making a simple estimate of the frequency dependence and magnitude of the photothermal response. If we apply a sinusoidal heat source to the surface of a material, thermal waves will propagate into the material, with a resulting sinusoidal thermal expansion over the volume being heated. A very general property of thermal waves is that they decay away as they propagate, with a characteristic decay length that is equal to the wavelength of the thermal wave. In this sense, they behave very much like electromagnetic waves propagating into a normal conductor.³⁸ For a homogeneous material with thermal conductivity κ , mass density ρ , and specific heat C , this penetration depth ℓ_t is given by

$$\ell_t(f) = \sqrt{\frac{\kappa}{\rho C} \frac{1}{\pi f}}$$

Thus we may assume, for a rough approximation, that the material only gets heated to a depth of ℓ_t . The thermal expansion of this part of the material is given, again approximately, by

$$\delta L = \ell_t \alpha \Delta T.$$

Let us consider a sinusoidally modulated pump beam with a power given by

$$P_{pump} = P_0 + P_m \frac{\sin(2\pi ft)}{2},$$

where P_m is the peak-to-peak modulated power in the pump beam. (For 100% modulation, $P_0 = P_m/2$, where P_m is the total amplitude of the pump beam.) If $P_{abs} = WP_m$ is the (peak-to-peak) power absorbed at the surface of the sample (W being the absorption coefficient), then the total temperature change ΔT over a single cycle is $\Delta T = (P_{abs}/2f)/(\rho CV)$, where V is the volume of the material getting heated.

For high frequencies, where $\ell_t \ll r_0$ and r_0 is the radius of the laser spot doing the heating, we can approximate the volume by⁹

$$V \sim \pi r_0^2 \ell_t,$$

which gives an approximate photothermal response

$$\delta L_{hi-f}(f) \sim P_{abs} \frac{\alpha}{\rho C} \frac{1}{r_0^2 f}$$

or

$$\delta L_{hi-f}(f) \sim P_{abs} \frac{\alpha f_s}{\kappa f}, \quad (1)$$

where the characteristic frequency for this homogeneous substrate is defined as

$$f_s \equiv \frac{\kappa}{\pi \rho C r_0^2}. \quad (2)$$

The high-frequency photothermal response is proportional to $1/f$, and its magnitude gives us the thermal expansion coefficient α , provided we know P_{abs} , ρ , and C (or it can give P_{abs} if we know α , ρ , and C , etc.).

For low frequencies, we approximate the volume¹⁰ by

$$V \sim \frac{1}{2} \left(\frac{4}{3} \pi \ell_t^3 \right),$$

which gives a photothermal response of

$$\delta L_{low-f}(f) \sim P_{abs} \frac{\alpha}{\kappa}. \quad (3)$$

Note that the low-frequency response is essentially independent of frequency, with a natural “turning point” between the low- and high-frequency regimes at the crossover frequency f_s . This turning point does not depend on P_{abs} or α , is determined by the length scale r_0 , and can be used to get the thermal conductivity κ , provided we know r_0 and ρC .

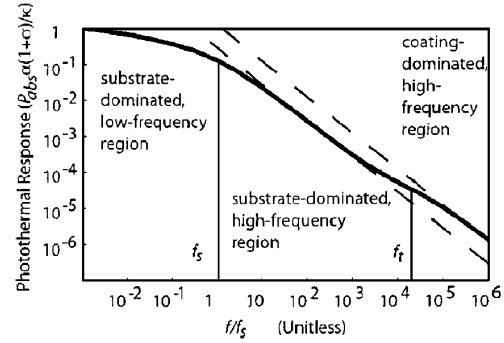


FIG. 2. The expected photothermal response of a coated sample. When the coating thickness is much less than the laser spot radius, there are three clearly defined frequency regimes. The magnitude of the photothermal response in each regime and the transition frequencies between regimes together allow us to determine the thermal properties of the sample.

A careful derivation gives the complete response, valid for a homogeneous material at all frequencies,^{10,25} as

$$\delta L(f) = \left(\frac{P_{abs}}{2} \right) \frac{1}{\pi} \frac{\alpha(1+\sigma)}{\kappa} \times \left| \frac{1}{\pi} \int_0^{\infty} du \int_{-\infty}^{+\infty} dv \frac{u^2 e^{-u^2/2}}{(u^2+v^2)(u^2+v^2+i2f/f_s)} \right|, \quad (4)$$

where σ denotes Poisson's ratio.

For a material with a coating, there is an additional length scale, the coating thickness t . At sufficiently high frequencies the thermal penetration depth ℓ_t becomes less than t , and the thermal waves essentially only sample the coating. When this happens, the photothermal response will be dominated by the coating and we have, approximately,

$$\delta L_{f \gg f_t}(f) \sim P_{abs} \frac{\alpha_c f_c}{\kappa_c f},$$

where the subscript c denotes a coating property. The transition frequency that defines this regime occurs where $\ell_t = t$, or

$$f_t \equiv \frac{\kappa_c}{\pi \rho_c C_c t^2}, \quad (5)$$

and the coating characteristic frequency is

$$f_c \equiv \frac{\kappa_c}{\pi \rho_c C_c r_0^2}. \quad (6)$$

At low frequencies, where $\ell_t \gg t$, the volume of the sample that gets heated and expands is predominantly substrate, with the coating contributing very little to the overall photothermal response. In this regime we expect the net response of the coated sample to be essentially indistinguishable from that of an uncoated sample.

If $t \ll r_0$ there will be two high-frequency regimes, as shown in Fig. 2: one at moderately-high frequencies in which $t \ll \ell_t \ll r_0$, where the photothermal response has a $1/f$ frequency response and is dominated by the substrate, and

another at higher frequencies where $\ell_t \ll l \ll r_0$. In this highest-frequency regime, the frequency dependence is again $1/f$, but the photothermal response is now dominated by the coating. The crossover frequency between these two regimes occurs where $\ell_t = l$, or $f = f_t$.

We may interpolate between these two high-frequency regimes to obtain an approximate, high-frequency photothermal response of a coated sample:

$$\delta L(f) \approx \frac{P_{abs}}{4\pi^2} \left[\left(\frac{\alpha(1+\sigma)}{\kappa} \right) \frac{f_s}{f} + \left(\frac{\alpha_c(1+\sigma_c)}{\kappa_c} \right) \frac{f_c}{f_t+f} \right]. \quad (7)$$

This is the formula we will use to fit our high-frequency data to extract the coating thermal properties.

IV. RESULTS

We measured the photothermal response of two samples. The first was single-crystal, synthetic, *c*-axis sapphire. The second was identical to the first except for the addition of a 4 μm multilayer dielectric coating of alternating layers of SiO_2 and TiO_2 . This coating formed a high-reflectivity mirror for infrared light with a wavelength of 1.064 μm .²⁷ Both samples, including the dielectric coating, were provided by CVI Laser, Inc.³⁹

Both samples had a thin (200 nm) layer of gold deposited on their surfaces. The purpose of this gold layer was threefold. First, this matched the optical reflectivities of the two samples so that all other aspects of the measurements would be the same. Second, the gold boosted the absorption for these initial measurements to enhance the photothermal response signal. Third, we wanted to ensure that all of the absorption occurred in the gold layer at the surfaces of the samples, as opposed to somewhere in the bulk or deep within the coating. Using the tabulated values of the thermal expansion coefficient, density, and specific heat for bulk gold,⁴⁰ and the reported thermal conductivity for a 200 nm gold film,¹¹ we estimate that because the thermal conductivity of the gold layer is so good, and its thickness so small, its photothermal response will be negligible below 250 MHz. At those frequencies, the observed response will be dominated by the substrate and dielectric coating.

Agreement between theory and experimental data is excellent at all frequencies, giving us high confidence in the measurement techniques. Moreover, the values for $\alpha(1+\sigma)$ and κ are consistent with our expectations from tabulated bulk values. (See Table I.)

Figure 3 shows the photothermal response of both samples, where the upper set of data points are from the sample with the dielectric coating. The thermal properties used in this fit are given in Table I. The two parameters we varied for the fit were the thermal conductivity κ , which determined the rolloff frequency, and the product $\alpha(1+\sigma)$, which determined the overall amplitude. The bulk value for the product ρC was assumed for both coating and substrate, and the absorbed power was measured from the visibility of the cavity. We measure the sum of the transmitted and reflected power and subtract it from the incident power to find the total power lost in the cavity. We then assume that this

TABLE I. Relevant material properties used in this work. Entries with an asterisk denote values derived from our data.

Material	ρ (kg/m ³)	C (J/kg K)	α (K ⁻¹)	κ (W/mK)
SiO_2	2.2×10^3 (Ref. 2)	670 (Ref. 2)	5.5×10^{-7} (Ref. 2)	1.4 (Ref. 2)
TiO_2	4.23×10^3 (Ref. 40)	688 (Ref. 40)	5×10^{-5} (Ref. 2)	10.4 (Ref. 11)
Gold film	19.3×10^3	126	$\alpha(1+\sigma)$ (K ⁻¹)	25 (Ref. 11)
Sapphire	4.0×10^3 (Ref. 2)	790 (Ref. 2)	$(5.53 \pm 0.06) \times 10^{-6*}$	$64 \pm 2*$
Coating	3×10^3	680	$(8.6 \pm 0.6) \times 10^{-6*}$	$1.08 \pm 0.15*$

loss is due to absorption, rather than scattering. This assumption is only justified because of the relatively high-absorption gold film present in our sample. The response of the coated sample was essentially identical to that of the uncoated sample at low frequencies, which agrees well with our expectations that the dominant photothermal response in that regime is due to the substrate. This agreement also gives us confidence that the absorption is the same for the two samples, which was one of the goals in applying the thin gold coatings.

At high frequencies, the response of the coated sample differs substantially from that of the uncoated one, and it agrees well with our expectations based on the thermal penetration depth as outlined in Sec. III. Using the tabulated values of ρ and C for bulk SiO_2 and TiO_2 (Ref. 40), we extract an effective thermal expansion coefficient and thermal conductivity of $\alpha_c(1+\sigma_c) = (8.6 \pm 0.6) \times 10^{-6} \text{ K}^{-1}$ and $\kappa_c = (1.08 \pm 0.15) \text{ W/mK}$. This value of the thermal conductivity is less than what would be expected from the bulk values of κ for SiO_2 and TiO_2 , which are 1.18 W/mK and 10.4 W/mK, respectively, which together would give an effective thermal conductivity of 1.83 W/mK. This reduction of the thermal conductivity is consistent with other observa-

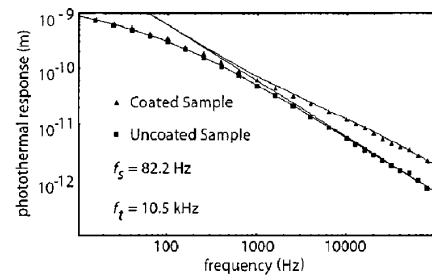


FIG. 3. Photothermal response of both samples. Upper dots are experimental data for sample 2, with the dielectric coating. The lowest theory curve is that of Ref. 10, which accounts for the substrate's photothermal response at all frequencies. The other two curves show high-frequency asymptotic behavior for samples with [Eq. (7)] and without [Eq. (4)] dielectric coatings. Noise in the data at high frequencies (low amplitudes) is due to optical crosstalk between the pump and probe beams. These effects are systematic and appear at the same levels and with the same frequency dependence in both samples. Gaussian error bars are smaller than the points as illustrated.

tions, which indicate that the effective thermal conductivity of a material in thin-film form is often lower than its bulk value.^{11–15}

V. CONCLUSIONS

We have developed a method of interferometric photo-thermal displacement spectroscopy that is well suited for studying thin dielectric films of the type used in optical coatings. Our method uses a Fabry-Perot cavity to enhance both the sensitivity of the interferometric measurement and the amplitude of the photothermal response (by enhancing the pump-beam power). Together, these can potentially provide orders of magnitude more sensitivity than conventional photo-thermal displacement methods. In this paper we demonstrate both the technique and the data analysis by measuring the thermal conductivity and thermal expansion coefficient of a high-reflectivity SiO₂-TiO₂ film on a sapphire substrate.

ACKNOWLEDGMENTS

Many thanks to Alan Weinstein for carefully reading this manuscript and for providing many helpful suggestions. This work was supported by the NSF under Grant No. PHY98-01158.

- ¹M. M. Fejer, S. Rowan, G. Cagnoli, D. R. M. Crooks, A. Gretarsson, G. M. Harry, J. Hough, S. D. Penn, P. H. Sneddon, and S. P. Vyatchanin, *Phys. Rev. D* (to be published).
- ²V. B. Braginsky and S. P. Vyatchanin, *Phys. Lett. A* **312**, 244 (2003).
- ³V. B. Braginsky, M. L. Gorodetsky, and S. P. Vyatchanin, *Phys. Lett. A* **271**, 303 (2000).
- ⁴N. Nakagawa, A. M. Gretarsson, and E. K. Gustafson, *Phys. Rev. D* **65**, 102001 (2002).
- ⁵K. Yamamoto, M. Ando, and K. Kawabe, *Phys. Lett. A* **305**, 18 (2002).
- ⁶K. Yamamoto, S. Otsuka, and M. Ando, *Class. Quantum Grav.* **19**, 1689 (2002).
- ⁷G. M. Harry, A. M. Gretarsson, P. R. Saulson, S. E. Kittelberger, S. D. Penn, W. J. Startin, S. Rowan, M. M. Fejer, D. R. M. Crooks, G. Cagnoli, J. Hough, and N. Nakagawa, *Class. Quantum Grav.* **19**, 897 (2002).
- ⁸D. R. M. Crooks, P. Sneddon, G. Cagnoli, J. Hough, S. Rowan, M. M. Fejer, E. Gustafson, R. Route, N. Nakagawa, D. Coyne, G. M. Harry, and A. M. Gretarsson, *Class. Quantum Grav.* **19**, 883 (2002).
- ⁹V. B. Braginsky, M. L. Gorodetsky, and S. P. Vyatchanin, *Phys. Lett. A* **264**, 1 (1999).
- ¹⁰M. Cerdonio, L. Conti, A. Heidmann, and M. Pinard, *Phys. Rev. D* **63**, 082003 (2001).
- ¹¹Z. L. Wu, P. K. Kuo, Lanhua Wei, S. L. Gu, and R. L. Thomas, *Thin Solid Films* **236**, 191 (1993).
- ¹²M. L. Grilli, D. Ristau, M. Dieckmann, and U. Willamowski, *Appl. Phys. A: Mater. Sci. Process.* **A71**, 71 (2000).
- ¹³Z. L. Wu, M. Thomsen, and P. K. Kuo, *Opt. Eng.* **36**, 251 (1997).
- ¹⁴B. S. W. Kuo, J. C. M. Li, and A. W. Schmid, *Appl. Phys. A: Solids Surf.* **A55**, 289 (1992).
- ¹⁵G. Langer, J. Hartmann, and M. Reichling, *Rev. Sci. Instrum.* **68**, 1510 (1997).
- ¹⁶V. B. Braginsky and A. A. Samiolenko (unpublished).
- ¹⁷M. N. Inci, *Simultaneous Measurements of Thermal Optical and Linear Thermal Expansion Coefficients of Ta₂O₅ Films: In ICO 19* (Firenze, Italy, 2002).
- ¹⁸C. L. Tien, *J. Mod. Opt.* **47**, 1681 (2000).
- ¹⁹M. A. Olmstead, N. M. Amer, S. Kohn, D. Fournier, and A. C. Boccarda, *Appl. Phys. A: Solids Surf.* **A32**, 141 (1983).
- ²⁰*Progress in Photothermal and Photoacoustic Science and Technology*, edited by A. Mandelis (Elsevier, New York, 1992), Vol. 1.
- ²¹*Progress in Photothermal and Photoacoustic Science and Technology*, edited by A. Mandelis (Prentice-Hall, Englewood Cliffs, NJ, 1994), Vol. 2.
- ²²*Progress in Photothermal and Photoacoustic Science and Technology*, edited by A. Mandelis and P. Hess (SPIE Opt. Eng. Press, Bellingham, Wash., 1997), Vol. 3.
- ²³*Progress in Photothermal and Photoacoustic Science and Technology*, edited by A. Mandelis and P. Hess (Bellingham, Wash., New York, 2000), Vol. 4.
- ²⁴Andreas Mandelis, *Phys. Today* **53**(8), 29 (2000).
- ²⁵M. DeRosa, L. Conti, M. Cerdonio, M. Pinard, and F. Marin, *Phys. Rev. Lett.* **89**, 237402 (2002).
- ²⁶E. D. Black, *LIGO Technical Document*, T000001-00-R:1-10, 2000.
- ²⁷Shanti R. Rao, PhD thesis, California Institute of Technology, 2003.
- ²⁸R. W. P. Drever, J. L. Hall, F. V. Kowalski, J. Hough, G. M. Ford, A. J. Munley, and H. Ward, *Appl. Phys. B: Photophys. Laser Chem.* **31**, 97 (1983).
- ²⁹E. D. Black, *Am. J. Phys.* **69**, 79 (2001).
- ³⁰P. R. Saulson, *Phys. Rev. D* **42**, 2437 (1990).
- ³¹Lightwave Electronics. 2400 Charleston Road, Mountain View CA 94043. <http://www.lightwaveelectronics.com>
- ³²A. Abramovici and R. Savage, NPRO-PSL Conceptual Design. *LIGO Technical Document*, pp. T960089-00-D, 1996.
- ³³D. L. Balageas, J. C. Krapez, and P. Cielo, *J. Appl. Phys.* **59**, 348 (1986).
- ³⁴B. Li, Zhaoxin Z. Zhen, and S. He, *J. Phys. D* **24**, 2196 (1991).
- ³⁵M. Liu, M. B. Suddendorf, and M. G. Somekh, *J. Appl. Phys.* **76**, 207 (1994).
- ³⁶M. Liu, M. B. Suddendorf, and M. G. Somekh, *Semicond. Sci. Technol.* **8**, 1639 (1993).
- ³⁷M. Vicanek, A. Rosch, F. Piron, and G. Simon, *Appl. Phys. A* **59**, 407 (1994).
- ³⁸J. D. Jackson, *Classical Electrodynamics*, 3rd ed. (Wiley, New York, 1975), pp. 296–298.
- ³⁹CVI Laser, LLC, 200 Dorado Place SE, Albuquerque, NM 87123.
- ⁴⁰*CRC Handbook of Chemistry and Physics*, edited by D. R. Lide, 77th ed. (CRC Press, Boca Raton, 1996–1997).

Bibliography

- [1] A. Savchenkov, I. Grudinin, A. Matsko, D. Strekalov, M. Mohageg, V. Ilchenko, and L. Maleki. Morphology dependent photonic circuit elements. *Opt. Lett.*, 31:1313, 2006.
- [2] I.S. Grudinin, A.B. Matsko, A.A. Savchenkov, D. Strekalov, V.S. Ilchenko, and L. Maleki. Ultra high Q crystalline microcavities. *Opt. Commun.*, 265:33–38, 2006.
- [3] I.S. Grudinin, V.S. Ilchenko, and L. Maleki. Ultrahigh optical Q factors of crystalline resonators in the linear regime. *Phys. Rev. Lett. A*, 74(063806), 2006.
- [4] I.S. Grudinin, A.B. Matsko, and L. Maleki. On the fundamental limits of Q factor of crystalline dielectric resonators. *Opt. Exp.*, 15:3390–3395, 2007.
- [5] I.S. Grudinin and L. Maleki. Ultralow threshold Raman lasing with CaF₂ resonators. *Opt. Lett.*, 32:166–168, 2007.
- [6] I.S. Grudinin and L. Maleki. Efficient Raman laser based on a CaF₂ resonator. *J. Opt. Soc. Am. B*, 25:594–598, 2008.
- [7] I.S. Grudinin, A.B. Matsko, and L. Maleki. Stimulated Brillouin scattering in whispering gallery mode resonators. *Phys. Rev. Lett.*, 2008 (submitted).
- [8] A.A. Savchenkov, A.B. Matsko, I.S. Grudinin, E.A. Savchenkova, and L. Maleki. Optical vortices with large space charge: generation and interference. *Opt. Express*, 14:2888–2897, 2006.
- [9] I.S. Grudinin et al. Fabrication of submillimeter axisymmetric optical components. NASA tech briefs, NASA Jet Propulsion Laboratory, March 2007.
- [10] A.A. Savchenkov et al. Simplified generation of high-angular-momentum light beams. NASA tech briefs, NASA Jet Propulsion Laboratory, March 2007.
- [11] Breck Hitz. Ultralow threshold reported for Raman laser. *Photonics Spectra*, pages 92–93, March 2007.

- [12] E.D. Black, I.S. Grudinin, S.R. Rao, and K.G. Libbrecht. Enhanced photothermal displacement spectroscopy for thin-film characterization using a Fabry-Perot resonator. *J. of Appl. Phys.*, 95:7655–7659, 2004.
- [13] Lord Rayleigh. The problem of the whispering gallery. *Philosophical magazine*, 20:1001–1004, 1910.
- [14] R.D. Richtmyer. Dielectric resonators. *J. of Appl. Phys.*, 10:391–398, 1939.
- [15] J.A. Stratton. *Electromagnetic Theory*. McGraw-Hill Book Company, New York, 1941.
- [16] A. Ashkin and J.M. Dziedzic. Observation of light-scattering from nonspherical particles using optical levitation. *Phys. Rev. Lett.*, 38:1351, 1980.
- [17] R.E. Benner, P.W. Barber, J.F. Owen, and R.K. Chang. Observation of structure resonances in the fluorescence-spectra from microspheres. *Phys. Rev Lett.*, 44:475, 1980.
- [18] C.G.B. Garrett, W. Kaiser, and W.L. Bond. Stimulated emission into optical whispering modes of spheres. *Phys. Rev.*, 124:1807–1809, 1961.
- [19] V.B. Braginsky, M.L. Gorodetsky, and V.S. Ilchenko. Quality factor and nonlinear properties of optical whispering-gallery modes. *Phys. Lett. A*, 137:393–397, 1989.
- [20] D.K. Armani, T.J. Kippenberg, S.M. Spillane, and K.J. Vahala. Ultra-high-Q toroid microcavity on a chip. *Nature*, 421:925–928, 2003.
- [21] M. Borselli, K. Srinivasan, P.E. Barclay, and O. Painter. Rayleigh scattering, mode coupling, and optical loss in silicon microdisks. *Appl. Phys. Lett.*, 85:3693–3695, 2004.
- [22] M. Borselli, T.J. Johnson, and O. Painter. Beyond the Rayleigh scattering limit in high-Q silicon microdisks: theory and experiment. *Opt. Exp.*, 13:1515–1530, 2005.
- [23] S.M. Spillane, T.J. Kippenberg, and K.J. Vahala. Ultralow-threshold Raman laser using a spherical dielectric microcavity. *Nature*, 415:621–623, 2002.
- [24] M.L. Gorodetsky and I.S. Grudinin. Fundamental thermal fluctuations in microspheres. *J. Opt. Soc. Am. B*, 21:697, 2004.
- [25] V.S. Ilchenko, X.S. Yao, and L. Maleki. Pigtailling the high-Q microsphere cavity: a simple fiber coupler for optical whispering-gallery modes. *Opt. Lett.*, 24:723–725, 1999.
- [26] M. Cai, O. Painter, and K.J. Vahala. Observation of critical coupling in a fiber taper to a silica-microsphere whispering-gallery mode system. *Phys. Rev. Lett.*, 85:74–77, 2000.

- [27] S. Uetake, R.S.D. Sihombing, and K. Hakuta. Stimulated Raman scattering of a high-Q liquid-hydrogen droplet in the ultraviolet region. *Opt. Lett.*, 27:421–423, 2002.
- [28] V.B. Braginskii, V.S. Ilchenko, and K.S. Bagdasarov. Experimental-observation of fundamental microwave-absorption in high-quality dielectric crystals. *Phys. Lett. A*, 120:300–305, 1987.
- [29] V.S. Ilchenko, A.A. Savchenkov, A.B. Matsko, and L. Maleki. Sub-microwatt photonic microwave receiver. *IEEE Phot. Techn. Lett.*, 14:1602–1604, 2002.
- [30] A.A. Savchenkov, V.S. Ilchenko, A.B. Matsko, and L. Maleki. Kiloherz optical resonances in dielectric crystal cavities. *Phys. Rev. A*, 70:Art. No. 051804, 2004.
- [31] V.S. Ilchenko, A.A. Savchenkov, A.B. Matsko, and L. Maleki. Nonlinear optics and crystalline whispering gallery mode cavities. *Phys. Rev. Lett.*, 92:Art. No. 043903, 2004.
- [32] D.W. Vernooy, V.S. Ilchenko, H. Mabuchi, E.W. Streed, and H.J. Kimble. High-Q measurements of fused-silica microspheres in the near infrared. *Opt. Lett.*, 23:247, 1998.
- [33] A. B. Matsko and V. S. Ilchenko. Optical resonators with whispering gallery modes I: Basics. *J. Sel. Top. Quant. Electron.*, 12:3–14, 2006.
- [34] V.S. Ilchenko and M.L. Gorodetskii. Thermal nonlinear effects in optical whispering gallery microresonators. *Laser Physics*, 2:1004, 1992.
- [35] M.L. Gorodetskii and A.E. Fomin. Eigenfrequencies and Q factor in the geometrical theory of whispering-gallery modes. *Quantum. Electron.*, 37:167–172, 2007.
- [36] S.D. Jacobs et al. Magnetorheological fluid composition. United States patent 5804095, September 1998.
- [37] H. Johansen and G. Kaestner. Surface quality and laser-damage behaviour of chemomechanically polished CaF₂ single crystals characterized by scanning electron microscopy. *J. of Mater. Sci.*, 33:3839–3848, 1998.
- [38] T. Kuriyagawa, M. Saeki, and K. Syoji. Electrorheological fluid-assisted ultra-precision polishing for small three-dimensional parts. *Precision Engineering*, 26:370–380, 2002.
- [39] W.B. Kim, S.J. Lee, Y.J. Kim, and E.S. Lee. The electromechanical principle of electrorheological fluid-assisted polishing. *Int. J. of Mach. Tools and Manuf.*, 43:81–88, 2002.
- [40] J. Yan, K. Syoji, and J. Tamaki. Crystallographic effects in micro/nanomachining of single-crystal calcium fluoride. *J. Vac. Sci. Technol. B*, 22:46–51, 2003.

- [41] J. Yan, K. Syoji, and J. Tamaki. Some observations on the wear of diamond tools in ultra-precision cutting of single-crystal silicon. *Wear*, 255:1380–1387, 2003.
- [42] J.E. DeGroot, H.J. Romanofsky, I.A. Kozhinova, J.M. Shoen, and S.D. Jacobs. Polishing PMMA and other optical polymers with magnetorheological finishing. *Optical Manufacturing and Testing*, 5180:123–134, 2003.
- [43] E. Yablonovitch. Inhibited spontaneous emission in solid-state physics and electronics. *Phys. Rev. Lett.*, 58:2059–2062, 1987.
- [44] A. Melloni, R. Costa, P. Monguzzi, and M. Martinelli. Ring-resonator filters in silicon oxynitride technology for dense wavelength-division multiplexing systems. *Opt. Lett.*, 28:1567–1569, 2003.
- [45] V.R. Almeida, C.A. Barrios, R.R. Panepucci, and M. Lipson. All-optical control of light on a silicon chip. *Nature*, 431:1081–1084, 2004.
- [46] S.J. Choi, K. Djordjev, P.D. Dapkus, W. Lin, G. Griffel, R. Menna, and J. Connolly. Microring resonators vertically coupled to buried heterostructure bus waveguides. *IEEE Phot. Techn. Lett.*, 16:828–830, 2004.
- [47] S.P. Pogossian, L. Vescan, and A. Vonsovici. The single-mode condition for semiconductor rib waveguides with large cross section. *J. of Lightwave Technol.*, 16:1851–1853, 1998.
- [48] R. G. Hunsperger. *Integrated Optics: Theory and Technology*. Springer Verlag, Berlin, 2002.
- [49] R.K. Chang and A.J. Campillo. *Optical processes in microcavities*. World Scientific, Singapore, 1996.
- [50] A.B. Matsko, A.A. Savchenkov, and L. Maleki. Vertically coupled whispering-gallery-mode resonator waveguide. *Opt. Lett.*, 30:3066–3068, 2005.
- [51] J. Yan, J. Tamaki, K. Syoji, and T. Kuriyagawa. Single-point diamond turning of CaF_2 for nanometric surface. *Int. J. Adv. Manuf. Technol.*, 24:640–646, 2004.
- [52] A.E. Fomin, M.L. Gorodetsky, I.S. Grudinin, and V.S. Ilchenko. Nonstationary nonlinear effects in optical microspheres. *J. Opt. Soc. Am. B*, 22:459–465, 2005.
- [53] M.L. Gorodetsky, A.A. Savchenkov, and V.S. Ilchenko. Ultimate Q of optical microsphere resonators. *Opt. Lett.*, 21:453–455, 1996.
- [54] M.L. Gorodetsky, A.D. Pryamikov, and V.S. Ilchenko. Rayleigh scattering in high-Q microspheres. *J. Opt. Soc. Am. B*, 17:1051, 2000.

- [55] W.v. Klitzing, R. Long, V.S. Ilchenko, J. Hare, and V. Lefevre-Seguin. Frequency tuning of the whispering-gallery modes of silica microspheres for cavity quantum electrodynamics and spectroscopy. *Opt. Lett.*, 26:166–168, 2001.
- [56] W. Kaiser, C.G.B. Garrett, and D.L. Wood. Fluorescence and optical maser effects in $\text{CaF}_2 - \text{Sm}^{++}$. *Phys. Rev.*, 123:766–776, 1961.
- [57] W.E. Moerner. Examining nanoenvironments in solids on the scale of a single, isolated impurity molecule. *Science*, 265:46–53, 1994.
- [58] R.J. Thompson, G. Rempe, and H.J. Kimble. Observation of normal-mode splitting for an atom in an optical cavity. *Phys. Rev. Lett.*, 68:1132–1135, 1992.
- [59] M.E. Crenshaw and C.M. Bowden. Quantum optics of two-level atoms in a dielectric: comparison of macroscopic and microscopic quantizations of the dielectric. *Opt. Commun.*, 203:115–124, 2002.
- [60] T. Aoki, B. Dayan, E. Wilcut, W.P. Bowen, A.S. Parkins, T.J. Kippenberg, K.J. Vahala, and H.J. Kimble. Observation of strong coupling between one atom and a monolithic microresonator. *Nature*, 443:671–674, 2006.
- [61] A.A. Savchenkov, A.B. Matsko, D. Strekalov, M. Mohageg, V.S. Ilchenko, and L. Maleki. Low threshold optical oscillations in a whispering gallery mode CaF_2 resonator. *Phys. Rev. Lett.*, 93:243905, 2004.
- [62] M.E. Lines. Scattering losses in optic fiber materials. I. A new parametrization. *J. Appl. Phys.*, 55:4052–4057, 1984.
- [63] E.D. Palik. *Handbook of optical constants of solids*. Academic, New York, 1998.
- [64] J.D. Jackson. *Classical electrodynamics*. John Wiley and Sons, New York, 3rd edition, 1998.
- [65] M. Reichling, M. Huisinga, S. Gogoll, and C. Barth. Degradation of the $\text{CaF}_2(111)$ surface by air exposure. *Surf. Sci.*, 439:181, 1999.
- [66] M.E. Lines. Ultralow-loss glasses. *Ann. Rev. Mater. Sci.*, 16:113–135, 1986.
- [67] M. Schlesinger, T. Szczurek, M.K. Wade, and G.W.F Drake. Anomalies in the vacuum uv absorption spectrum of Yb^{3+} in CaF_2 . *Phys. Rev. B.*, 18:6388, 1978.
- [68] Ch. Goerling, U. Leinhos, and K. Mann. Surface and bulk absorption in CaF_2 at 193 and 157 nm. *Opt. Commun.*, 249:319, 2005.

- [69] A.H. Laufer, J.A. Pirog, and J.R. McNesby. Effect of temperature on the vacuum ultraviolet transmittance of lithium fluoride, calcium fluoride, barium fluoride, and sapphire. *J. Opt. Soc. Am. A*, 55:64–66, 1965.
- [70] E.G. Schneider. A note on the photographic measurement of the transmission of fluorite in the extreme ultraviolet. *Phys. Rev.*, 45:152, 1934.
- [71] S. Logunov and S. Kuchinsky. Experimental and theoretical study of bulk light scattering in CaF₂ monocrystals. *J. Appl. Phys.*, 98:053501, 2005.
- [72] B.K. Min, T.J. Kippenberg, and K.J. Vahala. Compact, fiber-compatible, cascaded raman laser. *Opt. Lett.*, 28:1507–1509, 2003.
- [73] T.J. Johnson, M. Borselli, and O. Painter. Self-induced optical modulation of the transmission through a high-Q silicon microdisk resonator. *Opt. Exp.*, 14:817, 2006.
- [74] M.J. Weber, editor. *Handbook of Laser Science and Technology*, p.259, volume 3. Chemical Rubber Co., Boca Raton, 1986.
- [75] A. Yariv. *Quantum Electronics*. Wiley, New York, 1975.
- [76] R. Adair, L.L. Chase, and S.P. Payne. Nonlinear refractive-index of optical-crystals. *Phys. Rev. B*, 39:3337, 1989.
- [77] V. Denks, A. Kotlov, V. Nagirnyi, T. Savikhina, and G.D. Jones. Impurity-related excitonic processes in CaF₂:Sr. *Phys. Status Solidi*, 191:628, 2002.
- [78] A.A. Savchenkov, A.B. Matsko, V.S. Ilchenko, and L. Maleki. Optical resonators with ten million finesse. *Opt. Exp.*, 17:6768–6773, 2007.
- [79] I. Breunig, M. Falk, B. Knabe, R. Sowade, K. Buse, P. Rabiei, and D.H. Jundt. Second harmonic generation of 2.6 W green light with thermoelectrically oxidized undoped congruent lithium niobate crystals below 100° C. *Appl. Phys. Lett.*, 91:221110/1–3, 2007.
- [80] I.L. Fabelinskii, editor. *Molecular scattering of light*. Plenum Press, New York, 1968.
- [81] D.C. Wallace, editor. *Thermodynamics of crystals*. Dover, New York, 1998.
- [82] R. Loudon. The Raman effect in crystals. *Adv. Phys.*, 50:813–864, 2001.
- [83] M. Daimon and A. Masumara. High-accuracy measurements of the refractive index and its temperature coefficient of calcium fluoride in a wide wavelength range from 138 to 2326 nm. *Appl. Opt.*, 41:5275–5281, 2002.

- [84] L.L. Boyer, J.A. Harrington, M. Hass, and H.B. Rosenstock. Multiphonon absorption in ionic crystals. *Phys. Rev. B*, 11:1665–1680, 1975.
- [85] S. Venugopalan and A.K. Ramdas. Effect of uniaxial stress on the Raman spectra of cubic crystals: CaF_2 , BaF_2 , and $\text{Bi}_{12}\text{GeO}_{20}$. *Phys. Rev. B*, 8:717–734, 1973.
- [86] R.W. Boyd, editor. *Nonlinear Optics*. Academic Press, New York, 1992.
- [87] A.B. Matsko, A.A. Savchenkov, R.J. Letargad, V.S. Ilchenko, and L. Maleki. On cavity modification of stimulated raman scattering. *J. Opt. B*, 5:272–278, 2003.
- [88] P.G. Klemens. Anharmonic decay of optical phonons. *Phys. Rev.*, 148:845–848, 1966.
- [89] A.B. Matsko, A.A. Savchenkov, and L. Maleki. Ring-down spectroscopy for studying properties of CW Raman lasers. *Opt. Commun.*, 260:662–665, 2006.
- [90] C.V. Raman and K.S. Krishnan. A new type of secondary radiation. *Nature*, 121:501–502, 1928.
- [91] G.S. Landsberg and L.I. Mandelshtam. Eine neue erscheinung bei der lichtzerstreuung in krystallen. *Naturwissenschaften*, 16:557–558, 1928.
- [92] H.M. Pask. Continuous-wave, all-solid-state, intracavity Raman laser. *Opt. Lett.*, 30:2454–2456, 2005.
- [93] E.M. Dianov and A.M. Prokhorov. Medium-power CW Raman fiber lasers. *IEEE J. Sel. Top. Quant.*, 6:1022–1028, 2000.
- [94] O. Boyraz and B. Jalali. Demonstration of a silicon Raman laser. *Opt. Exp.*, 12:5269–5273, 2004.
- [95] T.J. Kippenberg, S.M. Spillane, B. Min, and K.J. Vahala. Theoretical and experimental study of stimulated and cascaded Raman scattering in ultrahigh-Q optical microcavities. *IEEE J. Sel. Top. Quant.*, 10:1219–1228, 2004.
- [96] K.J. Vahala. Optical microcavities. *Nature*, 424:839–846, 2003.
- [97] D.N. Mirlin and I.I. Reshina. Temperature dependence of Raman-scattering linewidth in a CaF_2 single-crystal. *Fiz. Tverd. Tela*, 13:2639, 1972.
- [98] A.R. Gee, D.C. O’Shea, and H.Z. Cummins. Raman scattering and fluorescence in calcium fluoride. *Solid State Commun.*, 4:43–46, 1966.
- [99] M.L. Gorodetsky and V.S. Ilchenko. Optical microsphere resonators: optimal coupling to high-Q whispering-gallery modes. *J. Opt. Soc. Am. B*, 16:147–154, 1999.

- [100] D.R. Rowland and J.D. Love. Evanescent wave coupling of whispering gallery modes of a dielectric cylinder. *IEE Proceedings-J*, 140:177–188, 1993.
- [101] A.A. Savchenkov, A.B. Matsko, V.S. Ilchenko, N. Yu, and L. Maleki. Whispering-gallery-mode resonators as frequency references. II. Stabilization. *J. Opt. Soc. Am. B*, 24:2988–2997, 2007.
- [102] J.W. Lou, F.K. Fatemi, and M. Currie. Brillouin fibre laser enhanced by Raman amplification. *Electron. Lett.*, 40, 2004.
- [103] L.F. Stokes, M. Chodorow, and H.J. Shaw. All-fiber stimulated Brillouin ring laser with submilliwatt pump threshold. *Opt. Lett.*, 7:509–511, 1982.
- [104] T. Heupel, M. Weitz, S. Chu, and T.W. Haensch. Cavity enhanced CW stimulated Brillouin scattering in a fused silica plate. *Opt. Commun.*, 140:281–284, 1997.
- [105] A. Debut, S. Randoux, and J. Zemmouri. Linewidth narrowing in Brillouin lasers: Theoretical analysis. *Phys. Rev. A*, 62:023803, 2000.
- [106] A. Debut, S. Randoux, and J. Zemmouri. Experimental and theoretical study of linewidth narrowing in Brillouin fiber ring lasers. *J. Opt. Soc. Am. B*, 18:556–567, 2001.
- [107] J. Geng, S. Staines, Z. Wang, J. Zong, M. Blake, and S. Jiang. Highly stable low-noise Brillouin fiber laser with ultranarrow spectral linewidth. *IEEE Phot. Techn. Lett.*, 18:1813–1815, 2006.
- [108] J. Boschung, L. Thevenaz, and P.A. Robert. High-accuracy measurement of the linewidth of a Brillouin fibre ring laser. *Electron. Lett.*, 30:1488–1489, 1994.
- [109] S.P. Smith, F. Zarinetchi, and S. Ezekiel. Narrow-linewidth stimulated Brillouin fiber laser and applications. *Opt. Lett.*, 16:393–395, 1991.
- [110] Y. Shen, X. Zhang, and K. Chen. Pump-to-stokes transfer of relative intensity noise in Brillouin fiber ring lasers. *Opt. Lett.*, 32:11–13, 2007.
- [111] F. Zarinetchi, S.P. Smith, and S. Ezekiel. Stimulated Brillouin fiber-optic laser gyroscope. *Opt. Lett.*, 16:229–231, 1991.
- [112] M. Raab and T. Quast. Two-color Brillouin ring laser gyro with gyro-compassing capability. *Opt. Lett.*, 19:1492–1494, 1994.
- [113] Y. Shen, X. Zhang, and K. Chen. All-optical generation of microwave and millimeter wave using a two-frequency bragg grating-based Brillouin fiber laser. *Electron. Lett.*, 40, 2004.
- [114] S. Norcia, S. Tonda-Goldstein, D. Dolfi, J.-P. Huignard, and R. Frey. Efficient single-mode Brillouin fiber laser for low-noise optical carrier reduction of microwave signals. *Opt. Lett.*, 28:1888–1890, 2003.

- [115] M.H. Fields, J. Popp, and R.K. Chang. Nonlinear optics in microspheres. *Prog. Optics*, 41:1–95, 2000.
- [116] Z. Yang, P. Chak, A.D. Bristow, H.M. van Driel, R. Iyer, J.S. Aitchison, A.L. Smirl, and J. E. Sipe. Enhanced second-harmonic generation in AlGaAs microring resonators. *Opt. Lett.*, 32:826–828, 2007.
- [117] T. Carmon and K. J. Vahala. Visible continuous emission from a silica microphotonic device by third-harmonic generation. *Nature Physics*, 3:430–435, 2007.
- [118] P. Del Haye, A. Schliesser, O. Arcizet, T. Wilken, R. Holzwarth, and T.J. Kippenberg. Optical frequency comb generation from a monolithic microresonator. *Nature*, 450:1214–1217, 2007.
- [119] H.B. Lin, A.L. Huston, B.J. Justus, and A.J. Campillo. Some characteristics of a droplet whispering-gallery-mode laser. *Opt. Lett.*, 11:614–616, 1986.
- [120] V. Sandoghdar, F. Treussart, J. Hare, V. Lefevre-Seguin, J.M. Raimond, and S. Haroche. Very low threshold whispering-gallery-mode microsphere laser. *Phys. Rev. A*, 54:1777–1780, 1996.
- [121] H.B. Lin and A.J. Campillo. CW nonlinear optics in droplet microcavities displaying enhanced gain. *Phys. Rev. Lett.*, 73:2440–2443, 1994.
- [122] T. Carmon, H. Rokhsari, L. Yang, T.J. Kippenberg, and K. J. Vahala. Temporal behavior of radiation-pressure-induced vibrations of an optical microcavity phonon mode. *Phys. Rev. Lett.*, 94:223902, 2005.
- [123] T. Sonehara, Y. Konno, H. Kaminaga, S. Saikan, and S. Ohno. Frequency-modulated stimulated Brillouin spectroscopy in crystals. *J. Opt. Soc. Am. B*, 24:1193–1198, 2007.
- [124] P.T. Leung and K. Young. Doubly resonant stimulated Brillouin scattering in a microdroplet. *Phys. Rev. A*, 44:593607, 1991.
- [125] J.Z. Zhang and R.K. Chang. Generation and suppression of stimulated Brillouin scattering in single liquid droplets. *J. Opt. Soc. Am. B*, 6:151–153, 1989.
- [126] S.M. Chitanvis and C.D. Cantrell. Simple approach to stimulated Brillouin scattering in glass aerosols. *J. Opt. Soc. Am. B*, 6:1326–1331, 1989.
- [127] A.L. Huston, H.B. Lin, J.D. Eversole, and A.J. Campillo. Nonlinear mie scattering: electrostrictive coupling of light to droplet acoustic modes. *Opt. Lett.*, 15:1176–1178, 1990.
- [128] J.Z. Zhang, G. Chen, and R.K. Chang. Pumping of stimulated raman scattering by stimulated Brillouin scattering within a single liquid droplet: input laser linewidth effects. *J. Opt. Soc. Am. B*, 7:108–115, 1990.

- [129] S.C. Ching, P.T. Leung, and K. Young. Spontaneous Brillouin scattering in a microdroplet. *Phys. Rev. A*, 41:5026–5038, 1990.
- [130] C.D. Cantrell. Theory of nonlinear optics in dielectric spheres. II. Coupled-partial-wave theory of resonant, resonantly pumped stimulated Brillouin scattering. *J. Opt. Soc. Am. B*, 8:2158–2180, 1991.
- [131] C.D. Cantrell. Theory of nonlinear optics in dielectric spheres. III. Partial-wave-index dependence of the gain for stimulated Brillouin scattering. *J. Opt. Soc. Am. B*, 8:2181–2189, 1991.
- [132] H.M. Lai, P.T. Leung, C.K. Ng, and K. Young. Nonlinear elastic scattering of light from a microdroplet: role of electrostrictively generated acoustic vibrations. *J. Opt. Soc. Am. B*, 10:924–932, 1993.
- [133] M.M. Elcombe and A.W. Pryor. The lattice dynamics of calcium fluoride. *J. Phys. C*, 3:492–499, 1970.
- [134] C.R.A. Catlow, J.D. Comins, F.A. Germane, R.T. Harley, and W. Hayes. Brillouin scattering and theoretical studies of high-temperature disorder in fluorite crystals. *J. Phys. C*, 11:3197–3212, 1978.
- [135] Z.H. Levine, J.H. Burnett, and E.L. Shirley. Photoelastic and elastic properties of the fluorite structure materials, LiF, and Si. *Phys. Rev. B*, 68:155120, 2003.
- [136] H. Mueller. Theory of the photoelastic effect in cubic crystals. *Phys. Rev.*, 47:947–957, 1935.
- [137] Ch. Salomon, D. Hils, and J.L. Hall. Laser stabilization at the millihertz level. *J. Opt. Soc. Am. B*, 5:1576–1587, 1988.
- [138] J. Helmcke, S.A. Lee, and J.L. Hall. Dye laser spectrometer for ultrahigh spectral resolution: design and performance. *Appl. Opt.*, 21:1686–1694, 1982.
- [139] W. Nagorney, N. Yu, and H. Dehmelt. High resolution Ba^+ monoion spectroscopy with frequency stabilized color-center laser. *Opt. Commun.*, 79:176–180, 1990.
- [140] M. Bass. *Handbook of Optics*. McGraw-Hill Book Company, New York, 2001.
- [141] D. Shoemaker, A. Brillet, C.N. Man, O. Cregut, and G. Kerr. Frequency-stabilized laser-diode-pumped Nd:YAG laser. *Opt. Lett.*, 14:609–611, 1989.
- [142] J.L. Hall and T.W. Hansch. External dye-laser frequency stabilizer. *Opt. Lett.*, 9:502–504, 1984.

- [143] J. Hough, D. Hils, M.D. Rayman, L.S. Ma, L. Hollberg, and J.L. Hall. Dye-laser frequency stabilization using optical resonators. *Appl. Phys. B.*, 33:179–185, 1984.
- [144] E.D. Black. An introduction to Pound-Drever-Hall laser frequency stabilization. *Am. J. Phys.*, 69:79–87, 2000.
- [145] A. Schoof, J. Grunert, S. Ritter, and A. Hemmerich. Reducing the linewidth of a diode laser below 30 Hz by stabilization to a reference cavity with a finesse above 10^5 . *Opt. Lett.*, 26:1562–1564, 2001.
- [146] V.V. Vassiliev, V.L. Velichansky, V.S. Ilchenko, M.L. Gorodetsky, L. Hollberg, and A.V. Yarovitsky. Narrow-line-width diode laser with a high-Q microsphere resonator. *Opt. Commun.*, 158:305–312, 1998.
- [147] T. Bottger, G.J. Pryde, C.W. Thiel, and R.L. Cone. Laser frequency stabilization at 1.5 microns using ultranarrow inhomogeneous absorption profiles in $\text{Er}^{3+}:\text{LiYF}_4$. *J. of Luminescence*, 127:83–88, 2007.
- [148] L. Allen, M.J. Padgett, and M. Babiker. The orbital angular momentum of light. *Progress in Optics*, 39:291–372, 1999.
- [149] L. Allen. Introduction to the atoms and angular momentum of light special issue. *J. Opt. B*, 4:S1–S6, 2002.
- [150] E. Santamato. Photon orbital angular momentum: problems and perspectives. *Progress in Physics*, 52:1141–1153, 2004.
- [151] D. McGloin and K. Dholakia. Bessel beams: diffraction in a new light. *Contemp. Phys.*, 46:15–28, 2005.
- [152] J. Courtial, K. Dholakia, L. Allen, and M.J. Padgett. Gaussian beams with very high orbital angular momentum. *Opt. Commun.*, 144:210–213, 1997.
- [153] J.E. Curtis, B.A. Koss, and D.G. Grier. Dynamic holographic optical tweezers. *Opt. Commun.*, 207:169–175, 2002.
- [154] S. Sundbeck, I. Gruzberg, and D. G. Grier. Structure and scaling of helical modes of light. *Opt. Lett.*, 30:477–479, 2005.
- [155] A.B. Matsko, A.A. Savchenkov, D. Strekalov, and L. Maleki. Whispering gallery resonators for studying orbital angular momentum of a photon. *Phys. Rev. Lett.*, 95:143904, 2005.

- [156] E.J. Galvez, P.R. Crawford, H.I. Sztul, M.J. Pysher, P.J. Haglin, and R.E. Williams. Geometric phase associated with mode transformations of optical beams bearing orbital angular momentum. *Phys. Rev. Lett.*, 90:203901, 2003.

Vita

Ivan Sergeevich Grudin in was born in Moscow, Russia, on January 6, 1980 to Sergey I. and Tatyana L. Grudinina. He was raised in Moscow, attending School 330 in 1986–1995 and 326 in 1995–1997. He then studied at M.V. Lomonosov Moscow State University, Physics Department. Ivan graduated from the Molecular Physics and Quantum Measurements group led by V.B. Braginsky. He was advised by M.L. Gorodetsky and received a R.V. Khokhlov thesis prize for his work on optical measurement of thermorefractive noise. In 2003 he started graduate work at the California Institute of Technology, at the Thermal Noise Interferometer, LIGO Project, later transferring to the Quantum Science and Technology Group at JPL. He was advised by Ken Libbrecht and Lute Maleki. He is a member of OSA.